Title

Novel optical techniques for characterization of native and engineered cartilage and the development of an APD based fluorescence lifetime imaging system

Author

Zhou, Xiangnan

Publication Date

2022

Peer reviewed|Thesis/dissertation

Novel optical techniques for characterization of native and engineered cartilage and the development of an APD based fluorescence lifetime imaging system

By

XIANGNAN ZHOU
DISSERTATION

Submitted in partial satisfaction of the requirements for the degree of

DOCTOR OF PHILOSOPHY

in

Biomedical Engineering

in the

OFFICE OF GRADUATE STUDIES

of the

UNIVERSITY OF CALIFORNIA

DAVIS

Approved:

Laura Marcu, Chair

Brian Kolner

Kent Leach

Jinyi Qi

Vivek Srinivasan

Committee in Charge

2022

Acknowledgment

I am grateful to a great number of people who have helped and supported me during my time as a graduate student. This work would not have been possible without them.

First and foremost, I am deeply indebted to my supervisor, Dr. Laura Marcu, for accepting me to her lab and giving me the opportunity and freedom to work on a wide range of projects and exploring new ideas. Her dedication to research, devotion to innovation and continuous support are insurmountable in shaping me into the independent scientist today. My deepest gratitude extends to my dissertation committee members, Dr. Brain Kolner, Dr. Kent Leach, Dr. Jinyi Qi and Dr. Vivek Srinivasan, for their immense knowledge and invaluable advice during my PhD study. I am extremely grateful to Dr. Paul French from Imperial College London who introduced me into the world of biophotonics.

I would like to thank all the members of Marcu Lab for their help and support. Especially, I am extremely grateful to Dr. Anne Haudenschild, Dr. Ben Sherlock, Dr. Julien Bec, Dr. Cai Li, Dr. Dinglong Ma and Dr. Alba Alfonso Garcia for a cherished time spent together in the lab. I must also thank Dr. Diego Yankelevich for his assistant, support, and guidance both in and out of academic life.

My appreciation also goes out to my friends for my amazing time in California. Dinglong and Mengxi, thank you for all the fishing, camping, hiking, and skiing trips. Cai, Tianchen and Pinghui, thank you for being wonderful friends and always there for me.

Last, and most importantly, I am ever grateful to my parents whose constant love and support keep me motivated and confident. Without their tremendous understanding, supports and encouragement, it would be impossible for me to complete my PhD.

Abstract

Articular cartilage, the near-frictionless tissue allowing smooth movement of joints, has a poor intrinsic healing capacity and can degenerate to osteoarthritis due to disease, trauma, or age. Clinical osteoarthritis is a late-stage condition for which disease-modifying opportunities are limited. Therefore, early detection of osteoarthritis is critical to support a paradigm shift from palliation of late disease towards prevention. Unfortunately, early diagnosis of OA is still a challenging, unmet clinical need that must be addressed. On the other hand, cartilage tissue engineering is an emerging strategy at the threshold of clinical translation, holding immense potential to deliver effective curative therapies for osteoarthritis. However, tissue engineers currently depend predominantly on time-consuming, expensive, and destructive techniques to monitor the maturation of engineered tissue, which can be inappropriate or impractical for large-scale biomanufacturing. Therefore, there is also an immediate need to develop nondestructive tools to monitor tissue-engineered cartilage products for both research and clinical applications.

Optical techniques such as fluorescence lifetime imaging (FLIm) and optical coherence tomography (OCT) have great potential to address these unmet needs due to their capacity to probe tissue composition and structure spatially and temporally in a nondestructive and noninvasive manner. In this dissertation, the feasibility of using FLIm and OCT for early detection of osteoarthritis and nondestructive monitoring of engineered cartilage is demonstrated, a novel solid-state multispectral FLIm system with improved performance is developed, addressing the limitations of current FLIm instrumentation for clinical and tissue engineering applications. Chapter two describes the basics principle and instrumentation of FLIm and OCT as well as the rationale for their application to cartilage research. In chapter three, the fluorescence properties of native cartilage are studied and the feasibility of using FLIm for the early detection of osteoarthritis

is demonstrated. Chapter four demonstrates the potential of bimodal FLIm-OCT as a nondestructive quality control technique for monitoring the growth of tissue-engineered cartilage in a pre-clinical animal model. Chapter five reports the design, development, and characterization of a novel multispectral FLIm system with four-times faster imaging speed, five-times lower measurement variability, and automated gain control for each spectral channel utilizing state-of-art solid-state detectors, addressing the limitation in imaging speed and signal-to-noise ratio of the current FLIm instrument for clinical and tissue engineering applications.

Table of Contents

Chapter 1 Introduction

Articular cartilage (Figure 1.1a) is the near frictionless tissue at the end of long bones with high capacity to bear load. It allows smooth movement of joints and absorbs shock. Injury to articular cartilage, which are well known for their poor healing capability, often degenerate inexorably to osteoarthritis (OA) (Figure 1.1b). OA is a prevalent and disabling disease affecting a large swathe of population worldwide [1] and have a substantial contribution to health care cost [2]. In the United States alone, OA affects more than 54 million Americans [3] and cost the economy more than $304 billion per year (both medical costs and lost wages) [4]. This large economic burden is expected to continue rising with increasing obesity and age in the population.

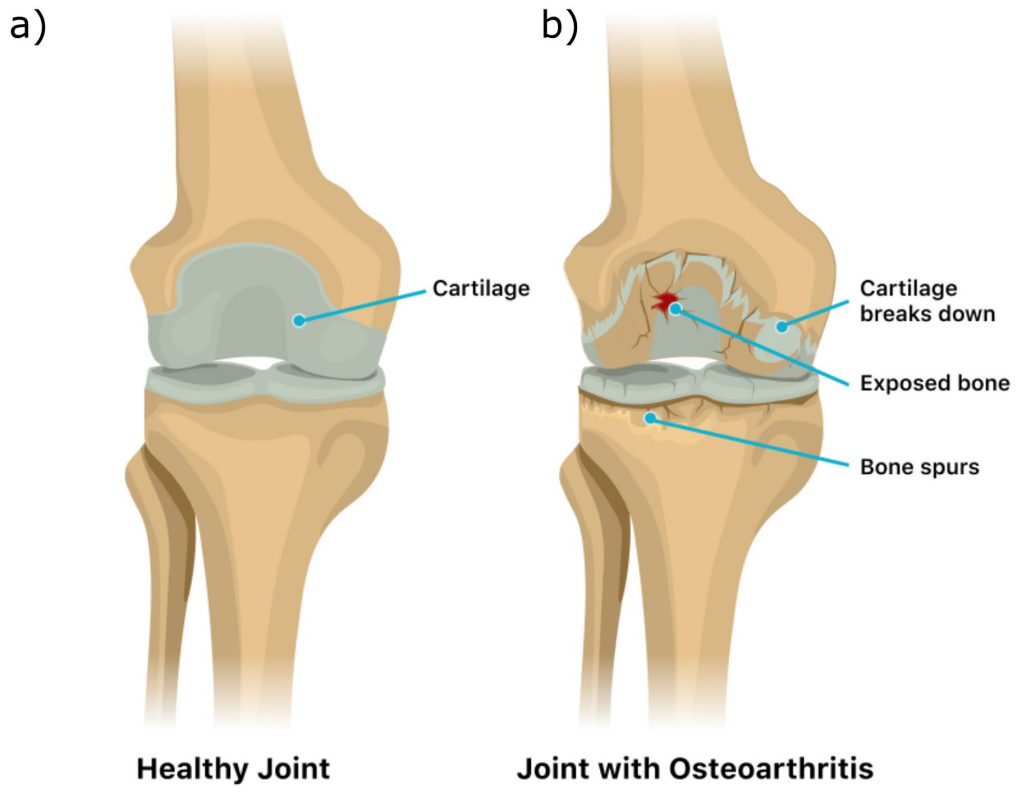

Figure 1.1 Illustration of healthy joint and joint with osteoarthritis.

Structurally, native articular cartilage possesses a unique, mechanically robust extracellular matrix (ECM), composed primarily of 15% to 30% glycosaminoglycan (GAG) (per dry weight), 50% to 75% collagen (per dry weight), and 70% to 80% water (per wet weight). The remaining balance of dry weight includes minor protein molecules and chondrocytes [5]. The large dense GAG chains embedded in a collagen matrix give rise to its exceptional mechanical functionality in the form of low friction articulation and resistance to compressive load. During the progression of osteoarthritis, the biochemical organization of the cartilage ECM is disrupted, in turn compromising the mechanical functionality of the tissue.

Unfortunately, clinical OA is a late-stage condition for which disease modifying opportunities are limited. At the early stages of OA, no visual, functional, or mechanical changes of articular cartilage appear detectable. The first observable indication of OA is gradual glycosaminoglycans (GAGs) loss. Left unattended, it will lead to a "death spiral" of increased matrix degradation and reduced biomechanical properties [6]. As a result, normal loading increases matrix damage, leading to an increasing feedback loop of cartilage damage, pain, and destruction. This deterioration continues until the cartilage completely loses its ability to bear load and is worn away to expose subchondral bone [7]. However, osteoarthritis typically develops over decades, offering a long window of time to potentially alter its course. As such, detection of biochemical alternation of cartilage ECM in pre- or early-osteoarthritis disease states will be critical to support a paradigm shift from palliation of late disease towards prevention [8].

Within the recent past, tissue engineering and regenerative medicine strategies have risen to the fore as a promising clinical treatment for OA (Figure 1.2). The primary goal of cartilage tissue engineering is to generate mechanically-functional cartilage replacement tissues that can be used to clinically repair articular cartilage defects [9-11]. For example, strategy such as scaffold-

free self-assembling process can produce neocartilage with native tissue functional properties [12], holding great potential for clinical use. However, currently, tissue engineers in both research and clinical settings depend predominantly on expensive, destructive, and time-consuming techniques as quality control to monitor the maturation of engineered cartilage. This practice can be impractical for large scale biomanufacturing and prevent spatial and temporal monitor of tissue growth which are critical for the fabrication of clinically-relevant-sized cartilage construct. Thus, there is a clear immediate need for nondestructive techniques for characterization of tissue engineered constructs at all levels of tissue engineered medical product development both in research and for clinical use. The ability to nondestructively and quantitatively measure the distribution and organization of ECM in engineered cartilage would serve as an invaluable analytical tool for the assessment of tissue engineering strategies [13].

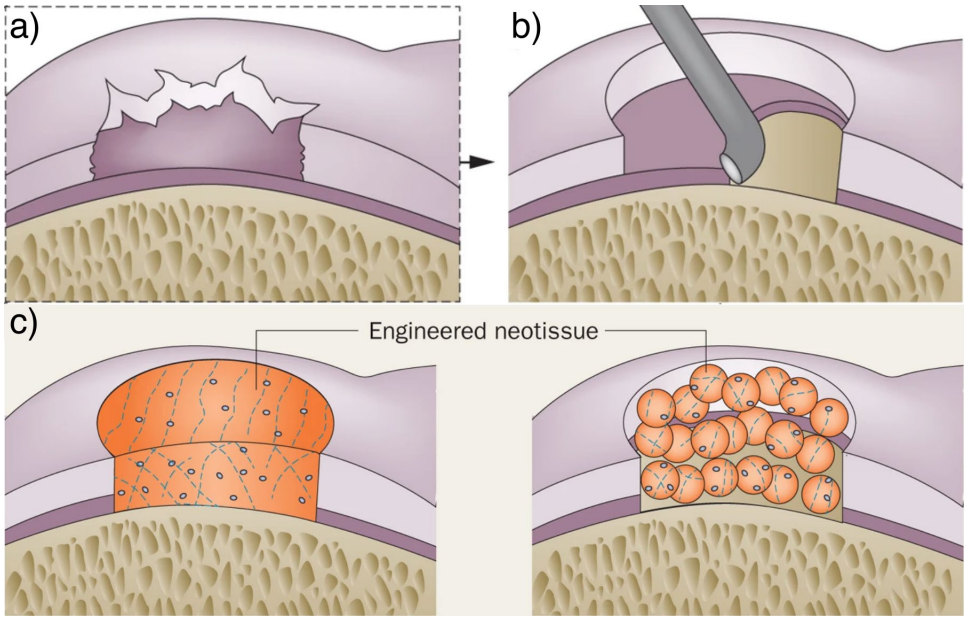

Figure 1.2 Tissue engineering approach for treating osteoarthritis. a) A full-thickness cartilage lesion. b) The lesion is debrided to ensure healthy, stable margins for integration

of the host tissue with the neotissue. c) Scaffold-free techniques based on self-assembling process or chondrospheres. Figure adapted from [14].

Conventional imaging modalities such as arthroscopic imaging, standard radiography, ultrasonography (US), and magnetic resonance imaging (MRI) are an integral part of the daily diagnosis of osteoarthritis [15-17]. However, arthroscopy is mainly a qualitative assessment technique that falls short of the laboratory assessment standards of biochemical analysis, histopathology. Both radiography and ultrasound are primarily structural imaging modalities that lack the ability to provide critical information regarding the biochemical composition of the cartilage ECM. Conventional MRI does allow accurate assessment of both cartilage morphology and biochemical composition (collagen ultrastructure and GAG concentration) but still suffers from low clinical image resolution [18].

Over the past decade, an array of novel optical imaging modalities has been explored extensively to characterize the biochemical makeup of both native and engineered cartilage. This includes laser scanning confocal microscopy [19], second harmonic generation microscopy [20], multiphoton microscopy [20-22], Fourier transform infrared imaging and spectroscopy [23-26] and Raman spectroscopy [13, 27]. Unfortunately, challenges including the complexity and high cost of instrumentation and low data acquisition speed limited these technologies mostly to benchtop use.

Fiber based label-free nondestructive imaging system combining multispectral fluorescence lifetime imaging (FLIm) and optical coherence tomography (OCT) is a promising tool to address the above needs. Fluorescence lifetime-based techniques are known to detect biochemical and functional alternations of tissue [28, 29]. Several endogenous fluorophores, including ECM structural proteins (e.g., collagen, GAG) and enzyme cofactors (e.g., NADH and

FAD), are responsible for tissue autofluorescence [30]. Optical coherence tomography, on the other hand, can provide complimentary depth-resolved high resolution structural investigation of cartilage tissue. OCT allows evaluation of cartilage microstructure and has been used arthroscopically as a translational research tool for early detection of OA [31, 32]. Recently, OCT has also been explored as a promising tool for real time monitoring of the development and growth of tissue-engineered products [33]. The fiber-based implementation makes FLIm – OCT bimodal approach a strong candidate for multimodal imaging *in vivo* as well as in challenging environment such as inside a bioreactor.

The current state of art multispectral FLIm system developed in our lab is based on the pulse sampling approach in which a large amount of fluorescence photons is generated by a short (sub-ns) and intense excitation pulse (~0.1-10 μJ) and detected by a high-bandwidth photodetector [34, 35]. To achieve multispectral detection, a time-multiplexing scheme using different length of fiber optic delay lines for each spectral band of the instrument is utilized. The fluorescence signal from tissue sample is separated into distinct spectral bands, delayed by optical fiber delay lines of different lengths, and detected by a single microchannel-plate photomultiplier tubes (MCP-PMT) detector. However, one limitation of this temporal multiplexing scheme stem from the use of a single MCP-PMT detector. The short delay between the arrival time of each channel (~50 ns) prevents adjustment of bias voltages for each individual channel. The detector gain must therefore be reduced to avoid saturation of the higher intensity channel, thus negatively impacting the signal-to-noise ratio (SNR) of the remaining channels.

In this dissertation, the feasibility of using novel optical techniques including FLIm and OCT for 1) early detection of OA and 2) non-destructive characterization of engineered cartilage construct is investigated. A novel FLIm system based on solid state avalanche photodiodes with

significant improved performance (sensitivity, imaging speed, and individual gain adjustment for each channel) was also developed, addressing the limitation of the current FLIm instrumentation.

Chapter 2 of this dissertation provides the basics of the fluorescence process as well as properties and sources of intrinsic fluorescence in native and engineered cartilage tissues. The principles of time-resolved fluorescence measurement and its common instrumentation are discussed. Emphasis is placed on multi-spectral fluorescence instrumentation based on the pulse sampling technique. Multimodal fluorescence lifetime and optical coherence tomography system are also described.

Chapter 3 of this dissertation investigates the feasibility of using fluorescence lifetime imaging for early detection of cartilage disease. Fluorescence properties of native articular cartilage and their variation across different depth-resolved zones was evaluated. The ability of fluorescence lifetime imaging to detect glycosaminoglycan (GAG) loss in native cartilage was demonstrated and the best FLIm parameters to infer the level of GAG loss was identified. Current results shows that FLIm could be utilized as a potential tool for basic research of cartilage as well as early detection of cartilage disease.

Chapter 4 of this dissertation demonstrates the potential of using bimodal fluorescence lifetime imaging and optical coherence tomography to characterize the maturation of tissue engineered cartilage in a pre-clinical implantation model. Bimodal FLIm-OCT imaging was carried out at key time points during *in vitro* then *in vivo* culturing of engineered cartilage. The heterogeneous biochemical and structural growth of engineered cartilage was detected by the bimodal imaging system demonstrating the potential of using FLIm-OCT as quality control tool for engineered cartilage manufacture.

Chapter 5 of this dissertation presents the design, development, and characterization of a novel multi-spectral fluorescence lifetime measurement device incorporating solid-state detectors and automated gain control for each spectral channel. Compared to the existing devices employing microchannel-plate photomultiplier tubes (MCP-PMT), the new system demonstrated 5-fold reduction of lifetime measurement variability in identical conditions, independent gain adjustment in each spectral band, and 4-times faster imaging speed.

In entirety, this work demonstrated the potential of fluorescence lifetime imaging and optical coherence tomography for the early detection of cartilage disease and monitoring of engineering cartilage maturation. Both of which has great impact on the patient care of osteoarthritis. A new fluorescence lifetime imaging system utilizing state of art solid state detectors was developed. Four-times faster imaging speed and five-folder reduction of lifetime measurement variability was demonstrated which will future benefit adoption of fluorescence lifetime images and its accompanied technologies as a clinical diagnosis tool and quality control method for large scale biomanufacturing of tissue engineered medical product.

Chapter 2 Introduction to fluorescence lifetime imaging

This chapter provides some background on the fluorescence process as well as properties and sources of intrinsic fluorescence in cartilage tissues. It then goes on to describe the principles of time-resolved fluorescence measurement. The principle of the frequency-domain technique, time corelated single photon counting (TCSPC) technique, time gating and pulse sampling technique are discussed. Emphasis is placed on multi-spectral fluorescence instrumentation based on pulse sampling technique and data analysis method. Multimodal fluorescence lifetime and the optical coherence tomography system are also introduced.

2.1 Fluorescence Lifetime

The theory behind fluorescence is explained in detail in *Principles of Fluorescence Spectroscopy* [36]. Briefly, fluorescence is the emission of light from an atom or molecule after a finite duration following the absorption of photons. This process is often explained by a Jablonski diagram (Figure 2.1), which details the transitions involved. Following the absorption of an excitation photon by the fluorophore of interest, several processes usually occur. The fluorophore is often excited to a higher singlet state (S_1, S_2,…, S_n) and rapidly relax to the lowest vibrational level of S_1 through internal conversion, a non-radiative process. During this process, energy of the excited electron is dissipated to other vibrational modes as kinetic energy. Internal conversion is extremely fast (10^{-14} and 10^{-11} s) and often completes prior to fluorescence emission since fluorescence is a slow process (10^{-9} to 10^{-7} s). As a result, fluorescence emission is generally observed between the lowest energy vibrational level of the first excited state (S_1) and the ground state. This ensures that the emission spectrum of a fluorophore is generally independent of the excitation wavelength. The energy of the fluorescence photon emitted is always less than that of the excitation photon due to

the energy lost through internal conversion, leading to a red-shifted emission called Stokes shift. Apart from fluorescence, electrons in the S_1 state can also decay to the ground state by means of non-radiative processes which are not shown in Figure 2.1.

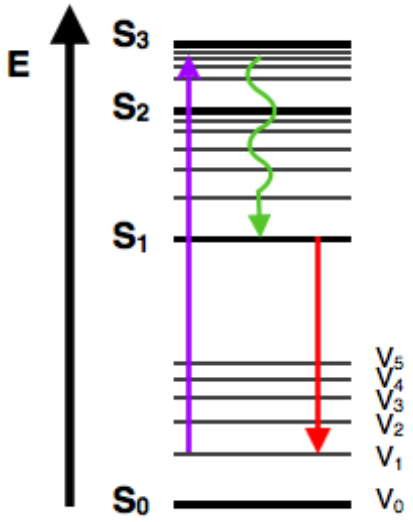

Figure 2.1 Jablonski diagram explaining the process of absorption(purple), internal conversion and vibrational relaxation (green), and fluorescence processes (red) [37].

The quantum yield and the fluorescence lifetime are the most important characteristics of any fluorophore. Quantum yield is defined as the ratio of emitted photons to the number of absorbed photons. Fluorophores with high quantum yields, such as rhodamine, display the brightest emissions. The lifetime (τ) of a fluorophore is defined as the average time between its excitation and relaxation to the ground state. The emission of fluorescence photons occurs at a typical rate of 10^8 s^{-1}, so that a typical fluorescence lifetime is near 10 ns (10×10^{-9} s). In addition, a fluorophore usually absorbs and emit photons over specific wavelength ranges, determined by its available energy levels. Thus, fluorophores are often characterized by their fluorescence lifetime, quantum yield, absorption spectrum, emission spectrum, and Stokes shift.

For a single fluorophore, the time-resolved fluorescence intensity decay profile (detected photon histogram) following instantaneous excitation can be described by a mono-exponential decay as follows:Equation Section 2

$$I(t) = I_0 e^{-t/\tau_i} + const. \tag{2.1}$$

where I_0 is the fluorescence intensity immediately following excitation and any background signal are represented by the constant term. In practice, the presence of multiple fluorophore or multiple states of a single fluorophore due to interactions with the local environment often leads to more complex fluorescence intensity decay profiles. This is generally the case for tissue autofluorescence. The complex fluorescence decays are frequently described by a multiexponential decay model summed across individual single exponential decays:

$$I(t) = \sum_i \alpha_i e^{-t/\tau_i} \tag{2.2}$$

where α is the pre-exponential factor. The fractional contribution of each decay time to the steady-state intensity can be determined as:

$$f_i = \frac{\alpha_i \tau_i}{\sum_j \alpha_j \tau_j} \tag{2.3}$$

The term $\alpha_i \tau_i$ are proportional to the area under the decay curve for each decay time. The mean lifetime ($<\tau>$) of a multiexponential mixture of fluorophores is the sum of each species lifetime (τ_i) weighted by the fractional contribution of each species (f_i):

$$<\tau>= \sum_i f_i \tau_i \tag{2.4}$$

2.2 Endogenous tissue fluorophores in cartilage

The great advantage of fluorescence is that, as an optical phenomenon, it utilizes non-ionizing radiation, is nondestructive and minimally invasive, and can hence be applied to living cells and tissues. Fluorescence from endogenous (naturally occurring) fluorophores in biological tissues can provide label-free contrast between different states of tissue for biomedical research as well as clinical applications. These endogenous fluorophores are strong biomarkers because their fluorescence properties are often dependent on the microenvironment, metabolic state, morphology, and pathological conditions of the tissue sample. Major endogenous fluorophores in cartilage tissue are structural proteins responsible for the robust mechanical properties of cartilage (collagen, GAG and aggrecan), nicotinamide adenine dinucleotide (phosphate) (NAD(P)H) and flavin adenine dinucleotide (FAD) which presents in chondrocytes. Table 2-1 summarizes excitation, emission, and lifetime characteristics of major endogenous fluorophores found in cartilage tissue. The excitation and emission spectra of major tissue fluorophores (not limited to cartilage) are illustrated in Figure 2.2.

Table 2-1 Spectral and lifetime characteristics of cartilage endogenous fluorophores

Endogenous fluorophore	Excitation (nm)	Emission (nm)	Lifetime(ns)	Reference
Metabolic coenzymes				
NAD(P)H	350 (max)	470(max)	0.4 (free), 1 to 5 (bound)	[36, 38-41]
FAD, flavin	450 (max)	550(max)	2.3 to 2.9 (free), <0.1 (bound)	[39, 42, 43]
Structural proteins				
Collagen	280 to 370	370 to 500	<5.3	[29]
GAG	300 to 370	350 to 550	~4.0	[44]
Aggrecan	300 to 370	350 to 600	2.0 to 4.0	[44]

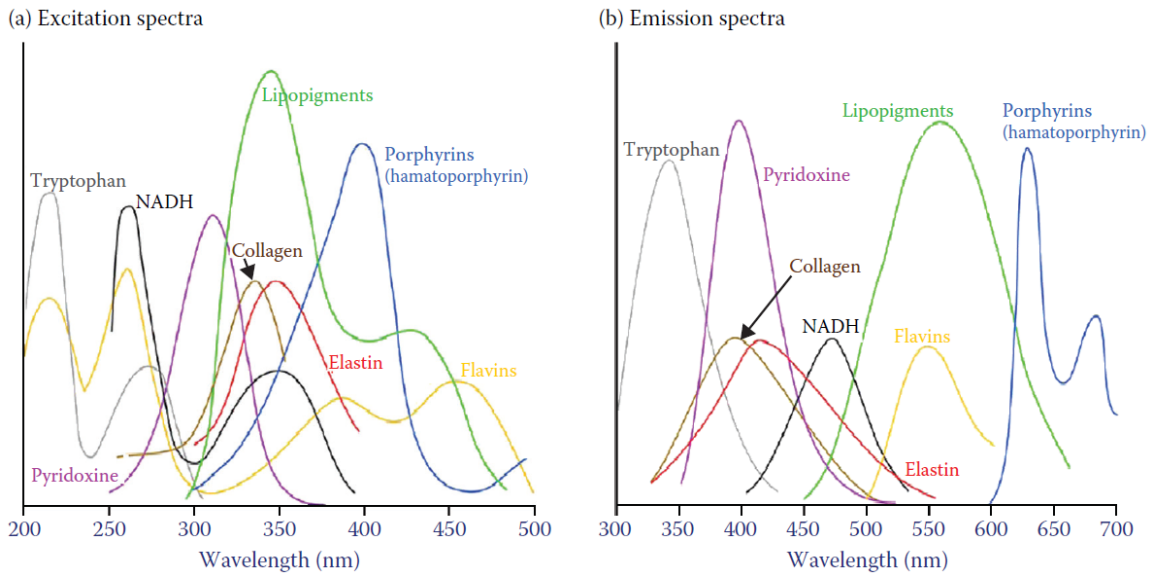

Figure 2.2 Excitation (a) and emission (b) spectra of the main types of biological fluorophores in tissue. Figure adapted from [45].

2.2.1. Native cartilage

Compared to other tissue in human body, cartilage tissue is sparsely populated by cells. Structural proteins such as collagen, aggrecan, and GAG are the major fluorophores found in cartilage ECM, which are often modified in pathological conditions [7] or during the process of engineered tissue maturation [46]. In native cartilage, structural proteins in the extracellular matrix often contribute more to the autofluorescence than the cellular component due to their higher quantum yield and abundance.

Collagen is the most abundant protein in human body with the main function of holding cells together in different organs. Collagen is composed of repeating amino acid sequences and exhibits a unique triple helix structure. Collagen type II is the predominant collagen type in cartilage tissue, accounting for more than half the dry wright of the tissue [47]. Cartilage also contains other fibrillar and globular collagen types, such as types V, VI, IX and XI [48], the roles

of which are not fully known but believed to play a role in intermolecular interactions of collagen type II. Collagens have excitation maxima at 340 nm and emission maxima at 400 nm (Figure 2.2). The autofluorescence of collagens (of which there are 28 known varieties [49]) is partly due to the present of amino acids but mainly arises from crosslinks between collagen fibers. These crosslinks can be formed by enzymatic action or other processes due to aging. An overview of collagen crosslinks that exhibit fluorescence is given in Table 2-2. Collagen has a relatively long lifetime from around 2 ns in solutions to 8.9 ns in powder [50]. Fluorescence properties of collagen can be used for noninvasive estimation of changes in ECM [51] which can be used for disease diagnosis or monitoring engineered tissue maturation.

Table 2-2 Fluorescence properties of collagen crosslinks [52]

Crosslink type	Excitation maximum (nm)	Emission maximum (nm)
Hydroxylysyl Pyridinoline	325	400
Lysyl Pyridinoline	325	400
Pentosidine	335	385
Vesperlysine	370	440
Crossline	380	460
Argpyrimidine	320	380

Proteoglycans are large macromolecules comprised of a protein core with attached *glycosaminoglycans* (*GAG*). Aggrecan is the primary proteoglycan in cartilage tissue consisting of a hyaluronana core with numerous glycosaminoglycan side chains. The accumulation of many proteoglycans into large macromolecules is critical for compressive resistance of cartilage tissue. The fluorescence properties (emission spectrum, normalized emission spectrum, average lifetime, decay constant and the fractional contribution of the slow decay component) of major native cartilage fluorophore excited at 337nm are shown in Figure 2.3.

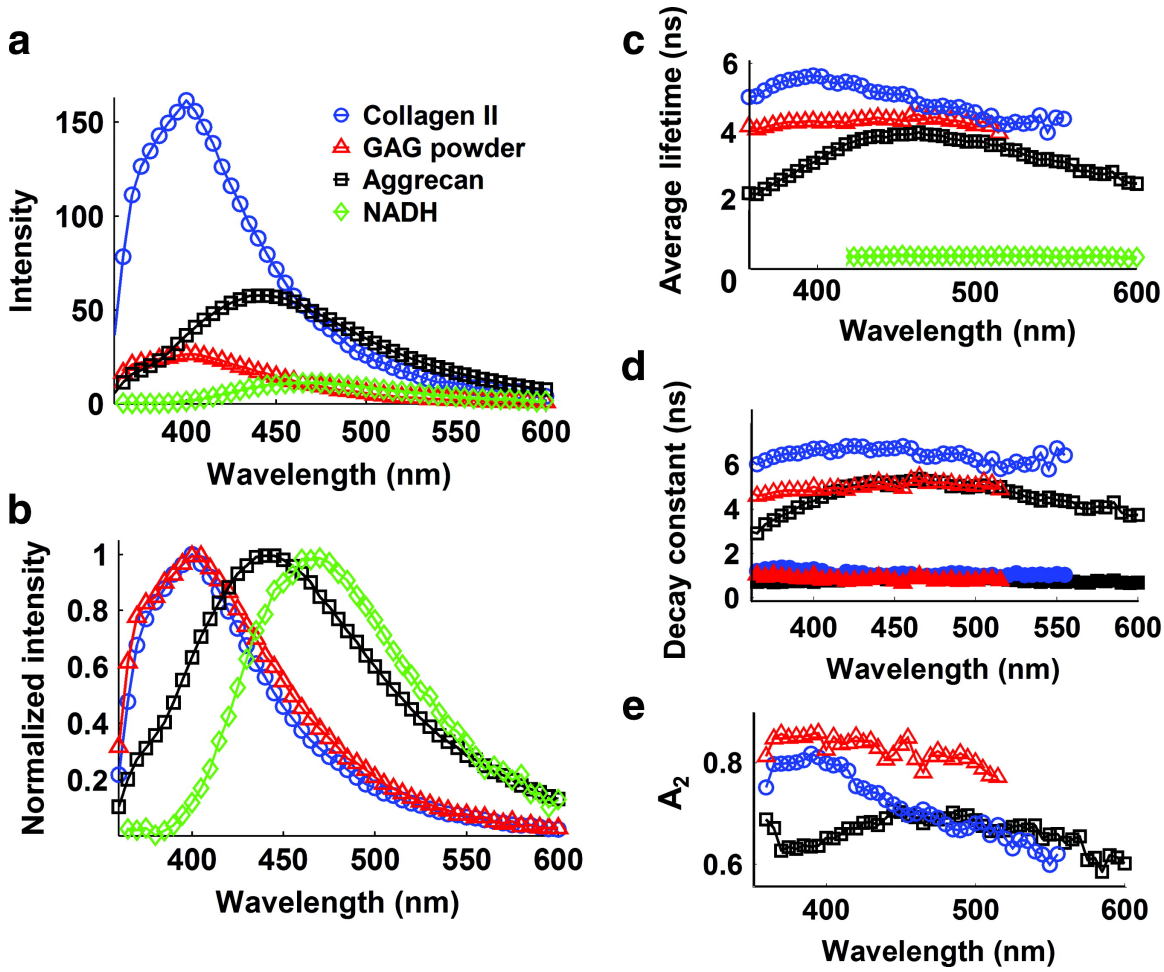

Figure 2.3 Fluorescence spectroscopic data acquired from the major endogenous fluorophores in native cartilage exited at 337 nm, including collagen type II, GAG powder, aggrecan, and NADH in chondrocytes. The time-resolved fluorescence parameters were retrieved with bi-exponential fitting. (a) Plots of fluorescence spectrum, (b) Spectra normalized to their peak values, (c) average lifetime, (d) fast decay constant τ_1 (filled symbols) and slow decay constant τ_2 (open symbols) for collagen, GAG, and aggrecan, and (e) the fractional contribution of the slow decay component A_2. GAG, glycosaminoglycans; NADH, the reduced form of nicotinamide adenine dinucleotide. Figure adapted from [44].

2.2.2. Engineered cartilage

Unlike native cartilage, which is sparsely populated by cells, engineered cartilage are comprised predominantly of chondrocytes, especially at the early stage of its development. As a result, nicotinamide adenine dinucleotide (NAD) and flavin adenine dinucleotide (FAD) contribute significantly to the fluorescence properties of engineered cartilage tissue in additional to collagen, aggrecan and GAG.

NAD and FAD are two key biomolecules consumed or generated in the metabolic process of oxidative phosphorylation [53, 54]. NAD(P)H, with excitation maximum around 340 nm and emission around 470nm, is probably the most studied endogamous fluorophore. It is involved in cell metabolism, reductive biosynthesis, antioxidation, cell signaling, aging, and regulation of apoptosis. FAD emits at a longer wavelength (550 nm) than NAD(P)H, with only small overlap, allowing for selecting imaging conditions specifically for FAD without spectral contamination from NAD(P)H. NAD(P)H is fluorescent in its reduced form and loses fluorescence under oxidation. In contrast, flavins are fluorescent in their oxidized form (FAD^+) and lose fluorescence when reduced (to $FADH_2$). The fluorescence lifetime of NAD(P)H is significantly shorter in the free state (~400 ps) compared with the protein bound state (~1 to 5 ns) of the molecule [36, 38, 39]. FAD has a longer lifetime in its free state (2.3 to 2.9 ns) compared with its protein-bound state (<0.1 ns) [42, 43, 55, 56]. Due to the pivotal role of NAD(P)H, and FAD in cell biology and metabolism, these endogenous fluorophores can play a critical role in monitoring the maturation of engineered cartilage.

2.3 Advantage of time-resolved fluorescence over intensity imaging

Time-resolved fluorescence imaging offers many unique advantages over intensity-based fluorescence imaging. Imaging based on fluorescence intensity alone provides information on the spatial distribution of fluorophores and can be used to discriminate different fluorophores with

distinct spectral properties. However, based on intensity information alone, one cannot distinguish between fluorophores with similar emission spectra or the same fluorophore within different molecular environments. Time-resolved fluorescence, on the other hand, can easily distinguish spectrally overlapping fluorophores utilizing the fluorescence lifetime information.

Overall, time-resolved fluorescence is advantageous in its ability to provide a means to contrast different fluorophores or states of fluorophores in distinct tissue microenvironments and thus can increase the specificity of fluorescence measurements. This is because fluorescence lifetime measurements are inherently radiometric (based on the assumption that the sample does not change during the period of fluorescence decay, which occurs on a nanosecond or picosecond timescale), and largely independent of fluorophore concentration, excitation and collection geometry, or attenuation of the fluorescence signal by absorption and scattering of the sample or instrumentation. This means that time-resolved measurements are robust in heterogenous samples such as biological tissue compared to intensity-based measurements. For example, proteins with different folding states, as well as bound and unbound fluorophores can be distinguished by fluorescence lifetime imaging.

In addition, time-resolved fluorescence measurements are self-referencing, meaning careful throughput calibration, which are critical for intensity-based experiment, are no longer required. Lifetime is an absolute measurement that could be repeated across different configurations (e.g., detector sensitivity excitation intensity, and path length) of the same instrument as well as a completely different instrument after accounting for the instrument response (IRF) of the specific device. As a result, multicenter studies are much easier to carry out and comparison of result from different institutes are made possible.

The key drawbacks of time-resolved fluorescence measurements include long acquisition time, high cost of instrument and sensitivity to local environment such as pH, temperature, and viscosity as well as complicated data interpretation.

2.4 Instrumentation

Fluorescence lifetime can be measured in either frequency-domain or time-domain. For frequency-domain methods, the sample is excited by light that is intensity modulated at a high frequency such that the fluorescence emission is intensity modulated at the same frequency. When this is done, a phase delay and amplitude change could be observed between the emission and excitation, determined by the intensity decay law of the sample (Figure 2.4). The decay dynamics of the sample can be recovered from the phase delay and amplitude change independently in the Fourier domain. For time-domain methods, the sample is excited by a short excitation pulse (<1 ns) and the decay is reconstructed either from a histogram of photon arrival time (Figure 2.5), by pulse sampling techniques or by time-gated detection (Figure 2.6). The details of each technique are discussed below. The decay dynamics of the sample can then be analyzed by fitting the experimental fluorescence decay profile to model decay profiles. Both frequency-domain and time-domain techniques offer unique advantages and challengers in different experimental scenarios including high throughput imaging, low photon budget imaging, high time resolution imaging or high dynamic range imaging. The advantages and limitations of different time-resolved fluorescence measurement techniques are summarized in Table 2-3.

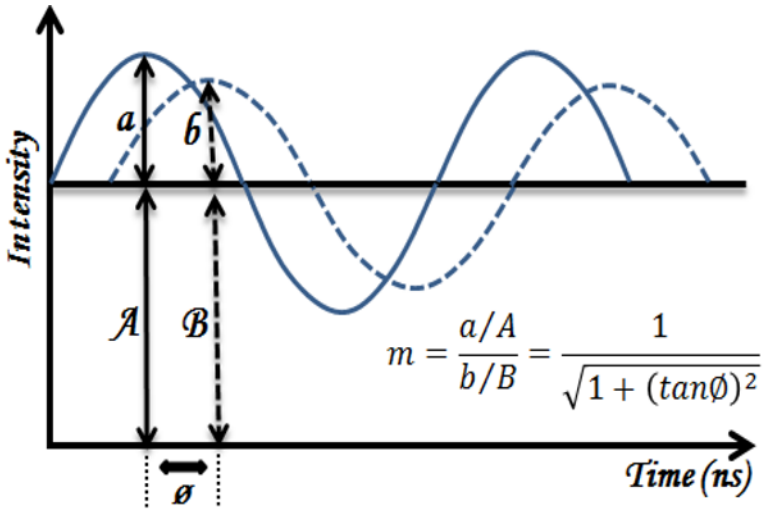

Figure 2.4 Principles of frequency domain lifetime measurements, where the fluorescence lifetime can be calculated based on the phase delay (ø) and the demodulation ratio m. Figure adapted from [57].

Table 2-3 Advantages and limitations of fluorescence lifetime techniques

Technique	Advantages	Limitations	Reference
TCSPC	• High lifetime estimation accuracy • Shot noise limited • Able to estimate multiple lifetime components	• Very high cost: > $100k • Slow acquisition speed	[58, 59]
Pulse sampling	• Fast acquisition speed • Unaffected by background light	• High cost: $50 ~ $100k • Complicated instrumentation noise characteristics	[60, 61]
Frequency domain	• Fast acquisition speed • Low cost: < $50k • Unaffected by background light	• Poor performance with low photon count	[58, 62]
Time gating	• Fast acquisition speed • Lower electronic dead time than TCSPC • Unlimited count rates	• Low sensitivity and resolution • Poor performance with low photon count • Undersampling of decay signal due to limited gates	[60, 62, 63]

2.4.1. Time Correlated Single Photon Counting

Time correlated single photon counting (TCSPC) is the most common implementation of fluorescence lifetime measurement, frequently used in microscopy. In TCSPC, the tissue sample is excited by a high repetition rate laser and the fluorescence emission is detected by single photon photodetector(s) [36] including multichannel detectors such as multi-anode photomultipliers (PMT) [64, 65] or Single Photon Avalanche Diode (SPAD) arrays [66]. The pulse energy of the excitation laser is adjusted so that less than one fluorescence photon can be detected per laser pulse to avoid photon pile-up. Generally, the detection rate is 1 photon per 100 excitation pulses. The time between the excitation pulse and the detected fluorescence photon is precisely measured and stored in a histogram (Figure 2.5). The histogram represents the waveform of the fluorescence decay when less than 1 photon is detected per excitation pulse. At higher count rate, the histogram is biased to shorter times. TCSPC is characterized by a high overall time resolution of 25 to 300 ps and a wide dynamic lifetime range. In almost all cases, the time resolution with which photons are being detected is limited by the timing jitter of the detector (25 to 300 ps) [63].

TCSPC is well suited for microscopy because the low pulse energy excitation beam can be tightly focused onto tissue sample without causing significant thermal damage. Shot noise limited detection is easily achievable, given TCSPC high temporal resolution and dynamic range. However, detection of individual photons necessitates that background light is kept to a minimum. This limits the TCSPC's potential in clinical settings, in which elimination of ambient room light is either impossible or creates a major disruption in clinical workflow. As a result, to date few clinically compatible TCSPC-based systems have been used in clinical applications. The more recent adoption of synchronous external illumination could address this shortcoming and facilitate a more effective implementation of TCSPC technique in clinics in the future [66, 67].

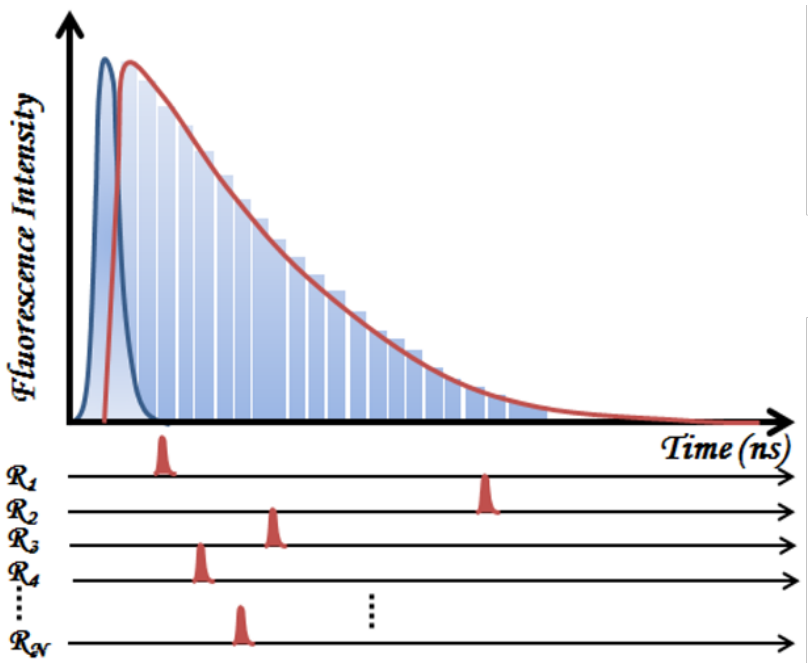

Figure 2.5 Principle of time correlated single photon counting (TCSPC). The time between the excitation pulse and the detected fluorescence photon is precisely measured and stored in a histogram. The histogram represents the waveform of the fluorescence decay when less than 1 photon is detected per excitation pulse. Figure adapted from [57].

2.4.2. Time gating

The basic idea of the time gating technique is to repetitively sample the fluorescence decay during pulsed excitation using two or more time-gates each delayed by a different time relative to the excitation pulse (Figure 2.6). The sample is excited by a short excitation pulse. The detection gate is then placed across the fluorescence decay until the entire intensity decay is measured. Two methods can be used to accomplish gated detection [68, 69]. One method is to turn on the detector for a short period of time during the intensity decay. Alternatively, same result can be achieved by gating the gain of the detector for a short period of time. The first ever time-domain lifetime instruments used gated detection to sample the intensity decay [70]. Due to low photon collection efficiency (only a small portion of the total fluorescence photons are collected per excitation pulse)

as well as the need for repeated measurement, time-gating methods has become obsolete of for most applications.

2.4.3. Pulse sampling

The pulse sampling techniques for time-resolved fluorescence measurement is perhaps the most intuitive data acquisition method among all. A schematic of the principle of the pulse sampling methods is shown in Figure 2.6. In the pulse sampling method, a large amount of fluorescence photons is generated by a short (sub-ns) and intense excitation pulse (~0.1-10 μJ) and detected by a high-bandwidth photodetector [34, 35]. The resulting electrical transient signal is captured with a fast digitizer with a resolution of tens of picosecond allowing fast recording (~few microseconds) of fluorescence decays. With pulse sampling, the entire fluorescence decay can be acquired using all emitted fluorescence photons from a single excitation pulse. Deconvolution of the instrument response function (IRF) is often required following data acquisition to recover the intrinsic fluorescence decay of the sample since the temporal responds of the photodetector and electronics are non-negligible (usually range from 100 ps to a few nanosecond).

Unlike TCSPC, which is theoretically shot noise limited, time-resolved fluorescence measurement with pulse sampling technique is affected not only by photon shot noise, but also by Johnson noise caused by detection electronics. This is the main reason TCSPC techniques are preferred for application in analytic chemistry and biology.

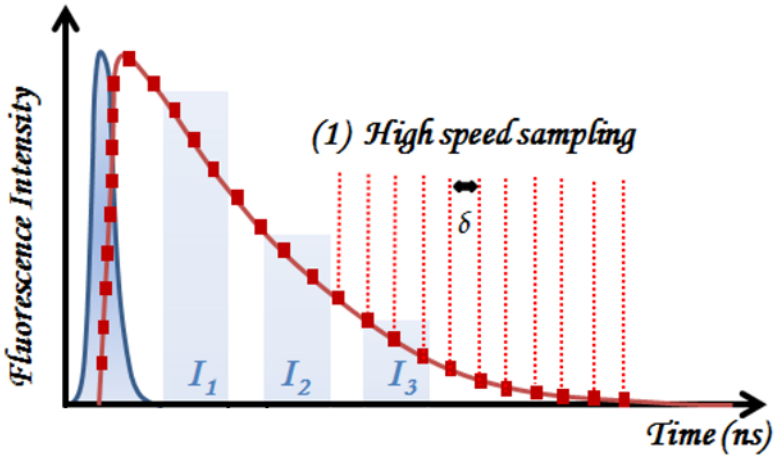

Figure 2.6 Principles of pulse sampling and time gated techniques. For pulse sampling, electrical transient signal is captured with a fast digitizer with a resolution of tens of picosecond. For time gating technique, the fluorescence decay can be collected through different time gates (I_1, I_2, I_3,…,I_n). Figure adapted from [57].

For clinical applications, several advantages of the pulse sampling technique stand out. (1) instruments based on pulse sampling techniques are generally simple and cost effective, especially for multispectral time- resolved measurement. Simultaneous acquisition of fluorescence decays in multiple spectral bands utilizing a single PMT was demonstrated with pulse sampling technique [71]. For TCSPC, simultaneous detection at multiple spectral bands can be achieved using multidetector schemes. However, multidetector schemes can be very costly when sub-nanosecond detectors are used and the requirement for multiple high voltage sources complicates the system considerably [72, 73]. (2) the large number of fluorescence photons generated within a nanosecond means that background illumination is unlikely to adversely impact the fluorescence signal. In addition, since analog detection technique is utilized, low frequency signals of ambient light can be filtered. (3) since fluorescence decay with a large number of photons can be excited at high repetition rates, the data acquisition speed of the pulse sampling technique is usually high and

limited primarily by the clinically permissible exposure to the tissue. TCSPC, on the other hand, is traditionally slow as the count rate is generally limited to 1% - 5% of the excitation rate [74], leading to data acquisition time that might be seconds long.

Overall, the time-resolved fluorescence measurement based on the pulse sampling method relies on relatively simple and cost-effective instrumentation and is capable of fast acquisition of full fluorescence decays for every excitation pulse under background illumination, making it well suited for clinical use.

2.5 Multispectral fluorescence lifetime imaging based on pulse sampling

Spectrally-resolved lifetime measurements have proven to be a reliable technique for quantitative and sensitive investigation of changes in the biochemical composition of tissue both *in vivo* and *in vitro* [29]. This is because tissue autofluorescence often originates from numerous endogenous constituents (e.g. structural proteins, metabolic enzyme co-factors, porphyrins, lipids and lipoproteins) with complex photo-physical properties and overlapping spectral emission [75]. Using spectrally-resolved and time-resolved fluorescence, multiple parameters including fluorescence intensity, spectrum and lifetime can be investigated for more complete assessment of tissue characteristics and underlying biochemical features [76, 77]. Traditionally, spectrally-resolved lifetime measurement is achieved by the wavelength scanning method in which fluorescence emission is dispersed by a monochromator and detected by either TCSPC, time gating or pulse sampling technique [78]. However, the wavelength scanning data acquisition is time consuming and can limit its applicability.

An alternative method to spectrally resolve the fluorescence is the multispectral approach. Using a combination of dichroic mirrors and optical filters, together with a time-multiplexing scheme consisting of different lengths of fiber optic delay lines, fluorescence emission can be

diverted into four distinct spectral bands and measured simultaneously by the pulse sampling technique following a single laser pulse excitation [71]. This approach enables near real-time acquisition and characterization of time-resolved fluorescence spectra using a single detector. Compared to the wavelength scanning approach, the exposure to a reduced number of optical pulses, and hence, low average optical power delivered to the tissue, can minimize the effect of phototoxicity on the tissue. The spectral bands can also be tuned to match the emission of different tissue fluorophores such as NADH, collagen, elastin, flavins and porphyrins, increasing the specificity of the approach.

Our group has reported the first implementation of a practical point-scanning system based on this approach [61]. A schematic of the system is shown in Figure 2.7. The system consists of the front-end optics (fiber-optic probe), the excitation laser (pulsed UV laser, 2-20 kHz), the wavelength selection module (WSM) using dichroic mirrors and band pass filters, the optical delay fibers, the pulse sampling photodetector (microchannel plate photomultiplier tube), and digitizer. The system itself is a single-point measurement instrument capable of multispectral fluorescence lifetime point measurements at high speed (2-20kHz). Fluorescence lifetime imaging (FLIm) is achieved by either mechanical scanning (2D or rotational) or freehand scanning. This instrument was further refined by our laboratory enabling fast system dynamic range adjustment [79], real-time data processing and real-time augmentation of fluorescence parameters for intraoperative tissue diagnosis and surgical guidance [80]. It is currently being evaluated in clinical settings to assess various tissue pathologies including oropharyngeal cancer [81] and brain tumors [82]. Also, it has been used extensively in benchtop experiments to investigate features of atherosclerotic lesions [83], to identify positive cancer margins in breast tissue specimens [84], and to answer fundamental biomedical questions in tissue engineering [85, 86]. The same time-multiplexing

single PMT approach was adopted by others groups [87-89] and combined with galvanometer scanners for both *in vitro* and *in vivo* tissue diagnosis with a handhold endoscope[90] or scanning microscopy [87, 91].

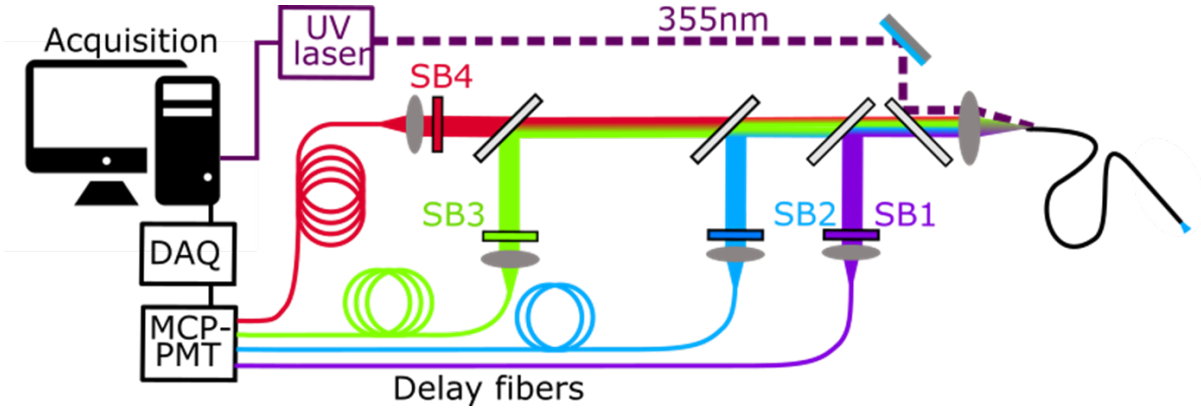

Figure 2.7 Multispectral fluorescence lifetime measurement system utilizing pulse sampling technique. Using a combination of dichroic mirrors and optical filters, together with a time-multiplexing scheme consisting of different length of fiber optic delay lines, fluorescence emission can be diverted into four distinct spectral band and measured simultaneously by pulse sampling technique following a single laser pulse excitation [71]. SB: Spectral Band, MCP-PMT: Microchannel plate photomultiplier tube, DAQ: Data Acquisition.

A limitation of the current temporal multiplexing scheme stems from the use of a single MCP-PMT detector. The short delay between the arrival time of each spectral channel (~50 ns) prevents adjustment of bias voltages for each individual channel. Therefore, the detector gain must be reduced to avoid saturation of the higher intensity channel, thus negatively impacting the signal-to-noise ratio (SNR) of the remaining channels (Figure 2.8). For biological tissue, collagen fluorescence often dominates due to the abundance and high quantum yield of collagen, limiting the ability of the current instrument to detect other weak fluorophores. This can be avoided by

selectively attenuating the spectral channel corresponding to collagen emission using natural density filters, but the approach adds to the complexity of experiment and data interpretation.

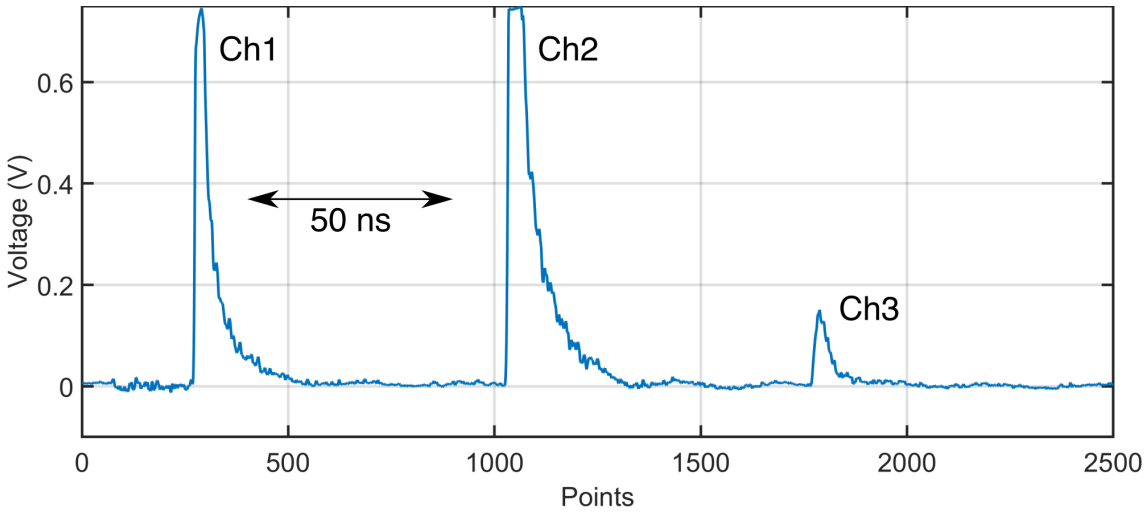

Figure 2.8 Limitation of current time-multiplexing approach. The short delay between the arrival time of each spectral channel (~50 ns) prevents adjustment of bias voltages for each individual channel. As a result, the detector gain must be reduced to avoid saturation of the higher intensity channel (Ch2), thus negatively impacting the signal-to-noise ratio (SNR) of the remaining channels. In the case shown here, the signal in channel 3 become too low to provide any useful information.

2.6 Time-resolved fluorescence data analysis

For time-resolve fluorescence measurements, the measured fluorescence transient signal ($y(t)$) is a convolution of the fluorescence impulse response function (fIRF) $h(t)$ and the instrument impulse response function (iIRF) $I(t)$. Mathematically, this can be expressed as

$$y(t) = h(t) * I(t) + \varepsilon(t) \tag{2.5}$$

with $\varepsilon(t)$ denotes any additive measurement noise. In discrete-time representation, for N equal sampling time points $t_i = i\delta t, i = 0, \ldots, N-1$ and sampling interval δt, we have

$$y(k) = \sum_{i=0}^{k} I(k-i) \cdot h(i) + \varepsilon_k \tag{2.6}$$

for $k = 0, \ldots, N-1$.

fIRF represents the intrinsic fluorescence decay of the sample and is usually modeled as a multiexponential decay function. iIRF contains information about the distortion introduced to the fluorescence transient signal by the instrument used in the experiment. This includes distortions due to the finite rise time, width and decay of the excitation laser pulse, distortion caused by the limited frequency response of the photodetector and digitizing electronics, and distortions introduced by the light dispersion of optical components in the instrument (usually optical fibers) [92]. An iIRF is often measured from a sample with a very shot or instantaneous lifetime (e.g., SHG signal from a urea crystal for two-photon microscopy).

A main challenge in the analysis of time-resolved fluorescence measurements is to remove the instrument distortion from the measured fluorescence transient signal to recover the intrinsic fIRF. This is often achieved through the deconvolution process which consist of the recovery of intrinsic fIRF from the noise-corrupted measurement using the instrument response function.

Critical to any deconvolution methods is the choice of model for which the intrinsic fIRF is parameterized. Two categories of parameterizations are generally employed to define the fIRF model: (1) *Parametric* models, which rely on *a prior* knowledge of the fluorescence sample under study, for example, the number of tissue fluorophores and the decay characteristic of each fluorophore. The most often used parametric fIRF model is the multiexponential model in which the fIRF is modeled as the summation of multiple single exponential decays. In this case, *a priori* assumptions are that the sample consists of a discrete number of fluorophores, each with a single exponential decay profile. If a continues distribution of fluorophores is assumed, a stretched-exponential model for the fIRF is adopted [93]. (2) *Nonparametric* models that do not make any a

priori assumptions of the physical behavior of the fluorescence sample. Instead, these models are often parameterized purely for mathematical convenience. For example, the fIRF can be expanded on to a set of orthogonal basis functions and parameterized by the set of expansion coefficients. The most commonly used basis functions are Fourier series [94], Laplace series [95], exponential series [96] and Laguerre series [97].

The *parametric* models are most appropriate if they describe the physics of fluorescent samples accurately. In fact, the prevalent use of the multiexponential model is due to the fact that many physical phenomena follow the single exponential decay law [98], especially for identification of known fluorophores in a controllable environment such as in cell imaging. However, for complex samples such as biological tissues, the number and type of fluorophores are often unknown, making it hard to justify and interpret parametric models from a physical point of view. On the contrary, *nonparametric* models represent fIRF without any *a priori* assumption of the number of the fluorophore and their decay profiles. By carefully choosing the expansion basis, nonparametric models are often numerically more efficient and mathematically easier to evaluate. However, without constraints from the underlying physical principles, they are highly sensitive to measurement noise and may result in unphysical decay functions in the presence of significant noise. For instance, it is well known that a Fourier series expansion may induce oscillation behavior (bumps) in fIRFs that do not match well with the smooth intensity decay function as expected [94].

2.7 Laguerre expansion models

Recently, a semi-parametric approach has been developed in our lab [99] to provide an efficient way of combining *a priori* knowledge into nonparametric models. In this case, the fIRF is expanded onto a set of Laguerre basis functions (LBFs) but controlled by additional constraints

such that the reconstructed fIRF is necessarily positive, monotonically decreasing, strictly convex and asymptotically goes to zero. Mathematically, fIRF is expressed as

$$h(k) = \sum_{l=0}^{L-1} c_l b_l(k;\alpha) \tag{2.7}$$

where c_l is the lth expansion coefficient, L is the total number of LBFs. The discrete-time LBFs are defined as:

$$b_l(k;\alpha) = \alpha^{\frac{k-l}{2}}(1-\alpha)^{\frac{1}{2}}\sum_{i=0}^{l}(-1)^i\binom{k}{i}\binom{l}{i}\alpha^{l-i}(1-\alpha)^i \tag{2.8}$$

where $l = 0, \ldots, L-1$ is the order of LBFs, and $0 < \alpha < 1$ is the scale parameter that controls the overall decay rate of the set of LFBs. The first 8 LBFs with $\alpha = 0.919, k = 500$ are visualized in Figure 2.8. The effect of the scale parameter α on the LBFs are illustrated in Figure 2.9.

The additional constrains can be expressed as

$$\lim_{t\to\infty} h(t) = 0 \tag{2.9}$$

$$\lim_{t\to\infty} h'(t) = 0 \tag{2.10}$$

$$\lim_{t\to\infty} h''(t) = 0 \tag{2.11}$$

$$h'''(t) \leq 0 \tag{2.12}$$

The Laguerre coefficients c_l in Eq. 2.7 can be estimated through a non-negative least-square problem (for details, please refer to [99]) and used for the reconstruction of intrinsic fIRF. The average fluorescence lifetime can then be computed from the fIRF. Realtime (<10 μs) and robust fluorescence lifetime estimation is achieved with this method making it better suited for clinical use.

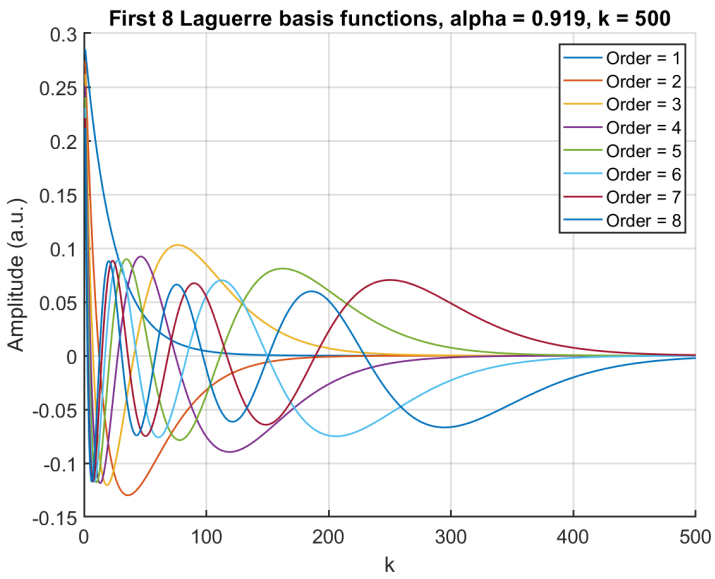

Figure 2.9 The first 8 Laguerre basis functions (LBFs) plotted for α = 0.919 and k=500.

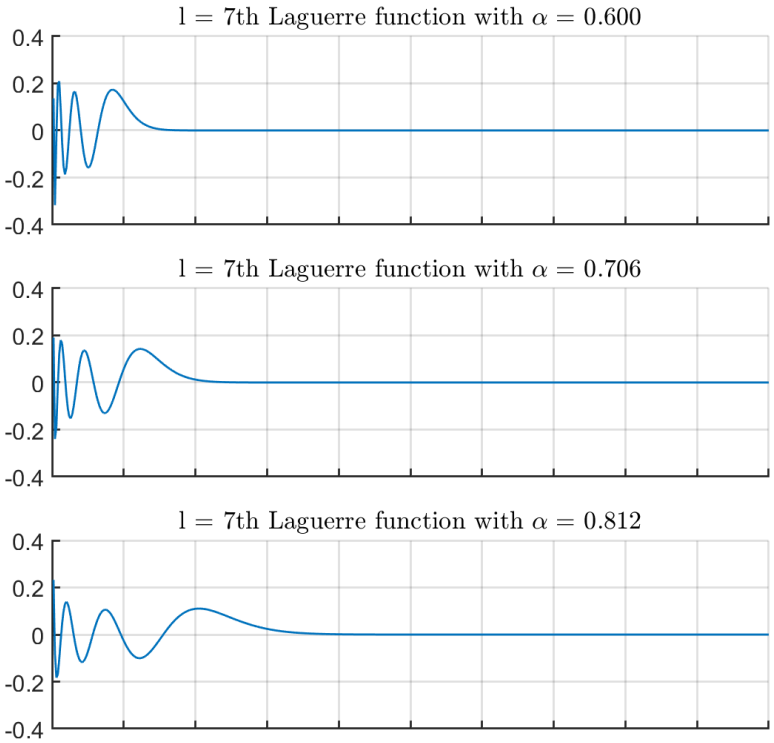

Figure 2.10 The effect of the scale parameter α on the 7th Laguerre function. The shorter the α the faster the LBFs decays to 0.

2.8 Multimodal imaging combining fluorescence lifetime imaging and optical coherence tomography

Pathological changes in tissue are often accompanied by alteration in not only biochemistry but also morphology. These alterations often include changes in tissue optical properties like fluorescence (intensity and lifetime), scattering and absorption coefficient. Thus, the most complete and reliable optical tissue assessment would be sensitive to both biochemistry and morphological changes. Unfortunately, no single optical imaging modalities currently available can provide both. Fluorescence lifetime imaging, for example, can provide biochemical and/or functional information with high sensitivity but falls short in providing tissue structure information due to its limited penetration depth (~300 μm). On the other hand, ultrasound and optical coherence tomography (OCT) can provide depth-resolved structural information of tissue but lacks any biochemical information. A promising solution, which has recently gained significant attention, is to combine multiple complementary modalities such that the product obtains the strength of the individual modalities. The resulting multimodal imaging system is capable of investigating the biochemistry as well as morphology of tissue in a single examination. The complementary data generated with multimodal systems has been shown to improve the sensitivity and specificity of tissue analysis [100-104].

The recent push to collect complementary biochemical and morphological data has led to the development of several multimodal imaging systems for both clinical use and research investigation. For instance, time-resolved fluorescence and ultrasound has been combined for

diagnosis of oral carcinoma [105], characterization of atherosclerosis [103, 104], and nondestructive evaluation of engineered cartilage [106]. Fluorescence imaging has been combined with OCT for detection of atherosclerosis [107, 108], colon cancer [109] and early bladder cancer [100]. Raman spectroscopy has been combined with OCT for characterization of breast tissue [110] and clinical skin cancer screening [111]. Raman spectroscopy, fluorescence lifetime imaging and OCT have been combined for mesoscale label-free characterization of tissue [112].

Our group has developed a fiber-based multimodal imaging system combining a commercial swept source OCT with multispectral FLIm developed in our lab for co-registered characterization of tissue such as atherosclerotic plaques [113]. Optical Coherence Tomography (OCT) is a high-resolution imaging modality utilizing low-coherence interferometry to measure the depth-resolved intensity of light backscattered from tissue samples up to a depth of 1~2 mm. OCT is similar to B-scan ultrasound except that image formation depends on differences in optical rather than acoustic backscattering properties of tissue [114]. Changes in tissue backscattered properties generally correlates with changes in tissue morphology. The resulting high-resolution cross-sectional volumetric data thus provide high-fidelity depictions of tissue structure and morphology. A schematic diagram of the multimodal system is shown in Figure 2.11.

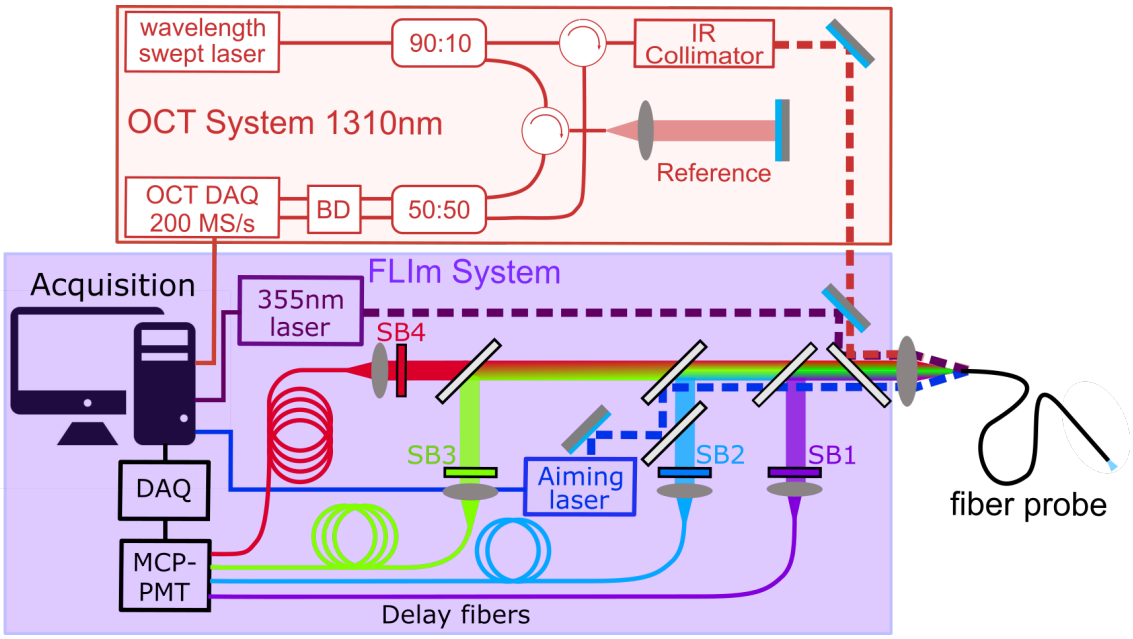

Figure 2.11 Multimodal fluorescence lifetime imaging and optical coherence tomography system. The FLIm subsystem is based on the pulse sampling approach, the detail of which has been reported [115]. Briefly, light from a 355 nm laser (4 kHz, 7.89 mW) is guided to the sample in the inner cladding of a double clad fiber. Tissue autofluorescence was collected by the same fiber to a wavelength selection module that separates the light into four spectral bands. Signals from four spectral bands (SB) are temporally multiplexed onto a single photomultiplier tube (PMT) using optical fiber delay lines and digitized by a high-speed digitizer. The OCT subsystem includes a 50mW, 1310 ± 55 nm swept-source laser with an A-scan line rate of 50 kHz. Laser output from the laser is split to the sample arm (90%) and reference arm (10%) using a 90/10 fiber coupler. The reflected signal from tissue sample and reference mirror are recombined using a 50/50 fiber coupler and detected by a dual balanced detector (BD). The output of the dual balanced detector is sampled by a 12 bit, 500 MS/s FPGA DAQ board in the OCT engine.

A comprehensive description of the FLIm-OCT system has been reported [113]. The FLIm sub-system is described in Section 2.5. For OCT, briefly, the system uses a 1310±55 nm swept

laser OCT engine from Axsun Technologies with an average output power of 50 mW and native A-scan line rate of 50 kHz. The OCT laser is fiber-coupled into a 90:10 fiber coupler sending 10% of the output power to the interferometer reference arm consisting of 2 m of single mode fiber (Corning® SMF-28 Ultra , to match the length of optical fiber probe) and a mirror mounted on a translation stage. The position of the mirror can be adjusted to match the optical path length of the sample and reference arm. The remaining 90% of OCT laser light is coupled into the core of the fiber probe consisting of a 2m section of double clad fiber (DCF) (Nufern, LMAGDF-10/400). The fiber probe has a doped silica core and a pure silica inner cladding with diameters of 11.5 μm and 400 μm, respectively. The concentric nature of the DCF give rise to the inherent co-registration of the FLIm and OCT data. The numerical apertures of the core and cladding are 0.08 and 0.46 respectively. The reflections in both the sample and reference arm are coupled back and separated from the incoming light by three-port fiber circulators. Light from the sample and reference arm is mixed using a 50:50 fiber coupler and detected by the onboard dual-balanced photodiodes in the OCT engine. The signals from the photodiodes are digitized and processed by the 12 bit, 500MS/s FPGA DAQ board inside the OCT engine. Depth-resolved B-scan are streamed to the experimental control computer. 2D imaging can be achieved by raster scanning of the fiber probe above the tissue sample using a motorized three-axis translation stage.

Chapter 3 Fluorescence lifetime imaging for early detection of osteoarthritis

Glycosaminoglycan (GAG) loss is an early marker of osteoarthritis, which is a clinical late-stage disease that affects millions of people worldwide. The goal of this chapter is to evaluate the ability of a fiber-based fluorescence lifetime imaging (FLIm) technique to detect GAG loss in articular cartilage. Native bovine cartilage explants (n=20) were exposed to 0 (Control), 0.5 (Low), or 1 U/mL (High) concentrations of chondroitinase ABC (cABC) to create samples with different levels of GAG loss. FLIm assessment (excitation: 355 nm; detection: channel 1: 375-410 nm, channel 2: 450-485 nm, channel 3: 530-565 nm) was conducted on depth-resolved cross-sections of the cartilage sample. FLIm images, validated with histology, revealed that loss of GAG resulted in a decrease of fluorescence lifetime values in channel 2 (Δ=0.44 ns, $p<0.05$) and channel 3 (Δ=0.75 ns $p<0.01$) compared to control samples (channel 2: 6.34 ns; channel 3: 5.22 ns). Fluorescence intensity ratio values were lower in channel 1 (37%, $p<0.0001$) and channel 2 (31% decrease, $p<0.0001$) and higher in channel 3 (23%, $p<0.0001$) relative to control samples. These results show that FLIm can detect the loss of GAG in articular cartilage and support further investigation into the feasibility of *in-vivo* FLIm arthroscopy.

3.1 Introduction

Articular cartilage is the near frictionless tissue at the end of long bones that allows smooth movement of joints and absorbs shock. Cartilage degenerative diseases such as osteoarthritis (OA)

are major causes of disability worldwide [117] and have a substantial contribution to healthcare cost [2]. This large economic burden will continue to increase as the population ages. Clinical osteoarthritis is a late-stage condition for which disease-modifying opportunities are limited. However, osteoarthritis typically develops over decades, offering a long window of time to potentially alter its course. As such, characterization of pre- or early-osteoarthritis disease states will be critical to support a paradigm shift from palliation of late-stage disease towards prevention [8]. Unfortunately, early diagnosis of OA is still a challenging, unmet clinical need that must be addressed.

Cartilage extracellular matrix (ECM) is composed primarily of 15-30% glycosaminoglycan (GAG) (per dry weight), 50-75% collagen (per dry weight), and 70-80% water (per wet weight). The remaining balance of dry weight includes minor protein molecules and chondrocytes [5, 118]. The mechanical properties of articular cartilage are determined by the biochemical composition of the main tissue constituents, GAG and collagen, creating a structure-function relationship in which GAG resists compressive loading and collagen resists tensile loading within the tissue [119]. During the early stages of OA, the changes in cartilage are clinically silent. No visual, functional, or mechanical alterations of articular cartilage appear detectable. Gradual GAG loss is the first observable indication of OA. Left untreated, it will lead to a “death spiral” of increasing matrix degradation and reduced biomechanical properties [6]. As a result, normal loading increases matrix damage, leading to a positive feedback loop of cartilage damage, pain, and destruction. This deterioration continues until the cartilage completely loses its ability to withstand load and is worn away to expose subchondral bone [7]. Therefore, the detection of GAG loss is critical for the early diagnosis of OA.

Imaging modalities are an integral part of the diagnosis of osteoarthritis. Conventional imaging modalities like arthroscopic imaging, standard radiography, ultrasonography (US), and magnetic resonance imaging (MRI) are widely used in daily clinical diagnosis [15-17]. Despite that, arthroscopy is primarily a qualitative assessment technique that falls short of the laboratory assessment standards of histopathology, biochemical analysis, and biomechanical testing. Both radiography and ultrasound fail to provide critical information regarding the biochemical composition of the cartilage ECM. Conventional MRI allows accurate assessment of both cartilage morphology and biochemical composition (collagen ultrastructure and GAG concentration) but still suffers from low clinical image resolution [18].

Over the past decade, novel optical imaging modalities have been studied to evaluate the biochemical makeup and structural organization of cartilage and are being actively explored for utility in cartilage research and OA diagnosis. This includes laser scanning confocal microscopy (LSCM) [19], second harmonic generation microscopy (SHG), multiphoton microscopy (MPM) [21], Fourier-transform infrared imaging and spectroscopy (FT-IRIS) [23] and Raman spectroscopy [27]. Unfortunately, challenges including the complexity and high cost of instrumentation and low data acquisition speed hamper their clinical translation. Moreover, optical coherence tomography (OCT) allowing evaluation of cartilage microstructure associated with cartilage health has been used arthroscopically as a translational research tool for early diagnosis of OA [31, 32]. Still, OCT lacks the ability to provide biochemical information.

Therefore, there is a need for new clinical-compatible imaging modalities for *in vivo* assessment of biochemical composition related to cartilage health. Fiber based time-resolved fluorescence lifetime imaging (FLIm) has the potential to address this need. FLIm with a lower-case m was used as an abbreviation to distinguish our fiber-based technology (Im ⇔ Imaging)

from fluorescence lifetime microscopy (FLIM). Over the past decade, several groups have reported that FLIm may be used for disease diagnosis and tissue characterization with applications in numerous clinical areas including oncology, cardiology, and ophthalmology [60]. Multimodal instrumentation combining FLIm and ultrasound has also been used to monitor matrix composition and mechanical properties of engineered cartilage tissue during maturation [120, 121]. Recent advantages in FLIm devices using miniature fiber optics probes, along with fast electronics enabling fast data acquisition speed, analysis, and real-time display [122] make this technique highly compatible with modern clinical arthroscopes. Hence, the goal of the present study was to investigate the feasibility of using FLIm for early detection of cartilage disease. Specifically, this study focused on 1) evaluation of fluorescence properties of native articular cartilage and their variation across different depth-resolved zones, 2) investigation of whether FLIm can detect the depletion of major cartilage biochemical constituents involved in development of osteoarthritis, namely GAG, and 3) determining whether FLIm parameters can be used to infer the level of glycosaminoglycan loss in cartilage.

3.2 Materials and Methods

3.2.1. Cartilage Harvest

Articular cartilage was excised as full thickness cylindrical osteochondral plugs (n = 25) from a juvenile (2-week-old) bovine femoral head obtained from an abattoir (Research 87, Boylston, MA) within 48 hrs of death. Cartilage explants were wrapped in gauze and soaked in PBS with protease inhibitors (2-nM phenylmethylsulfonyl fluoride, 10-mM N-ethyl malemide, 2-mM ethylene diamine tetraacetatic acid, and 5-mM benzamidine-HCl) as previously described [123], underwent three freeze thaw cycles to lyse cells, and stored at -20°C in protease inhibitor until imaging (Figure 2.1a).

3.2.2. Proteolytic Enzyme Treatments

Cartilage explants were placed one sample per well in 6 well plates (Costar, Corning, NY) in 6 mL of phosphate buffered saline (PBS) (Sigma-Aldrich, St. Louis, MO). To remove proteoglycans, chondroitinase ABC (cABC) (Sigma-Aldrich) was added to a final concentration of 0 U/mL (Control), 0.5 U/mL (Low cABC), or 1 U/mL (High cABC) of cABC per well. All treatments included 50 U/mL salt activated nuclease (ArcticZymes, Tromsø, Norway), 0.02% EDTA (Life Technologies, Grand Island, NY), and 1% penicillin/streptomycin/fungizone (Lonza, Basel, Switzerland). Treatment occurred for 10 hrs at 37°C on a rotatory plate at 35 revolutions/min. After treatment, explants were washed in fresh PBS for 12 hrs. to remove residual enzymes.

3.2.3. FLIm assessment of articular cartilage

After enzymatic treatment, full thickness cartilage samples were cut perpendicular to the surface into two half-cylinders. Samples were placed on a custom, glass sample holder for cross-sectional FLIm assessment. To study the depth dependent fluorescence lifetime (LT) of cartilage, the other half of the cylinder was sectioned using a custom cutting jig into approximately the superficial, middle, and deep zones of the cartilage and imaged *en-face* (schematic is shown in Figure 3.1a). During FLIm acquisition, samples were immersed in PBS to maintain hydration. The fluorescence LT images were reconstructed from FLIm measurements and co-registered with histology images using the shape of the tissue sections. Regions of interest (ROIs) were selected in FLIm images following co-registration based on histology features for further analysis. Following imaging, cartilage samples were placed in formalin and processed routinely for histologic analysis. MATLAB (Mathworks, Inc.) software was used for image co-registration and ROIs selection.

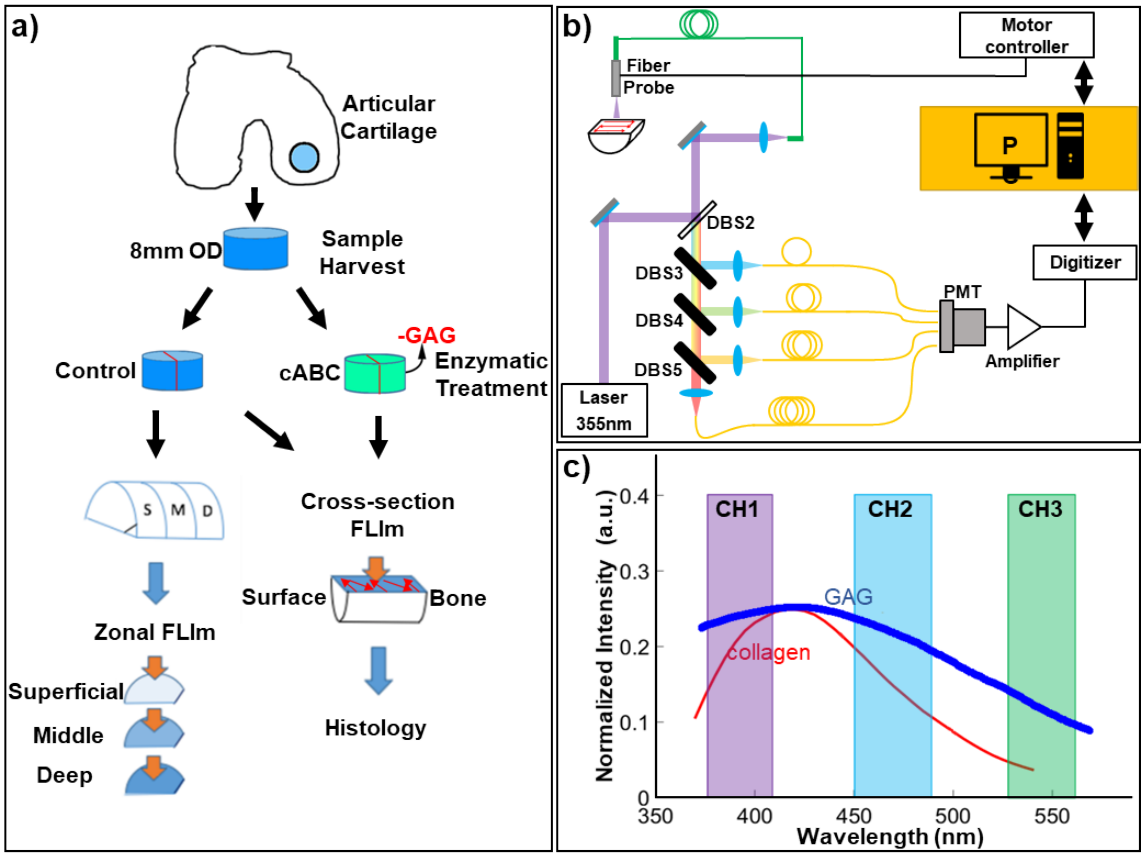

Figure 3.1 (a) Schematic diagram of the study protocol. Harvest and treatment of bovine articular cartilage samples in untreated (control) and chondroitinase ABC (cABC) groups. Zonal *en-face* imaging was conducted on samples from different depths of cartilage from control group. Cross-sectional imaging was conducted on both control and cABC treatment groups. (b) Schematic diagram of the FLIm imaging system. FLIm images were acquired by raster scanning of the optical fiber. (c) Spectral channels of the FLIm instrument: channel 1 = 375-410 nm, channel 2 = 450-485 nm, channel 3 = 530-565 nm. The reference emission spectrum of collagen (red) and GAG (blue) **[124]** were also overlaid.

3.2.4. FLIm Instrumentation

FLIm images were acquired using a prototype fiber-based point scanning principle and system which had been previously reported [125, 126]. A schematic of the system is shown in Figure 3.1b.

A frequency tripled Nd:YAG microchip laser (STV-02E-1x0, TEEM photonics) with repetition rate of 4K and pulse width of 600 ps was used as the fluorescence excitation light source. Fluorescence excitation and emission were guided to and from the target by a single 400 μm core diameter all-silica multimode fiber (FVP400440480, Polymicro). A wavelength selection module was used to separate fluorescence emission into three non-overlapping spectral bands (channel 1 = 375-410 nm, channel 2 = 450-485 nm, channel 3 = 530-565 nm) (Figure 3.1c). The spectral channels were temporally separated by passing the emission pulse through three delay fibers (FVP400440480, Polymicro) of different lengths. A single microchannel-plate photomultiplier tube (R3809U-50, Hamamatsu) detector was used to detect the temporally multiplexed signal. Neutral Density (ND) filter with ND=1.3 was used to attenuated signals in detection channel 1 and 2 so all spectral channels had similar signal intensity. Raster scanning was achieved using a motorized 3-axis translation stage (MX80L, Parker) with scanning speed up to 500 mm/s. FLIm images were acquired with 200 μm or 400 μm square pixel size over a 10 mm by 10 mm scanning area. The data acquisition time for each pixel was 8 ms, and the scanning speed was determined based on desired pixel size.

3.2.5. FLIm parameters

Following the acquisition of the fluorescence decay signal, non-negative constrained least-square deconvolution based on the Laguerre expansion method was performed to determine the fluorescence response of cartilage samples [127]. The average LT and intensity ratios were derived from the deconvolved fluorescence decay. The average LT was defined as the average amount of time a fluorophore stays in the excited state. Mathematically, it is the expected value of the probability distribution of detected photons which was obtained by normalizing the deconvolved decay by the total area under the curve. Intensity ratios were defined as the ratio of fluorescence

intensity at each channel to the sum of all three intensity channels. The standard deviation of the recovered LT was < 0.1 ns.

3.2.6. Histology

After FLIm assessment, samples were fixed in 10% neutral buffered formalin, paraffin embedded, and then sectioned parallel to the imaging plane at 10 μm. The sections were stained with hematoxylin and eosin (H&E) for general morphology, safranin O for GAG, and picrosirius red (PSR) for total collagen following routine procedures. The sections were imaged using an inverted microscope (BZ-X700, Keyence).

3.2.7. Fluorescence lifetime vs. distance from cartilage surface

To study the variability of fluorescence LT inside the cartilage tissue, we studied the change of fluorescence LT as a function of distance from the cartilage surface. To determine the distance from the cartilage surface of each pixel, the location of cartilage surface in cross-sectional images was first determined by finding the pixels with maximum fluorescence emission intensity gradient. Those pixels were used as a reference point for distance calculation. After that, the distance to cartilage surface of every pixel inside cross-sectional LT images was calculated. A distribution of fluorescence LT at a given distance can be generated by combining data from all cross-sectional images (n=3).

3.2.8. Region of Interest selection

ROIs were drawn manually based on the amount of safranin O staining in histology images. The GAG depleted region that had no, or minimal safranin O staining was segmented manually as ROIs for data analysis. The thickness of each ROI, average value of fluorescence LT, and intensity ratio within each ROI were calculated and used for statistical analysis.

3.2.9. FLIm image segmentation

A simple threshold-based segmentation algorithm was developed and tested for its ability to detect GAG depletion in cross-sectional FLIm images. Channel 1 intensity ratio was used as the parameter for the segmentation algorithm and 0.25 was set as the threshold based on receiver operating characteristic (ROC) analysis. The average depletion thickness was calculated and used for statistical analysis.

3.2.10. Statistics

In this study, n=25 biopsy samples were harvested from the same joint. We used n=3 to study the depth dependent lifetime of native cartilage. We used the remaining n=22 (control = 7, low cABC = 8, high cABC=7) to study the effect of GAG loss on cartilage fluorescence properties. Two samples were excluded from data analysis due to improper histology sectioning, resulted in the final total sample number of n=20 (control: n=6, low cABC: n = 8, high cABC: n = 6). Statistical analysis was performed using Student's t-tests and one-way ANOVA with Tukey's post-hoc analysis, where applicable. All statistical analysis was performed with R Statistical Software (Foundation for Statistical Computing, Vienna), and $p < 0.05$ were considered statistically significant.

3.3 Results

3.3.1. Depth dependent lifetime of native articular cartilage

Cross-sectional FLIm images (Figure 3.2a) showed that fluorescence LT in channel 1 varied with cartilage depth. The region closest to the cartilage surface had a LT of 5.7 ± 0.12 ns while the middle and deep part of cartilage had a longer LT of 6.1 ± 0.08 ns ($p<0.0001$). The same trend was also presented in the zonal FLIm images (Figure 3.2a). This was further confirmed by the violin

plot as the distributions of LT from both cross-sectional and zonal imaging shifted to higher LT values in middle and deep zone (Figure 3.2b). This trend was observed for all samples as depicted by the boxplot of LT distribution from all samples (n=3) which demonstrated that the LT increases with distance from cartilage surface. This increase was most noticeable within 500 μm from the surface (Figure 3.2c). In addition, changes of fluorescence LT were also associated with morphological heterogeneities. Macro-structures with shorter LT were also presented in both cross-section and *en-face* FLIm LT images (Figure 3.2a). No significant depth dependent LT changes were observed in other spectral channels.

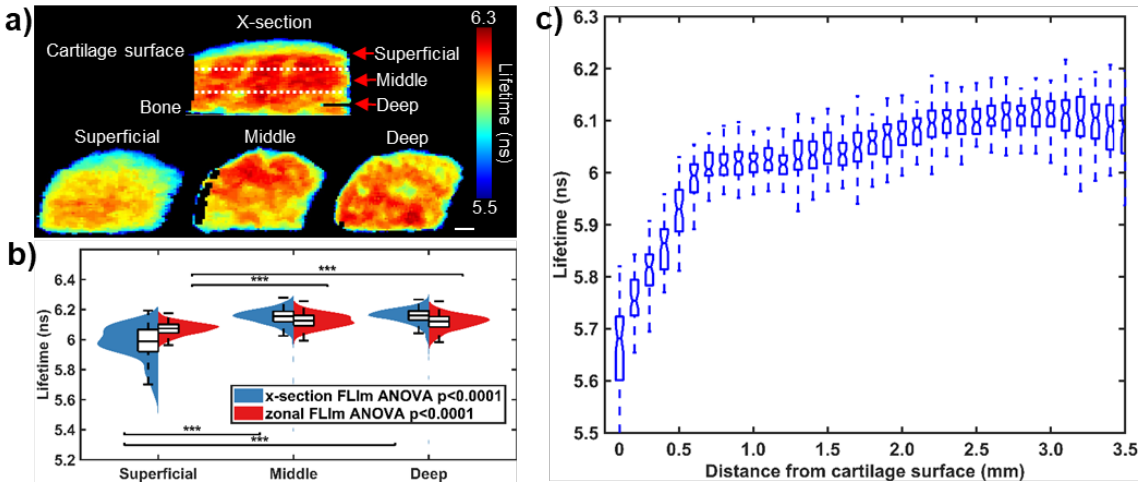

Figure 3.2 Channel 1 (375-410 nm) fluorescence LT increases with distance from articular cartilage surface (n=3). (a) Representative cross-section and zonal FLIm image of native bovine articular cartilage. Scalebar = 1 mm. Dashed line represents estimated location of cut of superficial, middle, and deep zone. (b) Violin plot of LT distribution of different zones of articular cartilage acquired through zonal and x-section imaging. The LT of superficial zone is significantly lower than that of middle and deep zones (***p<0.001). (c) A Box plot of average LT vs distance from cartilage surface for all samples (n=3). Each box represents all data points from all samples at the corresponding distance from cartilage

surface. Five values are highlighted: the extremes, the upper and lower quantiles, and the median. A clear increase of LT with distance from cartilage surface is observed. The increase is most prominent within the first 0.5 mm of cartilage surface.

3.3.2. Detection of GAG-depletion using FLIm

Safranin-O stained histology images showed that compared to untreated (control) cartilage, enzymatic treatment of cABC almost completely depleted GAG content within 1 mm distance from cartilage surface (Figure 3.3a). The depletion of GAG resulted in significant decreases in fluorescence LT in both detection channel 2 ($p<0.05$) and channel 3 ($p<0.01$) and significant changes in the intensity ratios in all collection channels ($p<0.0001$) (Figure 3.3b).

A segmentation algorithm based on channel 1 intensity ratio was able to identify regions of GAG depletion in both low and high cABC treated FLIm images (Figure 3.4a). Untreated control group had an average depleted layer thickness of ~0.1 mm while low (1 U/mL) and high (2 U/mL) C-ABC concentration treatment resulted in an average depletion layer thickness of 0.3 mm and 0.7 mm respectively. Average depletion thickness from high cABC treatment group was significantly higher than that of control (untreated) ($p<0.01$) and low cABC ($p<0.01$) treatment group. However, no significant difference was observed in average depletion region thickness between control and low cABC treatment group (Figure 3.4b).

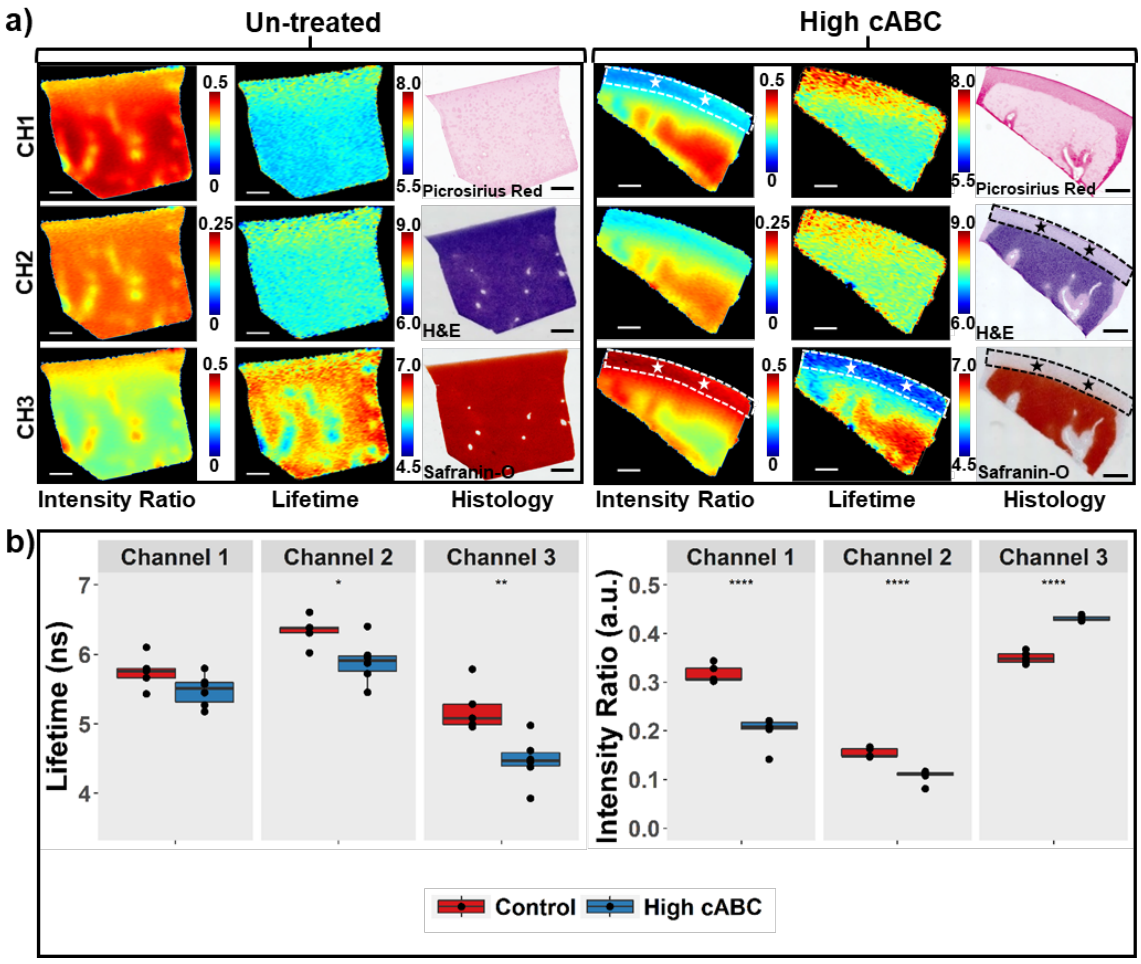

Figure 3.3 FLIm detects GAG depletion in articular cartilage. (a) Representative fluorescence cross-sectional intensity ratio images, LT images and histology images of untreated and treated bovine articular cartilage. ROIs highlight the region of GAG depletion in histology images of cABC treated sample. The corresponding region in FLIm LT and intensity ratio images are highlighted by ★. The GAG depletion region appears in FLIm maps with higher intensity ratio and lower LT in channel 3 as well as lower intensity ratio in channel 1. No GAG depletion is observed for control sample. Scalebar = 1 mm (n>=6 per group). (b) Box plot of ROI average LT from all samples in Control and High cABC group. Significant LT differences are observed in channel 2 (450-485 nm) *p<0.05

and channel 3 (530-565 nm) **p<0.01. Significant differences in intensity ratio are observed in all channels ****p<0.0001.

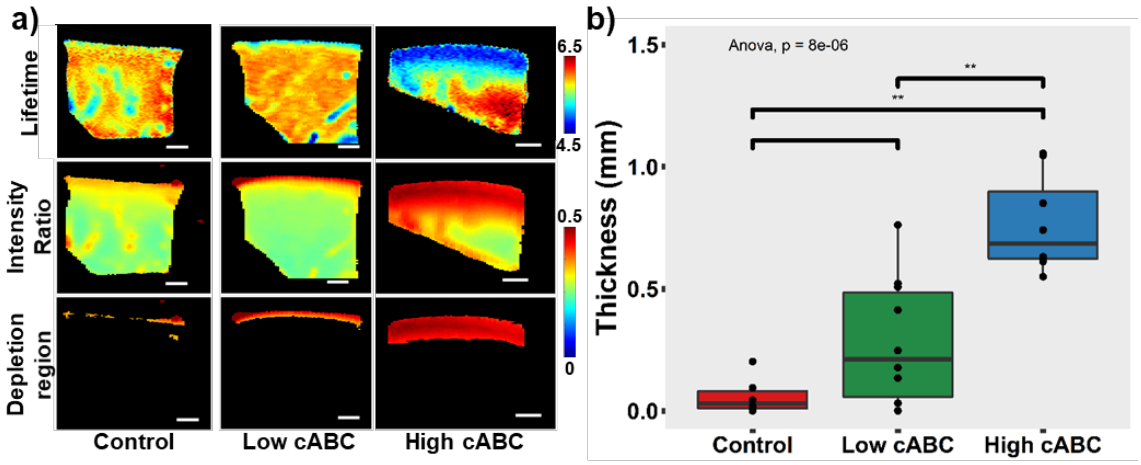

Figure 3.4 (a) Representative cross-sectional FLIm LT and intensity ratio images of cartilage without treatment and cartilage treated with high (2 U/mL) and low (1 U/mL) concentration of cABC. The depleted region is segmented using channel 1 intensity ratio of 0.25. Scalebar = 1 mm. (b) Box plot of the thickness of the GAG depleted layer calculated from segmentation result **p<0.01 (n>=6 per treatment group).

3.4 Discussion

This study demonstrated that 1) fluorescence LT of articular cartilage varies across its depth; shorter LT values were observed for the superficial zone of cartilage when compared with the middle and deep zones, and 2) the depletion of GAG can be detected using FLIm and the level of GAG depletion in articular cartilage can be inferred using fluorescence-based parameters. Both of the above points demonstrate that FLIm can detect biochemical changes in cartilage tissue and has great potential for early detection of cartilage disease.

To our knowledge, this is the first study to map the fluorescence features of native bovine articular cartilage across its full thickness. The cross-sectional imaging protocol allowed us to

study changes in FLIm parameters as a function of depth. The comparison of LT distribution obtained from cross-sectional imaging and that from conventional *en-face* imaging cross-validated the results. Given the complex zonal variation of cell morphology, collagen fiber orientation, and biochemical composition in articular cartilage [7], the change of fluorescence LT across the thickness of cartilage is expected. Current results are in agreement with earlier studies conducted on articular cartilage that showed shorter LT for the superficial layer relative to middle and deep zone of the cartilage [128] and a previous study that validated *en-face* FLIm parameters with biochemical assays [129]. These results, in conjunction with the fiber-based platform, allow for ease of translation into imaging in humans *via* augmentation of the current clinical practice of arthroscopy. By incorporating the optical fiber into a conventional viewing scope, this technique would enable straightforward visual evaluation of the integrity of the cartilage surface and inner structures, allow spatial or temporal monitoring during disease development, and allow clinicians to monitor the biochemical changes occurring within the patient.

Apart from the change of fluorescence LT as a function of depth, macro-structures presented in both cross-section (shape of tunnel) and *en-face* (round shape) exhibit shorter LT when compared with the surrounding cartilage mass. Since cartilage from juvenile bovine condyles was used in this study, these micro-structures could be cartilage canals that present only in the early stage of cartilage development [130]. Since cartilage canals have different biochemical composition when compared with the collagen-rich cartilage ECM, it is expected that these micro-structures exhibit a different LT. This demonstrated that FLIm could be a potential tool for studying basic biochemical properties associated with structural heterogeneities of cartilage as well. To date, much is known about articular cartilage organization and ECM, but less is known about its developmental biology. How articular cartilage grows and matures into a complex, functional

and multifaced structure is still unclear. FLIm could help advance our knowledge in these research areas by monitoring the change of biochemical properties of native articular cartilage during its development and along its depth. The advances will have significant impact for basic science and potential translational value to the design of superior cartilage regeneration and rapier strategies.

The finding that the depletion of GAG significantly altered the fluorescence features of articular cartilage tissue, and the change could be detected using our FLIm instrumentation is of critical importance for the research of OA diagnosis, as GAG loss is the first indicator for early OA development. This could enable early diagnosis of OA before clinical symptoms like pain and cartilage loss appear.

We acknowledge that the freeze-thaw cycles of the cartilage tissue before imaging lyses the cells and could alter cartilage fluorescence properties. Thus, the experimental conditions reported in this study might not fully mimic conditions encountered in the clinical application. In a separate study conducted on articular cartilage using the same FLIm instrumentation, we showed that the freezing process results in decreases in Channel 1 LT (Δ=0.14; p=0.003) and significant increases in Channel 2 LT (Δ=0.11; p=0.003) and Channel 3 LT (Δ=0.22; p=0.003) compared to fresh tissue. However, the changes were small compared to those induced by the loss of GAG which resulted in a significant decrease of fluorescence LT values in channel 2 (Δ=0.44 ns; $p<0.05$) and channel 3 (Δ=0.75 ns; $p<0.01$). The small differences in FLIm LT values with cell lysis could be attributed to the very low (~ 10% by volume) composition of cells within cartilage tissue.

Interestingly, collagen was more densely packed in the region of GAG depletion post cABC treatment. This was represented in picrosirius red stained histology as an increase in color saturation in the ROIs. In healthy cartilage, the collagen network is slightly stretched due to the

Donnan osmotic pressure caused by GAG content that provides its compressive stiffness [7]. Thus, the loss of GAG would lead to a slightly denser collagen matrix.

GAG loss resulted in a significant decrease in the intensity ratio of channel 1 and 2 which represents collagen and a significant increase in the intensity ratio of channel 3 which represents GAG. This non-intuitive change could be attributed to the conformational change of collagen structure inside cartilage tissue. It is well known that collagen cross-links strongly fluoresce. The loss of GAG could result in the breakdown of collagen cross-links which was not quantified in this study. Thus, the loss of GAG very likely resulted in the loss of absolute intensity in all spectral channels, but the loss in channels 1 and 2 were more prominent due to the high quantum yield of collagen and its cross-links. As intensity ratio characterizes the relative intensity contribution of each channel instead of absolute intensity, a higher absolute loss in channels 1 and 2 will result in a decrease in channel 1 and channel 2 intensity ratios and a higher channel 3 intensity ratio.

The decrease of fluorescence LT in channel 2 and channel 3 is a result of the intensity ratio change. Collagen is the dominant fluorophore in cartilage and has the highest fluorescence lifetime (~5.5 ns) of the major constituents[121]. The decrease of intensity ratio in channel 1 and channel 2 indicate a lower contribution from collagen which would result in a significant decrease of fluorescence lifetime in all channels. There is no significant change of fluorescence lifetime in channel 1 as collagen fluorescence completely dominates this channel. Channel 3 had the largest lifetime decrease as it sits at the tail of collagen emission spectrum and the collagen contribution is less dominant.

A threshold-based segmentation algorithm could distinguish high levels of GAG depletion in our cABC-treatment group from the control group using one of the many fluorescence parameters. However, intensity measurement is highly sensitive to the excitation and collection

geometry. Any change of excitation and collection geometry could lead to significant measurement error. On the other hand, fluorescence LT is robust to the change of measurement conditions. Thus, the effectiveness and robustness of our instrumentation to detect early OA could be further improved by including more FLIm parameters. Nonetheless, we demonstrated that parameters from non-invasive FLIm imaging can successfully detect GAG depletion in articular cartilage.

We employed raster scanning by a translation stage in this study to automate the scanning process. In a clinical setting, the fiber-based interface can be introduced through a standard clinical arthroscope with the FLIm imaging data overlaid on the arthroscope image on the surgical monitor. We have previously demonstrated this concept using a hand scanning probe[131] for interrogation of breast cancer tumors. Real time FLIm data was overlaid on conventional white light images of the tissue[28], providing valuable real time feedback to the surgeons. When combined with machine learning algorithms, real time classification was also possible, providing potential real-time disease discrimination[131].

We acknowledge that the cross-section imaging approach used in this study is different from an arthroscopy imaging situation. Future *en-face* imaging will be required to properly assess the performance of FLIm instrumentation for detection of OA and its usefulness in the clinical environment. Furthermore, we acknowledge that FLIm is only a surface imaging modality with a penetration depth of ~300 μm and is not able to provide any structural information regarding the integrity of articular cartilage. However, FLIm can be adapted to tissue interrogation in endoscopic-like configurations [132, 133], thus it can complement other structural imaging modalities like ultrasound and OCT. This study serves as an important step towards early diagnosis of OA and encourages further investigation into the feasibility of *in vivo* FLIm arthroscopy.

3.5 Conclusion

This study demonstrates that GAG degradation in articular cartilage can be detected by rapid, non-destructive, fiber-based FLIm. This technique could be utilized as a potential tool for basic research of cartilage. In addition, the size of the miniature fiber probe, the clinically compatible high imaging speed, and the potential for multi-mode imaging such as FLIm-OCT [134] make it a promising tool for the early diagnosis of osteoarthritis. This technique has great potential to facilitate a paradigm shift from palliation of late disease towards osteoarthritis prevention and early intervention.

Chapter 4 Multimodal fluorescence lifetime imaging and optical coherence tomography for longitudinal monitoring of tissue engineered cartilage maturation in a pre-clinical implantation model

Cartilage tissue engineering is a promising strategy for effective curative therapies for treatment of osteoarthritis. However, in both research and clinical settings, tissue engineers depend predominantly on time-consuming, expensive, and destructive techniques as quality control to monitor the maturation of engineered cartilage. This practice can be impractical for large scale biomanufacturing and prevent spatial and temporal monitor of tissue growth which are critical for the fabrication of clinically-relevant-sized cartilage construct. Non-destructive multimodal imaging techniques combining fluorescence lifetime imaging (FLIm) and optical coherence tomography (OCT) hold great potential to address this challenge. In this chapter, the feasibility of using FLIm-OCT for nondestructive, spatial, and temporal monitoring of self-assembled cartilage tissue maturation is investigated in a pre-clinical animal model.

4.1 Introduction

Damage to articular cartilage, which can occur through traumatic injury, pathology, or age, often degenerates inexorably to osteoarthritis (OA). Unfortunately, adult articular cartilage has only limited ability to heal as cartilage tissue is avascular and hypocellular [135, 136]. A multitude of treatments have been developed for this age-long problem, but no satisfactory long-term therapies are established. In the United States alone, OA affects the quality of life for more than 54 million

Americans [3] and cost the economy exceeding $304 billion per year (both medical costs and lost wages) [4].

Cartilage tissue engineering is an emerging strategy at the threshold of clinical translation. It holds immense potential to improve the clinical outcome and deliver effective curative therapies for treatment of OA [14]. Currently, in both research and clinical settings, tissue engineers depend predominantly on a battery of time-consuming, expensive, and destructive techniques as quality control to monitor the composition, structure, and function of engineered tissue during culture [137]. Destructive testing can be inappropriate or impractical for large scale biomanufacturing as partial or complete sample loss is required. It has been estimated that 70% of the cost of tissue engineered goods can be attributed to quality control efforts [138].

Furthermore, destructive testing often prevents spatial or temporal monitoring during tissue maturation which are critical for fabrication of clinically-relevant-sized tissue construct. To date, small cartilage tissue constructs (~Ø 4 × 2 mm) with biochemical content and mechanical function approaching native cartilage have been successfully fabricated [129]. However, a major challenge remains in the development of clinically-relevant-sized tissue constructs, typically 15-25 mm in diameter and can be as great as 5 mm thick, which are required to repair OA defects [139]. Larger engineered cartilage constructs often suffer from highly heterogeneous matrix deposition and possess poor mechanical properties that are unable to support physiologic loading [140-142]. Therefore, there is an immediate need to develop nondestructive and noninvasive tools to not only verify the critical biochemical and structural component but also monitor the spatial and temporal growth of tissue-engineered cartilage product for both research and clinical applications.

Optical techniques have shown great potential to address this unmet need due to their capacity to probe tissue composition and structure spatially and temporally in a nondestructive and

noninvasive manner. Fluorescence lifetime based techniques are known to detect biochemical and functional alternations in tissue [28, 29]. Several endogenous fluorophores, including the extracellular matrix (ECM) structural proteins (e.g., collagen) and enzyme cofactors (e.g., NADH and FAD), are responsible for tissue autofluorescence [30]. Fluorescence lifetime imaging (FLIm) based on autofluorescence provides a sensitive method for label-free nondestructive monitoring of bioengineered tissues both *in vitro* and *in vivo*. The spatial distribution of tissue biochemical component can be mapped by FLIm, providing critical information to assess the heterogeneous growth of large engineered constructs. Recently, FLIm has been applied for the characterization of engineered vascular constructs [85], osteogenic grafts [143, 144] and cartilage constructs [44, 86].

Optical coherence tomography (OCT), which is based on low-coherence interferometry, is a nondestructive, noninvasive imaging modality analogous to ultrasound (US) imaging but uses near-infrared radiation rather than sound waves [145]. OCT is well recognized as a viable tool for studying the structure and morphology of biological tissue [146] for diagnosis of illnesses such as atherosclerosis [147], epithelial cancer [148], osteoarthritis [149], and for surgical guidance [150]. State of art OCT systems can image cartilage tissue at micron resolution (near-histological) and one to two millimeters in depth [149]. Real-time 2D cross-sectional or 3D volumetric scans are easily achievable. Compared with US, which has been used to evaluate engineered tissue constructs [44, 106, 151], OCT offers better resolution, higher imaging speed and easy integration with other optical imaging modalities. Recently, OCT has been explored as a promising tool for real time monitoring of the development and growth of tissue-engineered products [33].

The monitoring of tissue engineered cartilage will benefits from the bimodal diagnostic approach combining FLIm and OCT techniques. FLIm can investigate construct biochemical

composition but is limited to the thin layers (< 0.5 mm) within the penetration depth of UV light. In addition, little structure information of the tissue construct is retrieved. In contrast, OCT enables three-dimensional evaluation of tissue microstructure, morphology, and potential structural defects, but lacks information on tissue biochemical composition. Thus, FLIm and OCT can complement each other and together provide a more comprehensive, orthogonal, and noninvasive spatial characterization and evaluation of cartilage constructs than either modality alone. Moreover, the two modalities can be easily integrated using an optical fiber probe, enabling sterile, longitudinal assessment of engineered tissue [113]. The ability of FLIm-OCT to probe biochemical and structural component of tissue spatially and nondestructively makes it a promising tool for characterization of engineered cartilage tissue.

The overall objective of this chapter was to evaluate the ability of a bimodal system combing FLIm and OCT for nondestructive, spatial, and longitudinal monitoring of changes in biochemical and structural properties of self-assembled cartilage construct in a pre-clinical implantation model. A fiber-based multimodal FLIm-OCT system was used to realize label-free, nondestructive monitoring of key biochemical and structural markers at three key time points (t= 2 and 4 weeks *in vitro*, t = 4 weeks *in vivo*) during engineered tissue maturation without perturbing or compromising sample sterility. This approach is flexible and can be easily extended to environments such as bioreactors or incubators. Specifically, the goals of the current study were (1) to determine whether heterogeneous construct growth can be detected by bimodal FLIm-OCT *in vitro* and (2) to evaluate whether *in vivo* tissue maturation in pre-clinical animal model can be detected by bimodal FLIm-OCT.

4.2 Materials and methods

4.2.1. Chondrocyte Isolation

Articular cartilage was harvested from the femoral condyles of five juvenile bovine stifle joints (Research 89, Boston, MA) (Overview; Figure 4.1a), minced, and digested in Dulbecco's Modified Eagle Medium (DMEM) with high glucose/GlutaMAX™-I (Life Technologies, Grand Island, NY) with 0.3% collagenase type II (Worthington, Lakewood, NJ), 5% fetal bovine serum (FBS) (HyClone, GE Healthcare Life Sciences, Marlborough, MA), and 1% penicillin/streptomycin/ fungizone (P/S/F) (Lonza, Basel, Switzerland) for 18h on an orbital shaker at 37 °C. Following digestion, the cells were collected, pooled, filtered through 70 µm cell strainers, and washed three times with DMEM.

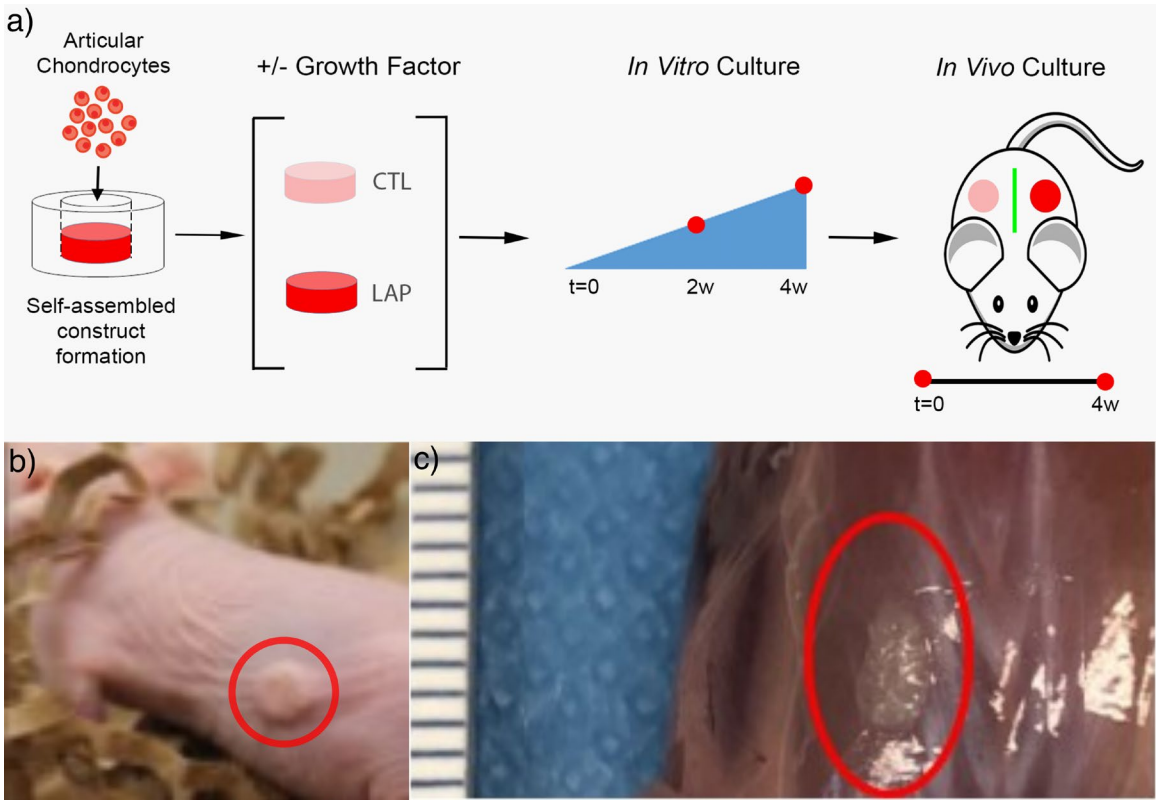

Figure 4.1 a) Schematic overview of the experiment design. Self-assembled constructs are treated with different growth factor and cultured *in vitro* for 4 weeks, followed by *in vivo* culture of another 4 weeks. Multimodal FLIm-OCT imaging was carried out at t = 2 weeks and 4 weeks (0 week *in vivo*) during *in vitro* culture and at t = 4 weeks for *in vivo* culture.

Red dots indicate imaging time points. b) Picture of tissue construct following implantation on the back of nude rat. c) Picture of engineered tissue after 4 weeks of *in vivo* culture following sacrifice of the animal.

4.2.2. *In vitro* self-assembled construct culture

Engineered cartilage constructs were formed using the self-assembling process, as described previously [12]. Briefly, 4×10^6 chondrocytes were suspended in 100 µL of control medium (CTL) consisting of DMEM with 1% ITS+ premix (BD Biosciences, Bedford, MA), 1% non-essential amino acids (NEAA) (Life Technologies), 50 µg/mL ascorbate-2-phosphate (Sigma-Aldrich, St. Louis, MO), 40 µg/mL L-proline (Sigma-Aldrich), 100 µg/mL sodium pyruvate (Sigma-Aldrich), and 100 nM dexamethasone (Sigma-Aldrich), and 1% P/S/F. Cell suspensions were seeded in 5 mm diameter, 2% agarose wells in 24-well plates (Costar, Corning, NY). After 4h, 400 µL of control medium were added to each well. Self-assembled constructs were cultured for 4 weeks in (1) CTL medium only (CTL) (5 samples) or (2) with recombinant human LAP TGF-β1 (LAP) (5 samples) (R&D Systems, Minneapolis, MN) [152] applied at 10 ng/mL for the entire culture duration. Constructs were removed from wells at day 5 and 1 mL of fresh media were exchanged daily.

4.2.3. *In vivo* self-assembled construct culture

Following 4 weeks of *in vitro* culture, constructs were implanted subcutaneously into the dorsal section of 5 nude mice (Figure 4.1b), in which the left side was the LAP group, and the right side was the CTL group. After 4 weeks of *in vivo* culture (Figure 4.1c), the mice were sacrificed, and all samples were harvested and processed for analysis.

4.2.4. Multimodal assessment of self-assembled articular cartilage

A multimode imaging system that combines two complementary techniques of FLIm and OCT was utilized to make nondestructive assessment of the engineered cartilage construct at 2 weeks and 4 weeks of *in vitro* culture (n=5 per group) and 4 weeks of *in vivo* culture (n=4 per group) as shown in Figure 4.1a. Samples were imaged using FLIm (resolution of 100 μm) first then followed immediately by OCT in a sterile environment inside a biosafety cabinet with a resolution of 100 μm. Matched samples were assessed nondestructively (FLIm-OCT) at all time points and histological analysis was performed at 4 weeks *in vivo*.

4.2.5. Multispectral FLIm instrument

The multispectral FLIm sub-system has been reported in detail in previous publications [61]. Briefly, a Q-switched pulsed 355 nm microchip laser (STV-02E-1x0, TEEM photonics, Grenoble, France) with 2 μJ pulse energy and 600 ps pulse duration was used to excite sample autofluorescence through a flexible fiber-optic probe consist of 400 μm core diameter pure silica multimode fiber (FVP400440480, Polymicro Optical Fiber, Molex, IL). Sterile imaging is achieved by raster scanning the fiber probe across the surface of the sample using a three-axis translation stage (LP28, Parker, Cleveland, OH) housed inside a biosafety cabinet. During scanning, each sample was placed inside a sterile 35 mm glass bottom dish (MatTech Corporation, Ashland, MA) in phosphate-buffered saline at room temperature. Sample autofluorescence emission was separated into 4 distinct spectral channels (CH1 = 375-410 nm, CH2 = 450-485 nm, CH3 = 532-565 nm, CH4 = 595-660 nm) using a custom-built wavelength selection module, time-multiplexed using optical fibers of different length, detected by a single microchannel plate photomultiplier tube (MCP-PMT) and digitized by a high-speed digitizer (PXIe-5185, National Instrument, Austin, TX) with a time resolution of 80 ps. Complete mapping of the sample surface was achieved under 1 minute at a resolution of 100 μm resolution.

4.2.6. FLIm parameters

Following the acquisition of the fluorescence decay signal, non-negative constrained least-square deconvolution based on the Laguerre expansion method was used to recover the fluorescence response of the tissue sample [99]. The average lifetime and intensity ratio were derived from the deconvolved fluorescence decay. The average lifetime is defined as the average amount of time a fluorophore stayed in the excited state. Mathematically, it is the expected value of the probability distribution of detected photons, which was obtained by normalizing the deconvolved decay by the total area under the curve. Intensity ratios were defined as the ratio of fluorescence intensity at each channel to the sum of all three intensity channels.

4.2.7. OCT instrument

The OCT sub-system is a swept source OCT (SS-OCT) based on an OEM OCT engine from Axsun Technology [115]. Briefly, it includes a 1310 ± 55 nm swept-source laser with 50 mW output power and a native A scan rate of 50 kHz. The OCT interferometry is realized with fiber couplers and circulators that split the laser output into sample and reference arms and recombine the reflected light from both arms. A single-mode fiber (SMF-28 Ultra) is used in the reference arm to match the optical path length of the optical fiber probe consist of the same single-mode fiber with a Graded-Index (GRIN) lens (1.8 mm diameter, 11 mm long, 0.25 pitch, 0.2 NA) attached at the distal end. The interference signal is detected by the on-board dual balanced detectors and sampled by the 12 bit, 500 MS/s FPGA DAQ board in the OCT engine. Depth-resolved OCT B-scans are generated in real-time by the onboard FPGA processor and streamed to the experimental control computer for visualization. The OCT system has an axial resolution of 10.2 μm and a transverse resolution of 16.3 μm in the focal plane.

4.2.8. Multivariate analysis of FLIm parameters

Pixel-wise Pearson correlation coefficients between all fluorescence lifetime images (channel 1 - 4) and intensity ratio images (channel 1 – 4) were analyzed using MATLAB (MathWorks, Natick, MA). Image data were filtered by a threshold signal-to-noise (SNR) value of 25 in channel 3 (channel with lowest signal intensity) to remove data point with low SNR. The same filter is applied to data from all channels to ensure that the dimension the data are identical. The correlation coefficient was averaged across all images irrespective of treatment or imaging time point. The correlation matrix is visualized using R statistical software (Foundation for Statistical Computing, Vienna) and $p < 0.05$ were considered statistically significant.

4.2.9. Biochemical homogeneous index

Statistical homogeneity theory [153] was used to determine tissue homogeneity using FLIm lifetime data of all channels. FLIm channel 1 lifetime is chosen based on the result of multivariant analysis of FLIm parameters. To compute the homogeneity index, a ring-shaped region of interest centered on the centroid of the tissue image is first selected so that the area of the ROI is half of the total area of the sample. The mean fluorescence lifetime of the ROI is computed. The percentage of the FLIm pixels inside the ROI that falls between $(1 \pm 0.05) \times$ mean lifetime is defined as the homogeneity index. If all the pixels inside the ROI falls within $(1 \pm 0.05) \times$ mean lifetime, the homogeneity index would be 1.

4.2.10. Histology

All samples were harvested from the back of mice following FLIm-OCT assessment at 4 weeks *in vivo* and fixed in 10% neutral buffered formalin, paraffin embedded, sectioned at 10 μm and

stained with hematoxylin and eosin (H&E) for general morphology. The sections were imaged using an inverted microscope (BZ-X700, Keyence).

4.3 Results

4.3.1. FLIm detects heterogeneous construct growth

Non-destructive FLIm assessment of engineered tissue construct during *in vitro* culture revealed heterogeneous tissue growth in all constructs at t = 2 weeks and t = 4 weeks for both treatment groups. A representative FLIm images of tissue construct at t = 4 weeks is shown in Figure 4.2. The outer edge of the tissue construct exhibited higher lifetime (Ch1: 3.1171 ± 0.2371 ns; Ch2: ~3.3606 ± 0.2593 ns) and intensity ratio than the center of the construct (Ch1: 2.8861 ± 0.1290 ns; Ch2: 3.1878 ± 0.0970 ns) in both channel 1 and 2. Relative homogeneous lifetime is observed in channel 3 (2.7060 ± 0.1162 ns) and 4 (2.8977 ± 0.1201 ns) with lower intensity ratio on the outer edge of the tissue construct. A defect (void) was observed in the center of the tissue construct.

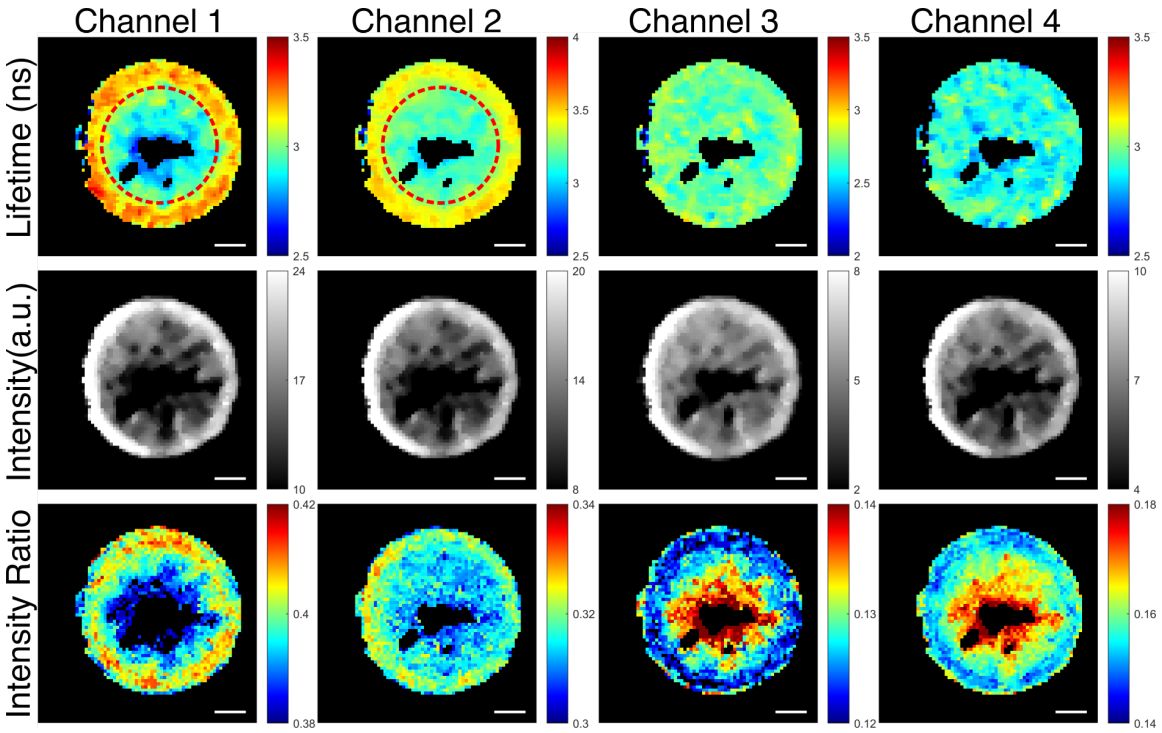

Figure 4.2 Representative FLIm maps of engineered tissue sample from LAP group at t = 4 weeks during *in vitro* culture. Heterogenous growth of tissue construct was observed. The outer edge of the tissue sample exhibited higher lifetime and intensity ratio in FLIm channel 1 and 2. Relative homogenous lifetime across the whole construct was observed in Channel 3 and 4 with lower intensity ratio at the outer edge. Scale bar = 1 mm.

4.3.2. Multivariant analysis of FLIm data

Correlation matrix between all FLIm maps, irrespective of treatments or time point, is shown in Figure 4.3a. The standard deviation of the correlation matrix is shown in Figure 4.3b. All fluorescence lifetimes (LT1, LT2, LT3, LT4) are correlated with each other. Among them, the highest correlation coefficient (0.8) exists between channel 1 lifetime (LT1) and channel 2 lifetime (LT2) with the lowest standard deviation of 0.08. Among intensity ratios, strongest correlation (0.8) is observed between channel 3 intensity ratio (INTR3) and channel 4 intensity ratio (INTR4) with the lowest standard deviation of 0.1. Channel 1 intensity ratio (INTR1) is inversely correlated with the intensity ratio of channel 3 (INTR3) and channel 4 (INTR4) with identical coefficient but positively with channel 1 lifetime (LT1) and channel 2 lifetime (LT2). Between lifetime and intensity ratios, channel 3 and channel 4 lifetime has a weak or no correlation between all intensity ratios. Channel 1 intensity ratio (INTR1) is strongly correlated to channel 1 lifetime (LT1) and channel 2 lifetime (LT2).

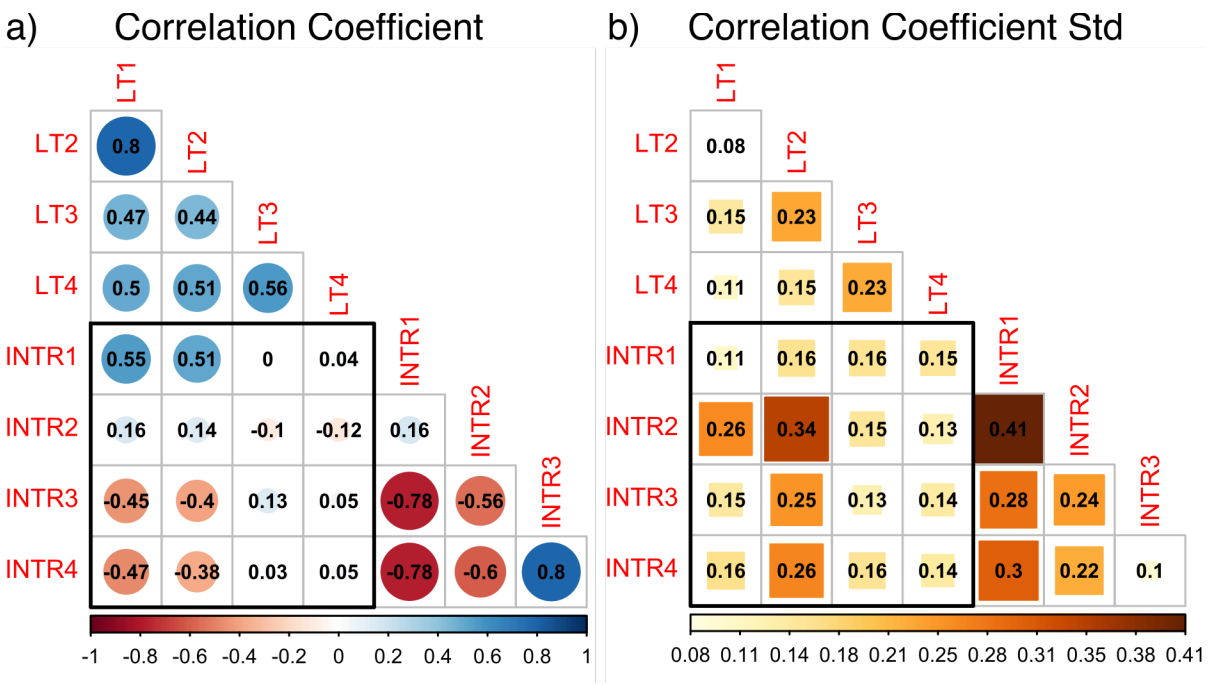

Figure 4.3 Multivariant analysis of FLIm lifetime and intensity ratios of channel 1 to 4. a) Correlation coefficient between FLIm lifetime and intensity ratios. The size of the circle indicates the absolute value of the correlation coefficient. b) Standard deviation of correlation coefficient between FLIm lifetime and intensity ratios. The size of the square indicates the absolute value of the standard deviation. LT: lifetime; INTR: intensity ratio. Black squares highlight the coefficient between lifetimes and intensity ratios.

4.3.3. Longitudinal FLIm assessment of construct maturation

Longitudinal FLIm assessment detects changes of tissue construct homogeneity index during *in vitro* culture. FLIm images of sample 2 from CTL group at t = 2 weeks and t = 4 weeks of *in vitro* culture is shown in Figure 4.4a and Figure 4.4d respectively. The ROI used for homogeneity index calculation is shown in Figure 4.4b and Figure 4.4e. The histogram of the fluorescence lifetime inside the ROI is plotted in Figure 4.4c and Figure 4.4d respectively. The homogeneity index of the tissue sample is higher for t = 4 weeks as more (82 %) of the pixels in the ROI falls between ±

10% of the mean lifetime of ROI, compared to that of week 2 (62 %). A bar plot of HI at t = 2 weeks and t = 4 weeks for CTL and LAP group is shown in Figure 4.5. Significant increase of HI is observed between week 2 and week 4 for both CTL and LAP group. No significant difference is observed between group at either time point.

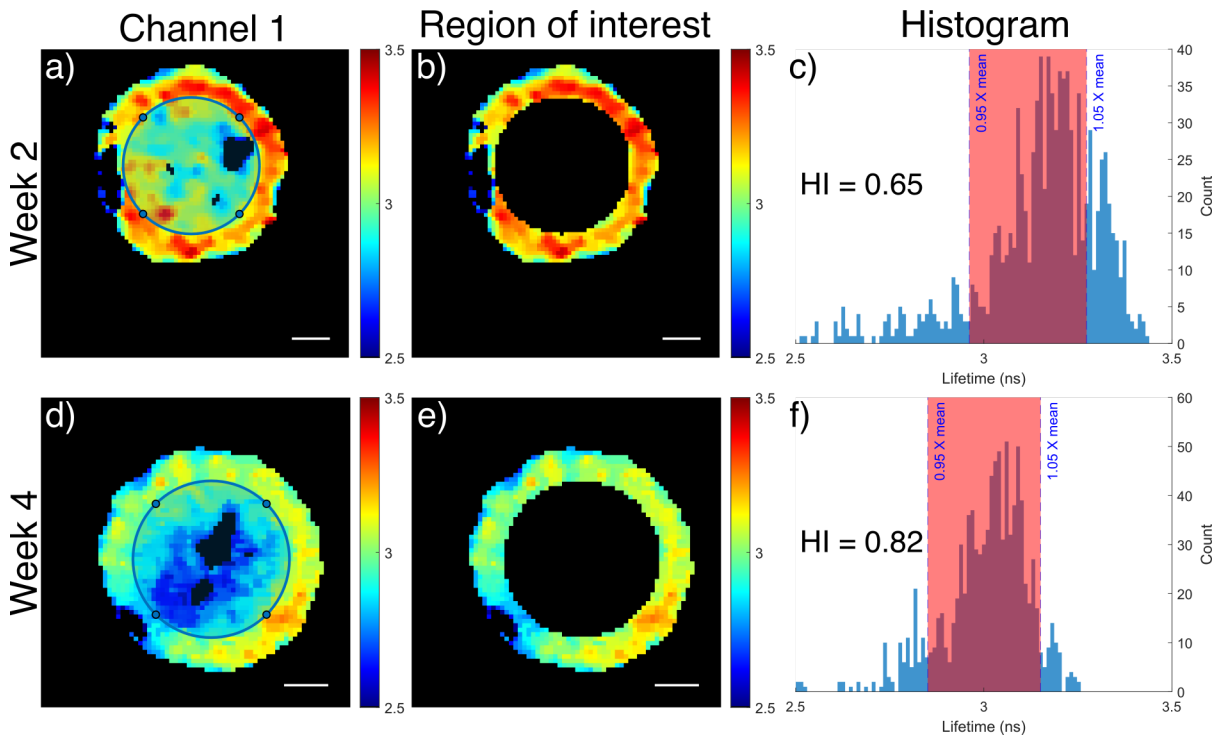

Figure 4.4 Longitudinal FLIm assessment detects tissue construct maturation. Channel 1 FLIm image, region of interest used for calculation of homogeneous index and the histogram of lifetime inside the region of interest is shown.

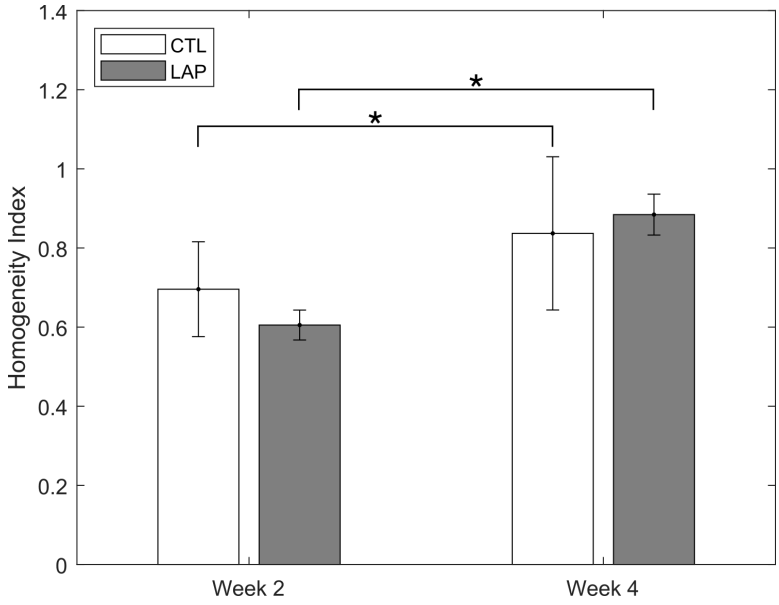

Figure 4.5 Homogeneity Index of tissue construct. Significant increase ($p < 0.05$) of HI is observed between week 2 and week 4 for both CTL and LAP group. No significant difference is observed between groups at either time points. * : $p < 0.05$

4.3.4. OCT detected structural defect in tissue construct

Non-destructive OCT assessment of the tissue construct during *in vitro* culture discovered defects (voids) at the center of tissue construct at both t = 2 weeks and t =4 weeks, in agreement with FLIm assessment. A representative 3D volume rendering of the tissue construct (same sample as Figure 4.2) is visualized in Figure 4.6a. A B-scan image from the center of the construct is shown in Figure 4.6b, the location of the B-scan is indicated by red line in the enface projection of the OCT 3D volume data shown in Figure 4.6c. Tissue morphology measured by OCT matched well with that from fluorescence lifetime (Figure 4.6d) and intensity (Figure 4.6e) map.

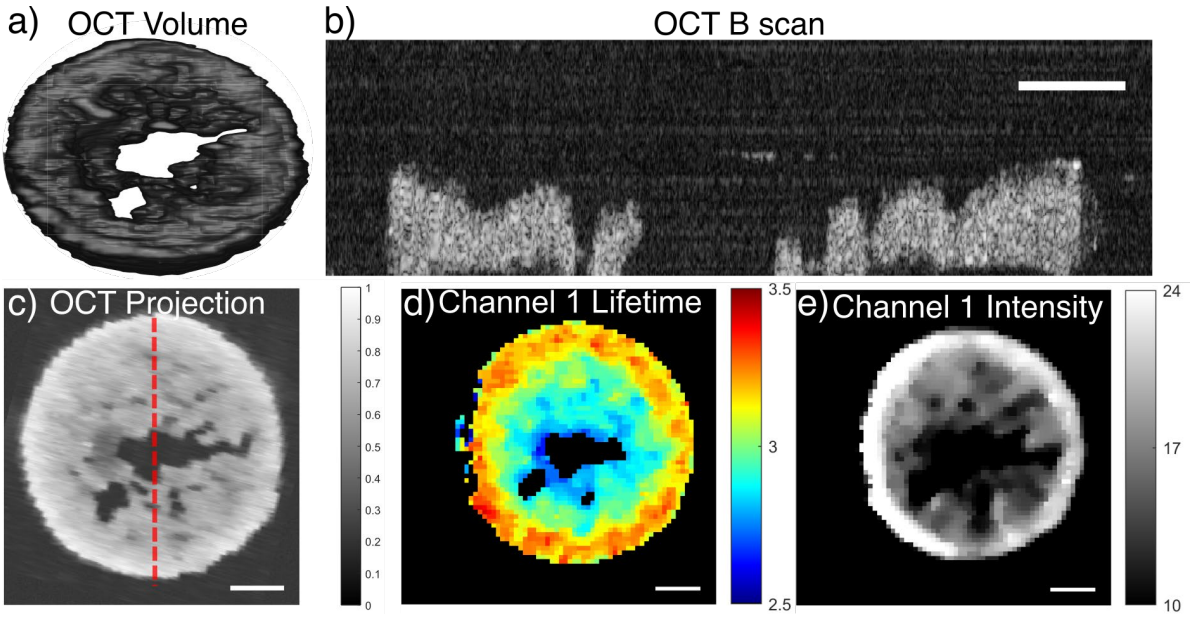

Figure 4.6 Non-destructive OCT assessment detected defect (void) in tissue construct. Matched sample with Figure 4.2. a) 3D volume rendering of tissue construct. b) OCT B-scan from the center of the tissue construct, location indicated by red line in OCT projection. c) Enface projection of the 3D volumetric OCT data. d) Channel 1 fluorescence lifetime map of the sample. e) Channel 1 fluorescence intensity map of the tissue sample.

4.3.5. Visualization of construct *in vivo* by FLIm-OCT

Representative *in situ* FLIm and OCT images of tissue construct at t = 4 weeks of *in vivo* culture are shown in Figure 4.7. The tissue construct retained its hyaline color as shown in the white light image (Figure 4.7a) while the size of the construct was reduced compared to t = 4 weeks *in vitro* (Figure 4.2). Tissue construct is visible in OCT B-scan image with distinct morphology from the muscle tissue of the mouse which has a layered structure and smooth surface. The lifetime of tissue construct exhibits lower lifetime (4.36 ±0.22 ns) in channel 1 compared to the surrounding native tissue (~ 5 ns – 6 ns). The opposite is observed for channel 3 with tissue construct exhibit longer lifetime (2.58 ± 0.24 ns) compared to the native tissue (~ 1 ns – 2.5 ns).

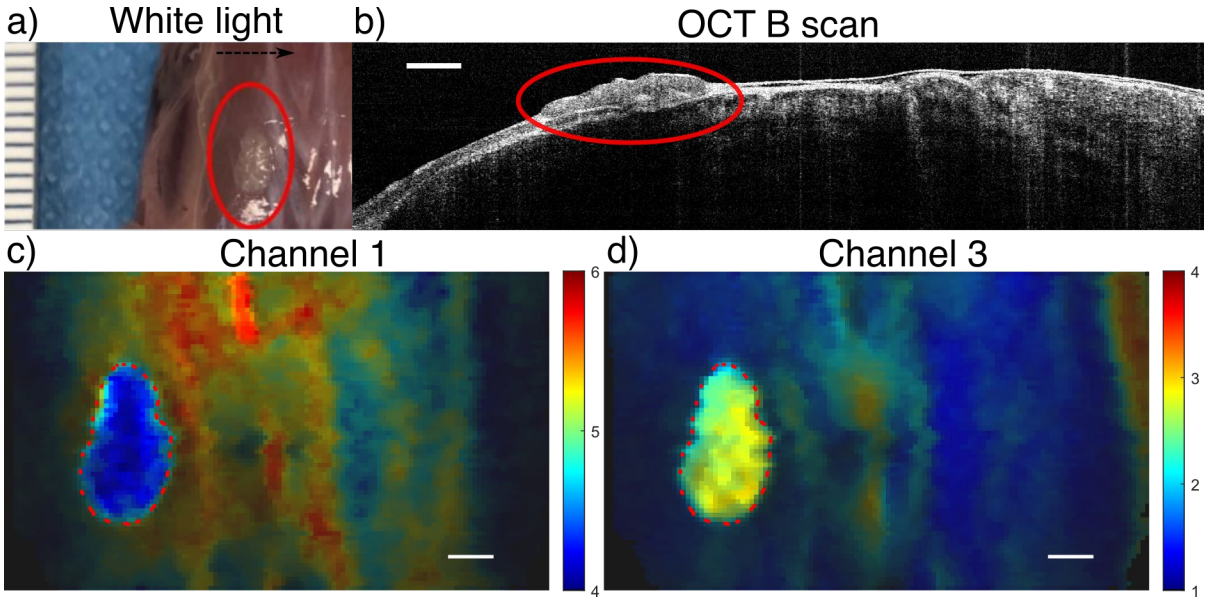

Figure 4.7 In situ FLIm and OCT image of cartilage construct on the back of nude mouse at t = 4 weeks of *in vivo* culture. a) White light image of the construct. Black arrow indicates scanning fast axis direction. b) OCT B-scan image from the center of the construct. c) FLIm channel 1 intensity weighted lifetime map. Construct ROI highlighted in red. d) FLIm channel 3 intensity weighted lifetime map. Construct ROI highlighted in red. Scale bar = 1mm.

4.3.6. OCT detects cyst formation in tissue construct

Comparison of *in situ* OCT B scan image with histology (H&E) showed that the formation of a cyst inside a CTL tissue construct that can be detected by OCT. The cyst was visualized in the OCT B-scan image as a hypoechoic region with low intensity as shown in Figure 4.8a. Histology (H&E) of the same tissue construct shown in Figure 4.8b confirmed the presence of the cyst. OCT B-scan image and histology from a LAP tissue construct without the presence of cysts is shown in Figure 4.8c and Figure 4.8d for comparison.

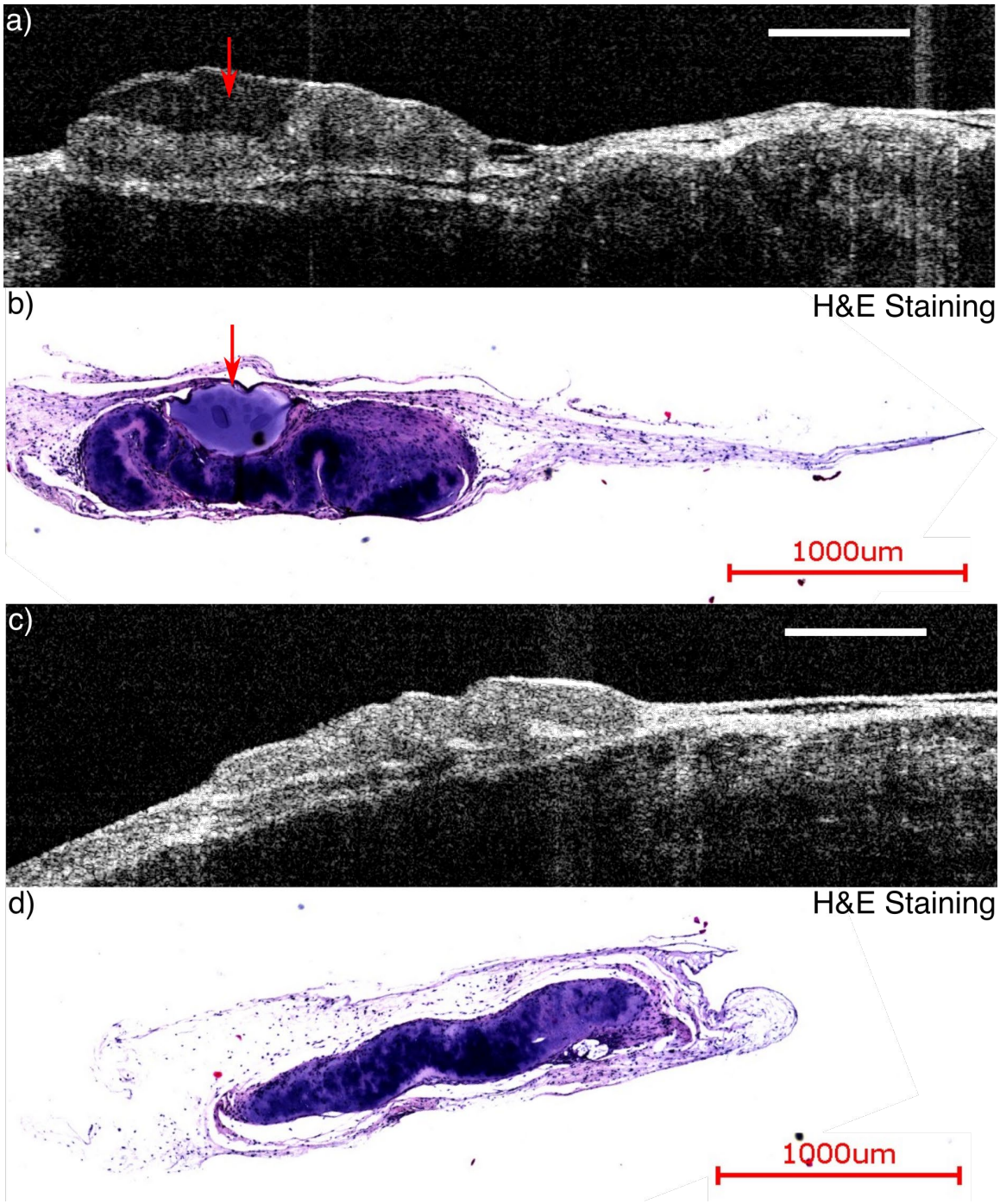

Figure 4.8 OCT image vs histology. a) OCT B-scan images of a CTL tissue construct with a cyst (red arrow, hypoechoic region) forming in its center. b) Histology (H&E) of the tissue construct in a) confirming the existence of cyst. c) OCT B-scan image of a LAP

tissue construct without cyst. d) Histology (H&E) of the tissue construct shown in c). Scale bar = 1 mm.

4.4 Discussion

The current study is the first (to the best of our knowledge) attempt at monitoring the maturation of engineered cartilage using multimodal FLIm-OCT during both *in vitro* and *in vivo* culture in a pre-clinical animal model. The results of the current study demonstrated the applicability of a non-destructive imaging system, combining FLIm and OCT, for spatial and temporal monitoring of the biochemical and structural characteristics of the tissue engineered cartilage. The two tissue characterization techniques (FLIm and OCT) utilized here successfully detected changes of ECM content during the maturation of self-assembled neo-cartilage during *in vitro* culture and *in vivo* maturation in a subcutaneous animal model. This multimodal imaging system holds great potential as a quality control method to provide full characterization of tissue engineered neo-cartilage before its release for clinical use, thus reducing the expense of biomanufacturing significantly and facilitating the translation of engineered cartilage product into clinical use.

The self-assembling process is a novel approach that allows engineering of articular cartilage constructs without the use of exogenous scaffolds [12]. Successful growth of self-assembled cartilage was associated with a significant increase in construct collagen and GAGs content, thereby providing a target for optical detection. Transforming growth factor beta (TGF-β) has become one of the most-used mediators for cartilage tissue engineering [154-156] due to its ability to promote chondrogenesis and strongly improve the synthesis of an array of cartilaginous structural matrix proteins, including proteoglycans and collagen (type-II)[46, 157-159]. TGF-β is often exogenously supplemented in culture media in its active form under the assumption that it will diffuse into constructs uniformly and improve the biosynthesis throughout the tissue. However,

recent studies have shown that at the later stages of tissue development, due to the presence of nonspecific binding sites in the ECM of articular cartilage, active TGF-β accumulates exclusively in the construct periphery leading to highly heterogeneous construct growth [152]. In the present study, the heterogeneous tissue growth due to nonuniform distribution of TGF-β is observed *in vitro* in both groups at both imaging time points. The outer edge of the tissue construct exhibited high fluorescence lifetime and intensity ratio in channel 1 (375-410 nm) and channel 2 (450-485 nm) as shown in Figure 4.2, indicating an increase in ECM collagen content. The fluorescence lifetime in channel 3 (CH3 = 532-565 nm) and channel 4 (595-660 nm) are relatively homogenous which is not surprising as channel 3 and channel 4 are outside the collagen emission spectrum and mostly sensitive to fluorescence signals from cells. This result demonstrated the potential of FLIm as a tool for nondestructively monitoring construct homogeneity during culture which is critical for creating clinically-relevant-sized constructs for joint repair.

Pixel-wise multivariant analysis of the FLIm data revealed strong correlation between all fluorescence lifetimes from all channels as shown in Figure 4.3, with the strongest correlation between channel 1 and channel 2 lifetime. This is expected as the major biological fluorophores in cartilage tissue construct, namely collagens, GAGs, and chondrocytes all have broad emission spectra. Collagen has a high quantum yield and fluorescence predominantly in channel 1 and channel 2 while cell fluorescence is present in all spectral channels [85]. GAGs have a similar emission spectrum as collagen but has low quantum yield. The high correlation between channel 1 and channel 2 can be explained by the high quantum yield of collagen which will cause collagen fluorescence to dominate the signal collected in channel 1 and channel 2 giving rise to a high correlation coefficient. The high correlation between fluorescence intensity ratio between channel 3 and channel 4 and lack of correlation between channel 3 and channel 4 lifetime with all intensity

ratios indicate that fluorescence from a single fluorophore is detected in channel 3 and channel 4. For engineered cartilage, this fluorophore is likely FAD inside chondrocytes. FAD has a broad emission from 500 nm to 650 nm matching the collection spectrum of channel 3 and channel 4. In addition, channel 3 fluorescence lifetime value of 2.70 ns agrees with the lifetime of FAD reported in the literature. Based on this result, we identified the parameters that are most useful for identifying the change of construct biochemical component: FLIm channel 1 parameters can provide information about collagen content in construct ECM while FLIm channel 3 parameters can be used to infer metabolic states of chondrocytes in the tissue constructs.

The development of a biochemical homogeneity index based on *en-face* FLIm parameters provides a single value to compare sample biochemical homogeneity among groups and across timepoints. The biochemical homogeneity index provides a new method for quantifying the heterogenous growth of the construct, currently missing in destructive testing methods. Significant increase of the homogeneity index is observed between t = 2 weeks and t = 4 weeks, indicating tissue maturation. A ring-shaped ROI is chosen for this study to account for the circular symmetry of the tissue sample but to exclude the defect (void) at the center of the construct. The defect at the center of the construct is a structural feature and can be quantified more accurately using 3D OCT volume data and therefore OCT was excluded from the biochemical homogeneity index calculation.

Defects (voids) with varying size, which are not identifiable by naked eye due to the transparent color of cartilage construct, are detected by FLIm and OCT independently in all tissue construct *in vitro* as shown in Figure 4.2 and Figure 4.6., The morphology of the tissue construct visualized by FLIm and OCT are very similar as shown in Figure 4.6 c-e. However, the spatial distribution of collagen in ECM shown in FLIm channel 1 is not visible in OCT data. This result

demonstrates the complimentary nature of FLIm and OCT techniques and the combination of both can yield a rapid and more complete characterization of tissue construct. The reason for the defect is unknown at this moment, more studies are needed to identify the reason of its formation.

FLIm-OCT assessment of the tissue construct in the pre-clinical animal model demonstrates that FLIm-OCT can be used to visualize the morphology and structure of the tissue construct *in situ* as shown in Figure 4.7. The formation of a cyst in tissue construct is detected by OCT and confirmed with histology (Figure 4.8). The size difference of the tissue construct between OCT and histology can be attributed to the error in histology sectioning and tissue shrinking during histology processing. The advantage of *in situ* OCT imaging is that it can provide real-time cross-section imaging with resolution close to that of histology at any location nondestructively at multiple time points. Histology analysis only allows the visualization of the tissue structure at discrete points and precludes the possibility of evaluating the entire clinical sample prior to implantation due to its destructive nature.

Compared to ultrasound (US), which has been used previously for characterization of engineered tissue constructs [44], OCT provides a higher resolution image with faster speed at the expense of penetration depth. For engineered cartilage, which is small in size and highly transparent, OCT is preferable compared to US. But we acknowledge that for larger tissue samples, US might be a better modality than OCT. In addition, FLIm and OCT are both optical modalities making the optical integration easy. A double clad fiber probe with diameter less than 400 μm can be easily utilized to deliver the 355 nm excitation of FLIm and the 1310 nm lighter of OCT to tissue sample as demonstrated previously [115]. The small form factor of the fiber optical probe makes FLIm-OCT the ideal modalities for applications like cardiovascular imaging.

4.5 Conclusion

This investigation demonstrates that the multimodal FLIm-OCT technique can be used to nondestructively monitor the heterogenous growth of engineered tissue construct during its maturation. The combination of FLIm and OCT offers a novel method for spatial and temporal monitoring of the maturation of engineered tissue construct by probing its chemical composition and structural properties in a nondestructive and noninvasive manner. This approach has a profound benefit in clinical research and large-scale manufacturing of tissue-engineered medical product where conventional quality control methods are destructive, sacrificing a large amount of tissue construct and incurring a large additional cost. Successful adoption of this method would accelerate the clinical translation of tissue engineered medical product from bench top to bedside.

Chapter 5 Multispectral fluorescence lifetime imaging device with silicon avalanche photo-detectors

The content of this chapter was previously published in *Optics Express.* Reprinted with permission from [160] © The Optical Society.

This chapter reports the design, development, and characterization of a novel multi-spectral fluorescence lifetime measurement device incorporating solid-state detectors and automated gain control. For every excitation pulse (~1 μJ, 600 ps), this device records complete fluorescence decay from multiple spectral channels simultaneously within microseconds, using a dedicated UV-enhanced avalanche photodetector and analog-to-digital convert (2.5 GS/s) in each channel. Fast (<2 ms) channel-wise dynamic range adjustment maximizes the signal-to-noise ratio. Fluorophores with known lifetime ranging from 0.5 - 6.0 ns were used to demonstrate the device accuracy. Current results show the clear benefits of this device compared to existing devices employing microchannel-plate photomultiplier tubes. This is demonstrated by 5-fold reduction of lifetime measurement variability in identical conditions, independent gain adjustment in each spectral band, and 4-times faster imaging speed. The use of solid-state detectors will also facilitate future improved performance and miniaturization of the instrument.

5.1 Introduction

Various label-free fluorescence spectroscopy and imaging techniques have been identified as a promising means for quantitative and sensitive investigation of changes in the biochemical composition of tissue both *in vivo* and *in vitro*[29]. Spectrally-resolved lifetime measurements, in particular, are of interest as the tissue autofluorescence originates from numerous endogenous constituents (e.g. structural proteins, metabolic enzyme co-factors, porphyrins, lipids and

lipoproteins) with complex photo-physical properties and overlapping spectral emission [75]. Thus, lifetime measurements can improve the specificity of the fluorescence acquisition by resolving the decay dynamics of such fluorophores in multiple spectral bands [161]. Also, lifetime measurements are more robust when compared to spectral intensities. The latter are typically hampered by non-uniform tissue illumination, changes in fluorescence excitation-collection geometries, or presence of endogenous absorbers (e.g., blood) resulting in light intensity attenuation. Moreover, an instrument capable of measuring decay dynamics of tissue autofluorescence simultaneously in multiple spectral emission can generate a wealth of orthogonal parameters for a more complete assessment of tissue characteristics and underlying biochemical features as well as for superior tissue classification [76, 77].

The most common implementation of fluorescence lifetime measurement is time-correlated single photon counting (TCSPC), frequently used in microscopy. In TCSPC, the tissue sample is excited by a high repetition-rate laser and the fluorescence emission is detected by single photon photodetector(s) [36] including multichannel detectors such as multi-anode photomultipliers (PMT) [64, 65] or single photon avalanche diode (SPAD) arrays [66]. TCSPC is well suited for microscopy because the low pulse energy excitation beam can be tightly focused onto tissue sample without causing significant thermal damage. However, detection of individual photons necessitates that background light is kept to a minimum. This limits the TCSPC's potential in clinical settings, in which elimination of ambient room light is either impossible or creates a major disruption in clinical workflow. As a result, to date few clinically compatible TCSPC-based systems have been used in clinical applications. The more recent adoption of synchronous external illumination could address this shortcoming and facilitate a more effective implementation of TCSPC technique [66, 67] in clinics in the future.

An alternative approach is pulse sampling of fluorescence emission transients in which a large amount of fluorescence photons are generated by a short (sub-ns) and intense excitation pulse (~0.1-10 μJ) and detected by a high-bandwidth photodetector [34, 35]. The resulting electrical transient signal is captured with a fast digitizer with a resolution of tens of picoseconds allowing fast recording (~few microseconds) of fluorescence decays. The large number of fluorescence photons generated within a nanosecond means that background illumination is unlikely to adversely impact fluorescence signal. In addition, since analog detection is utilized, low frequency signals of ambient light can be filtered. This approach was found best suited for mesoscopic imaging (submillimeter resolution) of large areas (>10mm) due to the high energy excitation pulses (~0.1-10 μJ).

Successful implementation of the pulse sampling approach has employed both avalanche photodiodes (APD) and PMTs. Earlier non-spectral-resolved devices using APDs were successfully used for colorectal cancer diagnosis *in vivo* [162] demonstrating the clinical potential of pulse sampling scheme but the identification of specific biochemical species was limited by the inability of the system to spectrally resolve the fluorescence emission. Later spectrally-resolved devices utilizing a PMT and a monochromator [35] demonstrated the clinical application of multispectral pulse sampling in studies of atherosclerotic plaques and brain tumors *in vivo*. Furthermore, the pulse sampling technique has enabled the construction of an instrument capable of simultaneous measurements of fluorescence lifetimes in multiple spectral emission bands suitable for tissue characterization [71].

Our group has reported the first implementation of a practical point-scanning system consisting of a fiber optic probe, a single microchannel plate photomultiplier tube (MCP-PMT) detector, fast digitizer (12.5 GS/s) and temporal multiplexing scheme using different lengths of

fiber optic delay lines for each spectral band of the instrument [61]. This instrument was further refined by our laboratory enabling fast system dynamic range adjustment [79], real-time data processing and real-time augmentation of fluorescence parameters for intraoperative tissue diagnosis and surgical guidance [80]. It is currently being evaluated in clinical settings to assess various tissue pathologies including oropharyngeal cancer [81] and brain tumors [82]. Also, it has been used extensively in benchtop experiments to investigate features of atherosclerotic lesions [83] and osteoarthritis [116], to identify positive cancer margins in breast tissue specimens [84], and to answer fundamental biomedical questions in tissue engineering [85, 86]. The same time-multiplexing single PMT approach was adopted by others groups [87-89] and combined with galvanometer scanners for both *in vitro* and *in vivo* tissue diagnosis with a handheld endoscope[90] or scanning microscopy [87, 91]. A limitation of this temporal multiplexing scheme stems from the use of a single MCP-PMT detector. The short delay between the arrival time of each channel (~50 ns) prevents adjustment of bias voltages for each individual channel. The detector gain must therefore be reduced to avoid saturation of the higher intensity channel, thus negatively impacting the signal-to-noise ratio (SNR) of the remaining channels.

In this chapter, we report the design, development, and performance evaluation of a pulse sampling Fluorescence Lifetime Imaging (FLIm) device using a multi-APD scheme for simultaneous measurement of fluorescence lifetimes in multiple spectral channels addressing the limitations of existing configurations. In contrast to the earlier implementation using one MCP-PMT, the instrument reported here relies on dedicated solid-state silicon avalanche photodiodes (APDs) and gain modulation for each spectral channel. This configuration allows for optimization of detection sensitivity in each spectral channel. While here we demonstrated a 3-channel detection scheme, this approach can be easily extended to a higher channel count, as needed. This new

multispectral FLIm system is compact and suitable for tissue characterization and diagnosis in clinical environments.

5.2 Materials and methods

5.2.1. Overview of the device using APDs for simultaneous measurements of fluorescence lifetime in 3 spectral channels

The APD-based multispectral FLIm device design is illustrated in Figure 5.1. A pulsed 355 nm UV laser is used for fluorescence excitation (STV-02E-140, TEEM photonics, France). Excitation light is delivered to the sample by a fiber optic probe connected to the fiber probe port. The fiber probe consists of one multimode optical fiber (365 μm core diameter, 0.22 NA, FG365UEC, Thorlabs, USA). Fluorescence signal from the sample is collected using the same fiber probe, spectrally resolved by a set of dichroic mirrors and bandpass filters and directed to three variable-gain, UV-enhanced Si APD module with integrated transimpedance amplifier. The device also includes a 440 nm laser (TECBL-50G-440-USB-TTL, Worldstartech, Canada) that serves as an aiming beam enabling real-time visualization of the location from where the fluorescence (point-measurement) is collected [163]. The entire optical system (except digitizer and computer) fits within a dimension of 25 cm x 21 cm. Two 2 channel digitizers with 1.5 GHz bandwidth and 2.5 GS/s per channel (NI PXIe-5162 digitizer National Instruments, Austin, Texas) were used for signal recording (not shown).

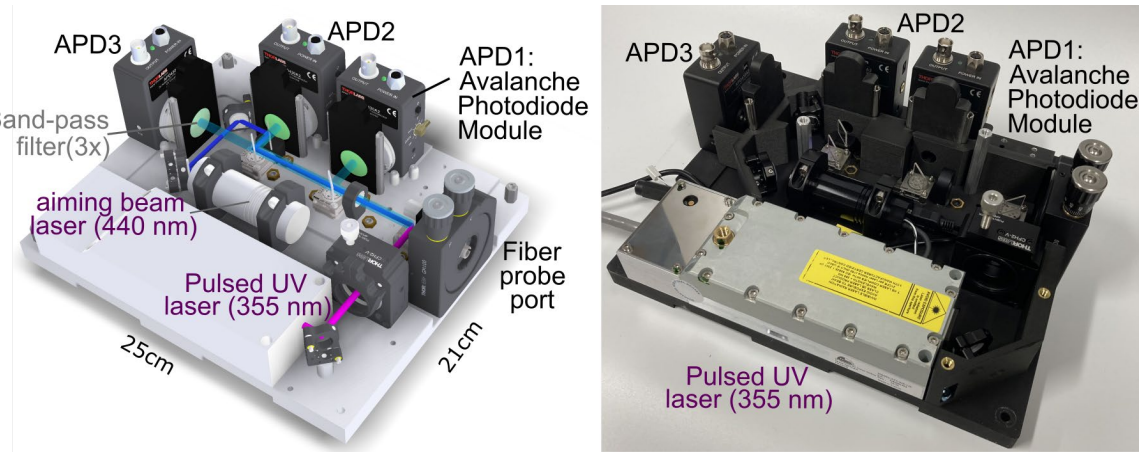

Figure 5.1 Schematic diagram and photograph of the 3 channel APD-based fluorescence lifetime device.

5.2.2. APD module

The variable-gain, UV-enhanced Si APD detector module was adapted from a commercially-available module (APD430A2-SP1, Thorlabs, NJ) and consists of three main parts: 1) the APD detector 2) the post-detection amplifier circuit with fixed trans-impedance gain. 3) the analog control circuit adjusting the bias voltage of the APD detector, and hence the overall gain of the APD module. Table 1 lists the APD module characteristics. Figure 2a depicts a typical responsivity curve. The multiplication factor was measured for each APD modules (Figure 5.2b).

Table 5-1 APD Module Specifications

Detector Type	UV Enhanced Silicon APD
Wavelength Range	200 - 1000 nm
Output Bandwidth (3 dB)	DC-400MHz
Active Area Diameter	0.2 mm
M Factor Adjustment Range	1 - 100 (Continuous)
Transimpedance Gain	5 kV/A (50 Ω Termination)
Max Conversion Gain	5.0×10^5 V/W

The bias control circuit modulates the reverse bias voltage at the APD detector based on an input control voltage. The accuracy, stability and response speed of the bias control circuit directly determine the performance of the imaging system. As a result, the integrated bias control circuit was designed based on the following characteristics: (1) The full gain (M=1-100) range of the APD module, corresponding to a maximum reverse bias voltage of approximately 150 V at the APD detector was controlled by a 0-4.6 V input voltage. (2) The relationship between reverse bias (control voltage) and APD module gain was nonlinear (Figure 5.2b), with unwanted variations of bias voltage leading to higher gain changes near the breakdown voltage (Figure 5.2c). The bias voltage stability at 150 V should be such that a gain variation no greater than 2% is observed. (3) The speed of gain adjustment of the APD module determines the ability to accommodate rapid changes in fluorescence intensity. Thus, the bias control circuit was designed to have a transit time of less than 2 ms which enables gain modulation at the laser repetition rate (< 500 Hz).

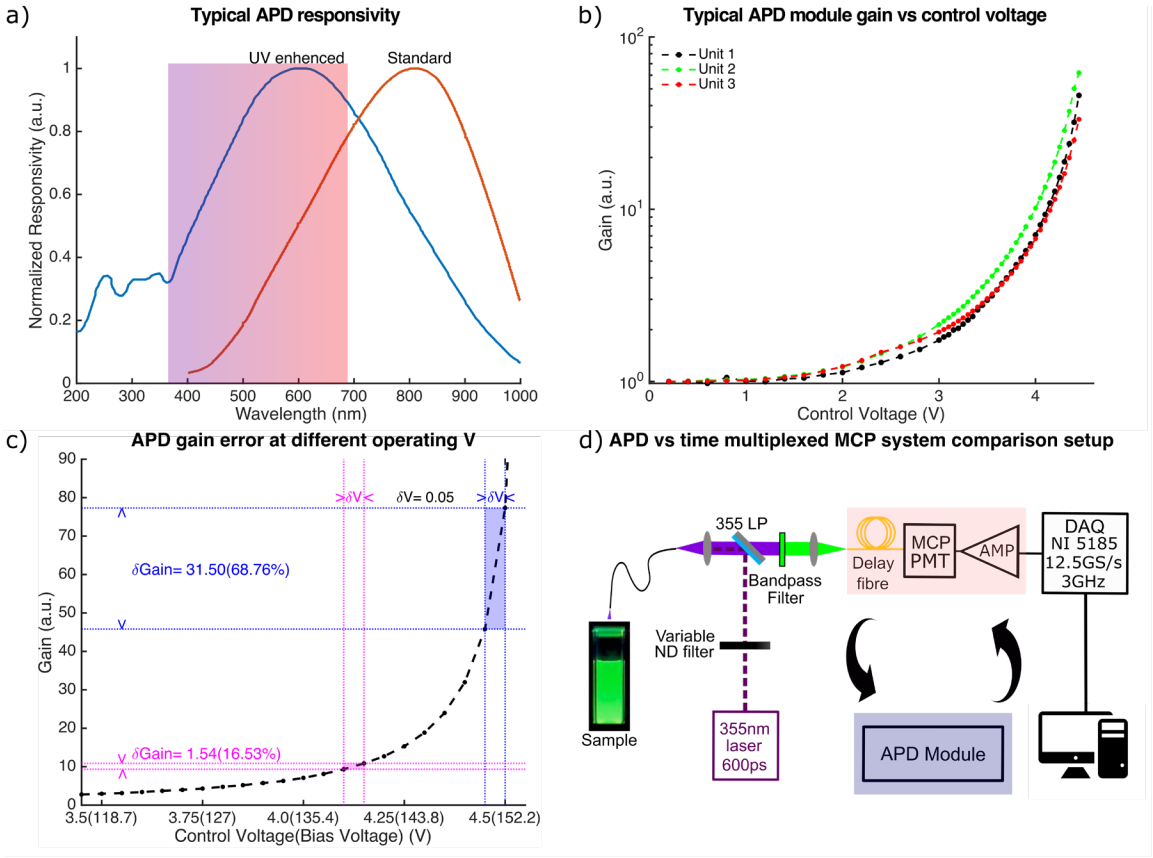

Figure 5.2 a) Spectral response of UV-enhanced APD and non-UV-enhanced APD module. Shaded rainbow area represents the typical emission spectrum range of biological tissue excited by 355nm laser. Adapted with permission from Thorlabs. b) Typical gain (multiplication factor) curve of the 3 APD modules. Unit-to-unit variation of the gain is observed. c) Due to APD modules' nonlinear behavior, same error in bias voltage leads to drastic different error of gain at different operating voltage. d) Schematics of the multi-APDs device vs. time multiplexing MCP device used in the SNR comparison experiment.

5.2.3. Optical throughput evaluation

To evaluate the ability to couple light from the fiber probe (365 µm core) onto the APD detector sensitive area (200 µm diameter), a lens (A397TM-A, f=11 mm, NA=0.3, Thorlabs, NJ) was used to collimate the light emerging from a 365 µm-core fiber and then a second lens (C610TME-A,

f=4.00 mm, NA=0.60; Thorlabs) was used to focus the light through a 200 μm size pinhole. The latter is representative of the APD aperture. The transmission efficiency was derived from optical power measurements before and after the pinhole (PM100D, Thorlabs, S120VC, 200 – 1100 nm, 50 mW).

5.2.4. Linearity characterization

To evaluate the linearity of the detection system and its effect on the fluorescence lifetime values, measurements were performed for different levels of excitation intensity and detector gain. These include measurement of Coumarin 120 (Exciton Coumarin 440) by varying the excitation intensity while keeping APD gain constant (M =75) and obtained signals with amplitudes from 0.2 V to 1.4 V in a step of 0.1V and measurements for different levels of APD gain while keeping the excitation intensity constant and obtained signals with the same amplitude range (0.2 V– 1.4 V). In addition, we tested various combinations of excitation intensity and APD gain such that a fixed peak signal (1 V) was maintained. In all configurations, 1000 waveforms were recorded at 2.5 GS/s. The instrument response function (iRF) was measured experimentally as stated in Section 2.8 for each APD gain level and used for lifetime deconvolution at corresponding APD gain level.

5.2.5. Performance characterization with fluorescent dyes and biomolecules

To determine the device lifetime measurement accuracy and precision, measurements were performed in solutions of organic dyes (100 μM concentration) with well-known fluorescence lifetimes and emission spectra: Coumarin 120 (Exciton Coumarin 440) in ethanol, Rhodamine 6G (Sigma, R4127) in water and Rose Bengal B (Sigma Aldrich CAS 11121-48-5) in ethanol. Their fluorescence emission was recorded in the 390/40 nm, 470/28 nm and 542/50 nm spectral band, respectively. Three main endogenous tissue fluorophores, i.e., the structure proteins collagen and elastin, and the enzyme cofactor NADH were used to determine the device's ability to analyze

more complex fluorescence dynamics of these biomolecules. Waveforms were acquired from Type 1 collagen from bovine Achilles tendon (Sigma Aldrich CAS 9007-34-5, dry powder), elastin from bovine neck ligament (Sigma Aldrich CAS 9007-58-5, dry powder), and 250 μM NADH (Sigma Aldrich CAS 606-68-8) solution prepared in 100 mM Mops buffer at pH 7. For each measurement, 1000 waveforms were acquired at 2.5 GS/s.

5.2.6. Comparative FLIm device performance: APD vs MCP-PMT detection schemes

The ability of the multi-APDs FLIm device reported here to perform accurate fluorescence lifetime measurement of biological samples was assessed in comparison with the time multiplexing single PMT FLIm system previously reported. The single PMT FLIm system has been fully described in our group's earlier publications [86]. The dynamic range of this earlier device could be adjusted by varying the bias high voltage of the PMT detector to account for the rapid change of fluorescence intensity [79].

We performed measurements under identical experimental conditions on fluorescent dyes with both multi-APDs and single PMT devices. Based on knowledge derived from prior benchtop experiments [85] and clinical studies [80], we determined experimental conditions that replicate the amount of signal typically encountered in clinical and pre-clinical setting. For clinical applications such as imaging of the oral cavity epithelium, a 400 mV peak fluorescence signal value was typically obtained in channel 1 (390/40 nm) with an PMT bias voltage of 1900 V. For benchtop applications, such as monitoring of engineered construct recellularization, a 400 mV peak fluorescence signal was typically observed in channel 3 (542/50 nm) with a PMT bias voltage of 2200 V. A single-channel APD prototype was used in this experiment as shown in Figure 5.2d. During the experiment, laser power and excitation collection geometry were set to obtain the desired signal (400 mV peak) using the time-multiplexing single-PMT system at the pre-

determined high voltage bias. The delay fiber, the PMT, and the amplifier were then replaced by the APD module. A signal with 400 mV peak voltage (the same as time multiplexing single PMT system) was obtained by adjusting the control voltage of the APD module. For comparison between both devices, waveforms (n=1000) and iRF from both systems were acquired at 12.5 GS/s (NI PXIe-5185, National Instrument, Austin, Texas).

5.2.7. Gain control characterization

The detector gain as a function of control voltage was characterized for each of the three APD detector modules. Specifically, constant incident light was directed to the detector and the output was recorded while the control voltage was increased in steps from 0.05 V to 4.6 V (0.2V steps were used to control voltage from 0.05 V -3.0 V and 0.05 V steps from 3.0 V - 4.6V.

The response time of the gain control circuitry was evaluated by monitoring the change in signal intensity (area under the curve of the measured detector pulse) following a step change (3.7 V to 4.4 V) of control voltage corresponding to a ~5x gain variation.

5.2.8. Optical fiber fluorescence background removal

Background fluorescence from the optical fiber probe is typically present in the acquired spectroscopic/imaging data, an undesirable effect that can be a significant obstacle to the extraction of fluorescence lifetime from the acquired waveforms. A computational method based on the normalization (scaling) of the fiber probe background fluorescence signal was applied to remove the background signal from the acquired waveform prior to lifetime computation. An illustration of the background removal process is shown in Figure 5.3. Fluorescence background waveform is acquired by holding the fiber probe in air (pointing away from any object) and adjusting the detector gain such that a good background fluorescence SNR is achieved. The waveform is then normalized (scaled) based on the amount of fluorescence signal generated by the fiber probe which

is a constant during an imaging session. The amount of fiber probe fluorescence signal is computed as the area under the curve (AUC) of the waveforms in the region prior to tissue fluorescence signal arrival as indicated by the red doted lines. The background is then normalized (scaled) and subtracted from the data with the normalization (scaling) factor calculated as the ratio of the AUC of the raw and background waveform. As this method is based on the constant fluorescence signal generated by fiber probe fluorescence, no knowledge of the detector gain is required making it a fast and simple but robust method.

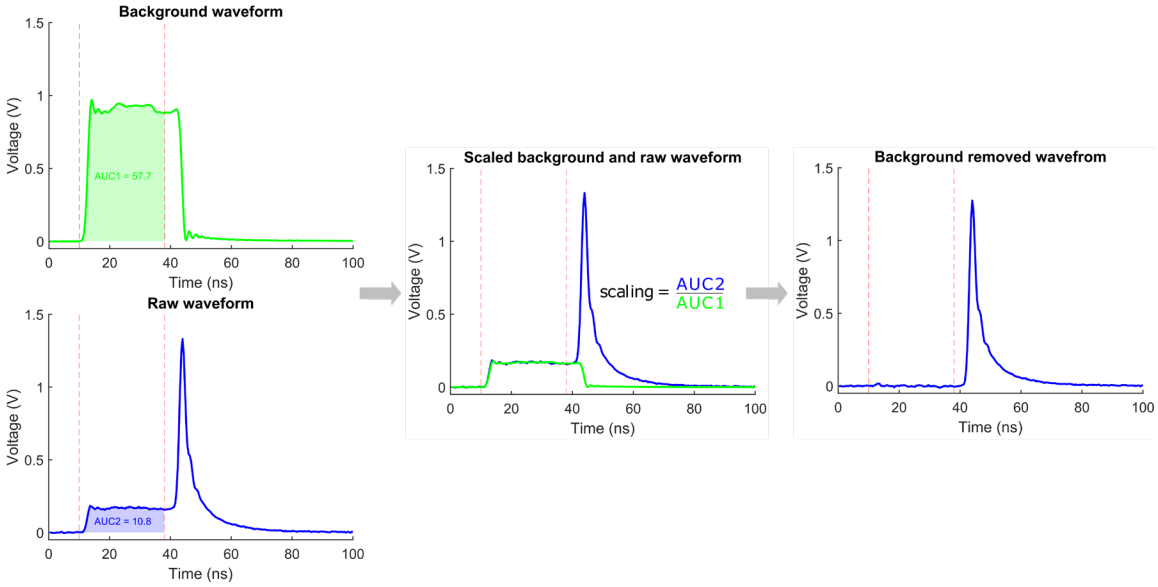

Figure 5.3 Fluorescence background removal process. The background waveform is normalized (scaled) based on the fluorescence signal generated from the optical fiber probe, which should remain constant during image acquisition, and subtracted from the acquired raw waveform. The normalization (scaling) factor is computed as the ratio of area under the curve (AUC) between the red doted lines of the raw waveform and background waveform. As the method is based on the constant signal of the fiber probe fluorescence, no knowledge of the detector gain is required making it a fast and simple but robust method.

5.2.9. Estimation of fluorescence lifetime values

Typically, three factors can lead to the broadening of the measured fluorescence emission waveform: 1) the duration of the excitation pulse, 2) the intermodal dispersion in the multimode optical fiber that results in broadening of the emitted light pulse, and 3) the response time of electronic components (detector and digitizer front end). To compensate for the fluorescence pulse distortion, the intrinsic fluorescence decay was recovered by numerical deconvolution of the instrument response function (iRF) from the measured fluorescence pulse transients.

The iRF in response to the 600 ps UV excitation pulse was measured using fluorescence pulses from two dye solutions. The 4-dimethylamino-4-cyanostilbene (DCS) (ChemBridge, San Diego, California) at 100 μM concentration in Cyclohexane was used to for 390/40 nm and 470/28 nm spectral channels. The hemicyanine dye 2-(p-dimethylaminosotyryl) pyridylmethyl iodide (2-DASPI) (Sigma-Aldrich, Cat. No. 280135) at 1 mM concentration in Ethanol was used for spectral channel of 542/50 nm. DCS dissolved in Cyclohexane has a very short (~66 ps) lifetime with fluorescence emission from 300nm - 500nm [36]. When dissolved in ethanol, 2-DASPI has a very short (~30 ps) average lifetime and a emission spectrum with a maximum at approximately 550 nm [164]. Unless otherwise stated, system iRF was acquired at 12.5 GS/s for PMT system and 5 GS/s for APD system.

For the APD-based device (except for data acquired for *Section 5.2.6 Comparative FLIm measurement of APD and MCP-PMT based devices*), the acquired fluorescence waveforms were first re-sampled to 5 GS/s equivalent by a lowpass interpolation algorithm 8.1 [165] prior to deconvolution to match the sampling rate of the system iRF. This was necessary because the deconvolution algorithm requires the iRF and fluorescence to have identical sampling rates. To compensate for laser jitter, after re-sampling the fluorescence waveforms from all measurements were temporally aligned using a constant fraction discriminator implemented in MATLAB

(MathWorks, Natick, Massachusetts). This approach compares favorably to signal timing determination based on maximum waveform amplitude, adversely impacted by noise and limits in sampling rate, or leading-edge discriminator, subject to time walk when applied to waveforms of varying amplitudes [166, 167]. An illustration of the data processing pipeline is shown in Figure 5.4.

Signal deconvolution was performed using a fast algorithm (<10 µs per decay) previously reported by our group [127]. The algorithm is based on a constrained least-squares deconvolution with Laguerre expansion (CLSD-LE) and has demonstrated robustness against noise.

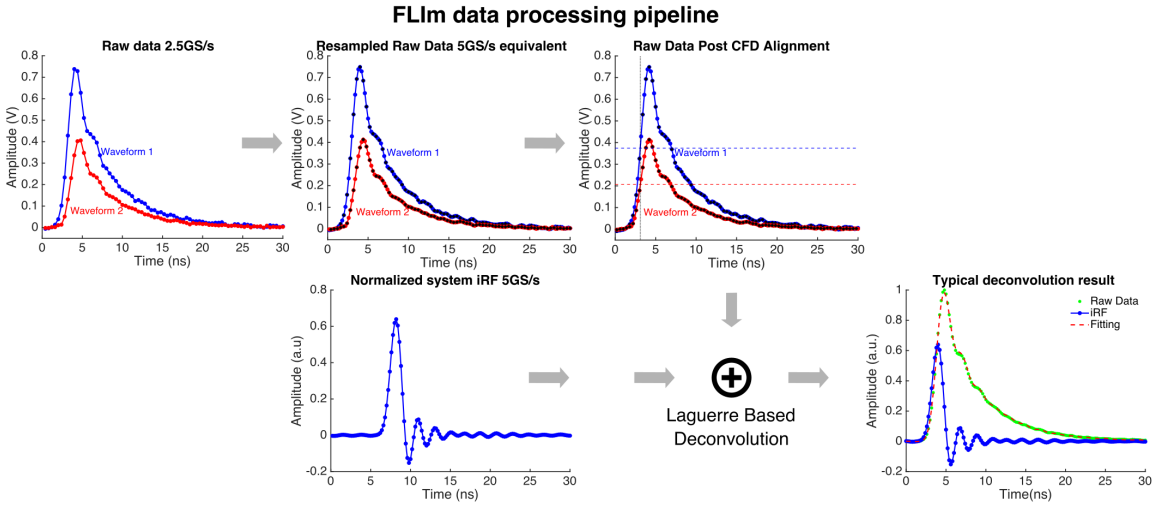

Figure 5.4 FLIm signal processing pipeline. The raw signal acquired at 2.5 GS/s is first re-sampled to equivalent of 5 GS/s by linear interpolation to match the sampling rate of system iRF. The signal is then deconvolved using a Laguerre expansion-based method to extract fluorescence lifetime and intensity. A fluorescence lifetime map can be generated for scanning application.

5.2.10. Validation on tissue sample

To validate the performance of the multi-APD-based device and its ability to generate FLIm images, data were recorded by freehand scanning (2341 point measurements, ~35 cm^2 sample area, 70-second scanning duration) of a tissue sample (lamb) which presents a variety of tissue types (e.g., bone, bone marrow, fat, muscle and connective tissue) that enable direct visualization of fluorescence contrast. FLIm images were reconstructed from point measurement by capturing a white light video of the specimen using an external camera (CM3-U3-13Y3C-CS, Point Gray, with Fujinon HF9HA-1B 2/3"9 mm lens) and extracting the measurement location for each frame (30 Hz) during the scanning procedure. FLIm measurement localization was achieved by a Convolutional Neural Network (CNN)-based aiming beam localization algorithm [163]. Linear interpolation was used to determine the FLIm measurement location between each available video frame when high (480 Hz) laser repetition rate was used due to the limitation of camera frame rate (30 Hz).

To demonstrate the improved performance of the novel simultaneous multispectral APD FLIm system, two configurations of the 355 nm excitation laser were used: 1) 1 μJ per pulse at output of fiber probe, low (120 Hz) laser repetition rate (excitation parameters similar to the time-multiplexing multispectral PMT FLIm system currently used for clinical studies); 2) 0.25 μJ per pulse at output of fiber probe, high (480 Hz) laser repetition rate. Under both configurations, the UV exposure to tissue sample was identical and in compliance with IEC 60825 standard [168]. Four-fold averaging of acquired fluorescence waveforms was performed for both configurations.

5.3 Results

5.3.1. Optical throughput

The measured coupling efficiency of light transmitted from 365 µm multimode fiber through the 200 µm pinhole was found to be 99%. This indicates a minimum effect of the small size of APD sensitive area on fluorescence photon collection efficiency.

5.3.2. System validation with fluorescent dyes and biomolecules

The computed lifetime values of the fluorescence dyes (Coumarin 120, Rhodamine 6G and Rose Bengal) and tissue fluorophores (collagen, elastin, and NADH) are listed in Table 5-2. These values were found to be in close agreement with those reported in the literature. Oscillation present in the tail of fluorescence waveforms and system iRF (Figure 5.4) did not pose any issue in the recovery of fluorescence lifetime values.

Table 5-2 Lifetime measurement and literature values for fluorescence dyes and tissue fluorophores used for system validation

		Measured		Literature
Fluorophore	Wavelength band (nm)	Lifetime (ns)	Error (ns)	Lifetime (ns)
Rose Bengal in ethanol	390/40	0.834	0.080	0.850[36]
Coumarin 120 in ethanol	470/28	3.60	0.034	3.64[169]
Rhodamine 6G in H_2O	542/50	3.97	0.080	4.08[170]
Collagen	390/40	5.621	0.093	1.42-5.30[171]
NADH	470/28	0.472	0.039	0.30-0.50[36]
Elastin	470/28	6.124	0.097	5.20-7.36[172]

5.3.3. APD module temporal response dependency on APD gain and signal amplitude

Changes in measured fluorescence pulse waveforms (e.g., C120 dye) as a function of APD gain and excitation intensities are shown in Figure 5.5a and Figure 5.5b, respectively. The normalized waveforms to peak intensity indicate that a decreased gain leads to a nonlinear behavior (Figure 5.5c), with most noticeable oscillations observed at the low gain (M=3). While the tail of the

fluorescence pulse as well as the measured iRF shows noticeable oscillation, the numerical deconvolution algorithm accounts for this behavior as seen in Figure 5.4.

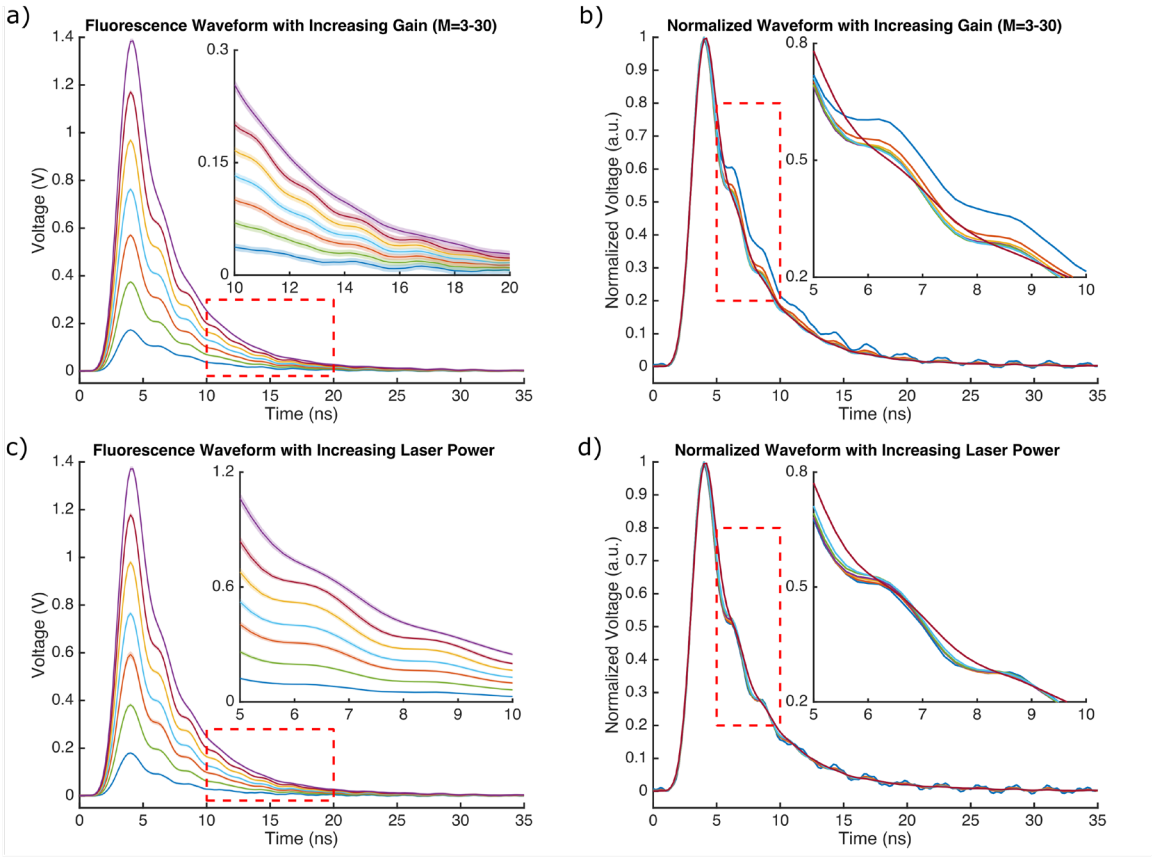

Figure 5.5 Investigation of measured fluorescence waveforms as a function of signal amplitude and APD gain, characterized using 1000 measurements of Coumarin 120 solution. a) Mean and standard deviation of fluorescence waveforms at different APD gain. b) Display of normalized averaged waveforms highlights some difference of temporal response that may affect estimated lifetime. c) Mean and standard deviation of fluorescence waveforms at different optical signal intensity (obtained by varying the laser pulse energy). d) Display of normalized waveforms highlights some difference in temporal response.

The impact of APD gain and signal amplitude on the APD module temporal response (Figure 5.5) may influence the ability to accurately estimate fluorescence lifetimes. This effect was

systematically evaluated by reporting the distribution of computed lifetimes after deconvolution in each configuration (Figure 5.6). Deconvolution was performed using a single iRF as well as using an iRF for each individual gain value (matching iRF, see Figure 5.6b-c). As seen in Figure 5.6a, variations of optical signal amplitude have minimum effect on average estimated lifetimes, in good agreement with literature values of 3.64-3.85 ns[169], although as expected, lower signal amplitude leads to higher lifetime standard deviation. Measurements at low gain led to an overestimation of lifetime (Figure 5.6b-c). This issue was addressed by using different iRFs for each gain value. We observed that compensating decrease of optical signal intensity by an increase in APD gain led to accurate lifetime estimations provided that different iRFs were used for each gain (Figure 5.6c). Interestingly, this did not lead to any increase in estimated lifetime standard deviation.

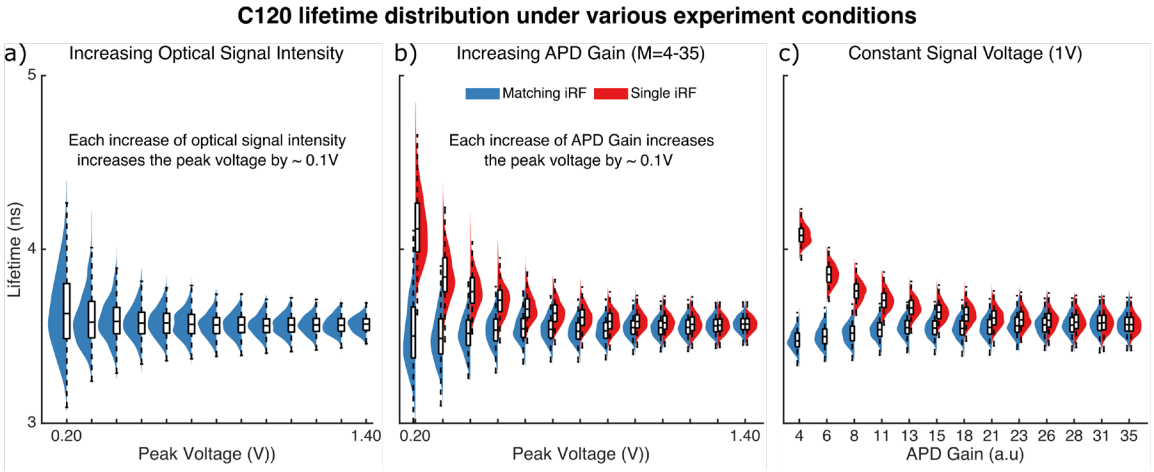

Figure 5.6 Distribution of Coumarin 120 fluorescence lifetime under (a) increasing optical signal intensity. (b) increasing APD gain. (c) constant signal peak voltage (1V) where each increase of APD gain is compensated by a decrease of optical signal intensity to maintain a constant 1V peak voltage.

5.3.4. APD System SNR evaluation

The recovered fluorescence lifetime of the APD system (3.573 ± 0.061 ns) was found in good agreement with that of the MCP-PMT system (3.66 ± 0.291 ns). However, higher SNR was obtained with the APD-based system (Figure 5.7a) compared to MCP-PMT system (Figure 5.7b), resulting in 5-fold lower standard deviation of measured fluorescence lifetime.

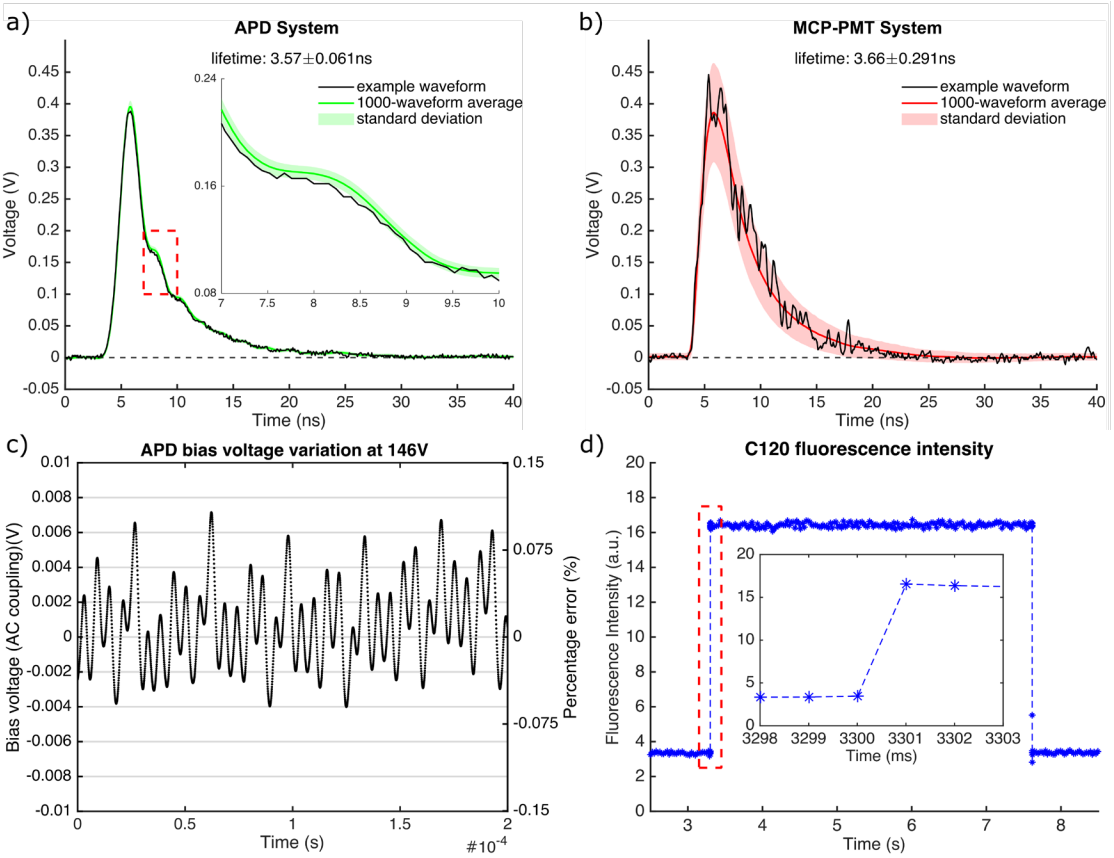

Figure 5.7 Back-to-back SNR comparison of muti-APDs FLIm device (a) and time multiplexing single PMT FLIm device (b). Mean fluorescence waveform, one raw waveform and standard deviation (shaded area) were shown. c) Variation of APD bias voltage @146V. Adapted with permission from Thorlabs. d) Response of the APD-based detection to a step change of bias voltage. The response time is less than 2 ms. No overshoot was detectable at either rising or falling edge. The time resolution of the measurement was 1 ms.

5.3.5. Characterization of gain control circuit speed and stability

The accuracy of the detector gain is determined by the stability of the bias voltage. The slope of the gain-bias curve is steepest close to the breakdown voltage (Figure 5.1b), thus variations of gain due to fluctuation of bias voltage will be highest near the breakdown voltage. We confirmed that the fluctuations of bias voltage were less 0.007 V (Figure 5.7c), which corresponds to a maximum gain fluctuation of 0.2 % at 146 V bias voltage. The overall APD FLIm response speed to a step change of control voltage (5-fold change in APD gain) was less than 2 ms (Figure 5.7d). No overshoot was observed at either rising or falling edge.

5.3.6. Validation on tissue sample

Figure 5.8 displays the FLIm parametric map obtained from freehand scanning of the lamb tissue. Areas of bone, bone marrow, fat and muscle are highlighted in the white light image of the tissue sample (Figure 5.8a). The FLIm point-measurement locations are shown in Figure 5.8b and Figure 5.8c for low (120 Hz) and high (480 Hz) laser repetition rate respectfully. As expected, better FLIm coverage of the tissue sample is achieved with high (480 Hz) laser repetition rate. The augmented FLIm maps from spectral band 470/28 nm for both low (120 Hz) and high (480 Hz) laser repetition rate are shown in Figure 5.8d and Figure 5.8e. Current results show that distinct tissue types (e.g. bone marrow, bone, fat, muscle) are associated with distinct fluorescence lifetimes and clearly distinguishable from the FLIm map. Lifetime values from different tissue types are consistent across FLIm maps of low and high laser repetition rate, indicating good lifetime recovery even with reduced pulse energy. However, a more complete and smoother FLIm map is achieved with higher laser repetition rate despite the reduction in pulse energy.

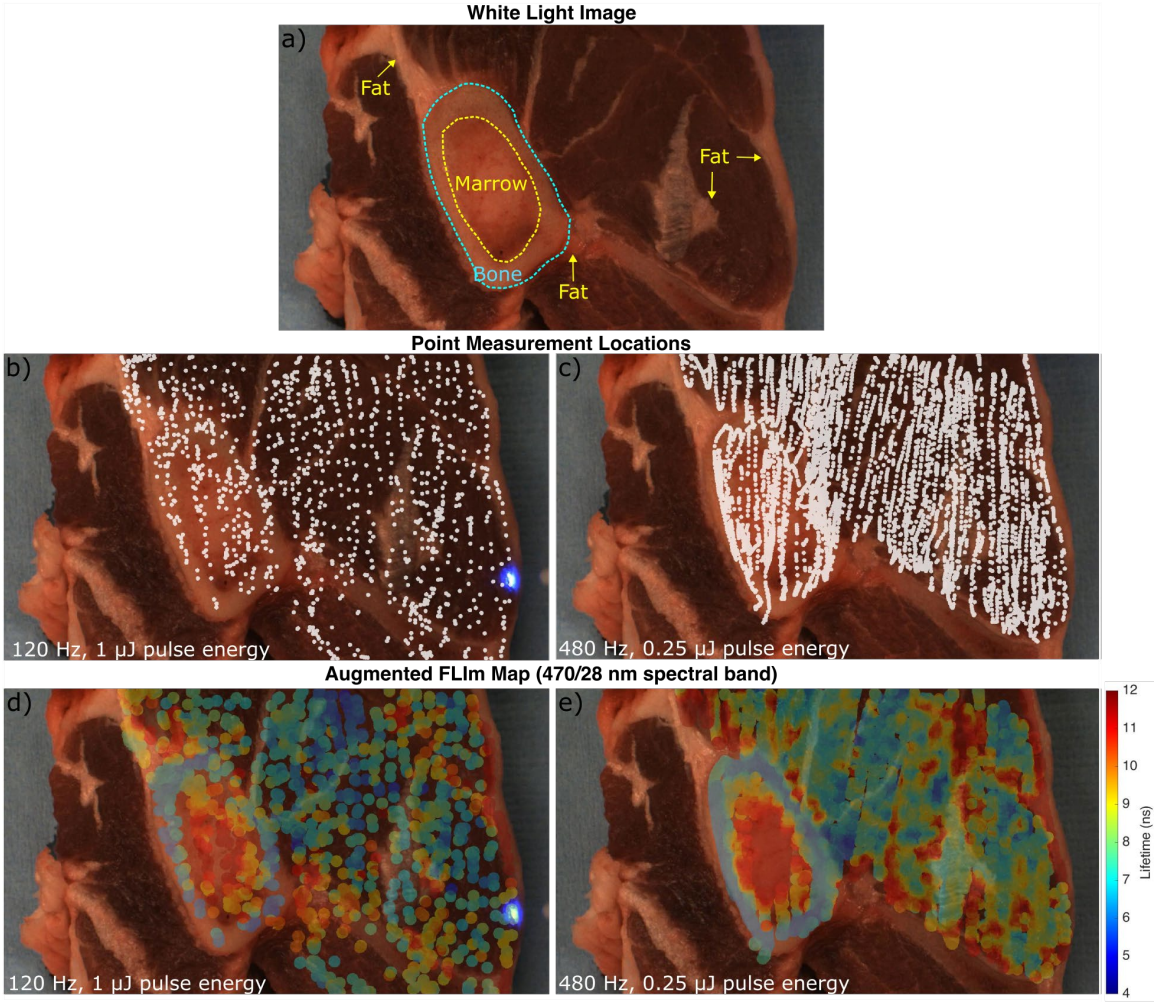

Figure 5.8 Representative FLIm images obtained via the freehand scanning of *ex vivo* fresh lamb tissue. a) white light image of lamb tissue sample. b) and c) FLIm points measurement locations for different 355nm laser configurations. d) and e) white light images of the lamb tissue augmented with lifetime maps from 470/28 nm spectral band under different 355 nm laser repetition rate.

5.4 Discussion

This study demonstrates the performance of an APD-based FLIm device enabling measurements of fluorophores with a broad range of fluorescence lifetimes (0.5 – 6.0 ns) simultaneously in multiple-emission spectral bands. The instrument is capable of rapid adjustments (< 2 ms) of the

detection gain independently for each APD detector resulting in maximization of SNR in each spectral channel. Rapid gain adjustment is critical to account for the potential rapid change of fluorescence intensity encountered in clinical setting due to change in probe-to-tissue distance during scanning, differences in quantum efficiencies of endogenous fluorescent molecules and presence of residual blood or other fluids. Moreover, the results show a significant improvement of the signal quality (higher SNR and lower lifetime variability) and imaging speed of the multi-APDs when compared to the previously reported time-multiplexing single PMT device.

The ability to recover accurate lifetimes independently from signal intensity levels, detector gain and detector output voltage is of critical importance for fluorescence lifetime measurements. Current results demonstrate that accurate and consistent lifetime values (1% variability of mean lifetime) can be achieved with the multi-APDs FLIm device across a wide range of signal intensity levels (Figure 5.6). We observed a broadening of the instrument's IRF at low detector gain and subsequently large lifetime estimation error when a single iRF is used for deconvolution (Figure 5.6b). Such behavior is expected given the dependance of the terminal capacitance of the APD detector from the detector's gain (reverse bias) [173]. We found that this effect can be addressed by deconvolving the measured signal with an iRF acquired at similar APD gain that resulted in a lifetime accuracy of 1% over the M=8-35 detector gain range (Figure 5.6b). The small (<0.1 ns) residual error observed at low APD gain (M=4) will be further investigated. For applications where small variations of lifetime are expected, highest accuracy can be achieved by ensuring a gain of no less than 8.

Current results also demonstrate the ability of the prototype multi-APDs FLIm device to accurately resolve fluorescence lifetimes ranging from as short as 0.5 ns to 6.0 ns. This demonstrates that the reduced bandwidth of the APD (400 MHz) compared to the MCP-PMT (1.5

GHz) does not prevent the accurate measurement of fluorophores with a broad range of lifetimes. Comparison of accuracy and precision of lifetime measurement in identical conditions between time-multiplexing single-PMT FLIm and multi-APDs FLIm demonstrates a 5-fold reduction of lifetime measurement variability in identical conditions. This improvement is particularly relevant for clinical data acquisition, where point measurement rate is currently limited by the maximum permissible exposure of tissue [168]. For example, we demonstrated that FLIm measurements performed in a clinical setting at a rate of 30 Hz (1.0 μJ pulse, 120 Hz laser repetition rate, 4-fold average) with the reference MCP system, could be performed as accurately with the proposed system at 480 Hz (0.25 μJ pulse, 480 Hz laser repetition rate, 4 averaging), leading to either a much faster or more complete coverage of the surgical field (Figure 5.8). Alternatively, improvements in FLIm detection could be used to better identify small changes in fluorescence lifetime, improving system sensitivity when small lifetime changes are expected such as recellularization of engineered tissue [85]. For applications where measurement speed is not critical, as for some benchtop applications, the proposed system will enable higher resolution imaging by sampling the tissue more densely while reducing data averaging.

FLIm measurements performed with the multi-APD device reported here will also benefit from the ability to adjust the gain of each individual channel independently. This addresses a limitation of the MCP-PMT-based system where the same detector gain is applied across all channels. As a result, the dynamic range of the MCP-PMT system is determined by the channel with the most signal, thus negatively impacting the SNR of the remaining channels. The APD FLIm system with individual channel gain adjustment capability will improve signal quality for tissue where fluorophores with distinct quantum yield are present in different spectral channels.

Moreover, the small size, low cost and robustness of APD detectors is a clear advantage over MCP-PMT. Independent detectors for each spectral band means that delay fibers are no longer necessary, thus reducing the complexity and cost of the system. In addition, the advance of Si manufacturing technology and integrated circuit design may enable, in the near future, the integration of a microchip laser, multiple APD detectors, their bias control and amplifier circuits as well as a compact multichannel ADC into one integrated circuit board, enabling the fabrication of miniaturized handheld FLIm systems for clinical use.

The APD-based pulse-sampling FLIm reported here is well suited for use in clinical settings and compares favorably to most recent developments in TCSPC-based systems. First, it operates under room light with no special accommodation in the operating room lighting conditions, thus making the adoption of the technology straightforward. While TCSPC-based systems utilizing synchronous external illumination were recently reported [66, 67], implementation in surgical settings would require all light sources to be replaced with sources synchronized with the TCSPC system. Second, the proposed simultaneous multispectral multi-APDs FLIm system can achieve a point measurement rate of 480 Hz, faster than the recently reported data acquisition rate of 50 Hz for the TCSPC-based system. This limited acquisition speed stems from the low photon collection efficiency of the reported TCSPC based system due to: the low filling factor (~3%) of the SPAD array, the intrinsic inefficiency of time-gated strategy and the high loss of dispersing optical components. Although these issues could be addressed with additional development, the device reported here provides key benefits to support clinical validation studies of FLIm technology.

5.5 Conclusion

We have demonstrated the first APD-based multispectral FLIm system with individual channel gain adjustment capability. Accurate and precise lifetime measurement was achieved across a 10-fold change of excitation intensity and APD gain. In comparison with previously reported multispectral pulse-sampling FLIm systems that rely on temporal multiplexing and a single MCP-PMT, the current design improves the system SNR and allows fast independent dynamic gain adjustment for each optical channel making it better suited for clinical use. Compared to an earlier-reported APD-based FLIm system [34], the current system offers better responsivity in visible wavelengths, multichannel detection for different tissue fluorophores and dynamic gain adjustment capability. The use of low-cost solid-state detectors will facilitate optical and electrical integration and miniaturization, leading to more compact and low-cost fluorescence lifetime imaging instrumentation. In addition, the validation plan we developed will serve as a reference for the design, validation, and standardization of future FLIm devices.

Chapter 6 Conclusion

Osteoarthritis is a prevalent and disabling disease affecting the quality of life of millions of people worldwide. The solution to this age-long and vexing problem resides not only in the early detection of the disease but also in the successful adaptation of the tissue engineering approach into the daily clinical care. The lack of an effective, clinical compatible technique for early diagnosis of OA and a nondestructive quality control tool for large scale manufacturing of engineered cartilage product motived this work.

Chapter 3 of this dissertation explored the potential of fluorescence lifetime imaging for early detection of OA by understanding the fluorescence properties of native cartilage tissue, as well as the relationship between enzymatic treatment induced biochemical changes in cartilage ECM and the measured optical parameters. The best parameter for detecting the loss of GAG in cartilage tissue was identified, providing a key parameter for quantitative characterization of cartilage ECM biochemical composition. Current results represented a powerful validation of FLIm measurements of distribution of biochemical components in cartilage tissue and showed that it can be used as a valuable tool for early diagnosis of OA.

Chapter 4 of this dissertation demonstrated the potential of using a bimodal system combining fluorescence lifetime imaging and optical coherence tomography for nondestructive monitoring of the heterogenous growth of tissue engineered cartilage in a pre-clinical animal model. Spatial and temporal variation of ECM components of tissue construct were detected by FLIm. Defects (voids) at the center of the tissue constructs during *in vitro* culture were detected by both FLIm and OCT. Cyst formation during *in vivo* culture was detected by OCT and confirmed with histology. This result showed that the FLIm-OCT multimodal approach has great potential to

replace costly destructive tests in the manufacturing of tissue engineered medical products, facilitating their clinical translation.

A new multispectral fluorescence lifetime imaging system with significantly improved performance was developed based on the state-of-art solid state avalanche photodiodes in Chapter 5. The new system addresses the limitations of the time-multiplexing single-PMT instrumentation. Individual gain adjustment for each spectral channel, five-times lower measurements standard deviation, four-times faster imaging speed and smaller footprint were achieved, which will facilitate the translation of FLIm and related technologies from benchtop to bedside.

In entirety, this dissertation provides strong evidence for the potential of fluorescence lifetime imaging and optical coherence tomography for early detection of OA and nondestructive monitoring of engineered cartilage maturation. A novel multispectral FLIm system with faster imaging speed, low measurement variability and individual gain control for each channel is developed. Results from this work serve as a crucial step for the adoption of multimodal FLIm-OCT to address the challenges of improving the patient care of osteoarthritis.

References

1. T. Vos, A. D. Flaxman, M. Naghavi, R. Lozano, C. Michaud, and M. Ezzati, "Years lived with disability (YLDs) for 1160 sequelae of 289 diseases and injuries 1990-2010: a systematic analysis for the Global Burden of Disease Study 2010," Lancet **380**, 2163-2196 (2012).
2. F. Xie, B. Kovic, X. Jin, X. He, M. Wang, and C. Silvestre, "Economic and Humanistic Burden of Osteoarthritis: A Systematic Review of Large Sample Studies," Pharmacoeconomics **34**, 1087-1100 (2016).
3. K. E. Barbour, C. G. Helmick, M. Boring, and T. J. Brady, "Vital Signs: Prevalence of Doctor-Diagnosed Arthritis and Arthritis-Attributable Activity Limitation - United States, 2013-2015," MMWR Morb Mortal Wkly Rep **66**, 246-253 (2017).
4. L. B. Murphy, M. G. Cisternas, D. J. Pasta, C. G. Helmick, and E. H. Yelin, "Medical Expenditures and Earnings Losses Among US Adults With Arthritis in 2013," Arthrit Care Res **70**, 869-876 (2018).
5. K. A. Athanasiou, A. R. Shah, R. J. Hernandez, and R. G. LeBaron, "Basic science of articular cartilage repair," Clin Sports Med **20**, 223-247 (2001).
6. T. P. Andriacchi, S. Koo, and S. F. Scanlan, "Gait mechanics influence healthy cartilage morphology and osteoarthritis of the knee," J Bone Joint Surg Am **91 Suppl 1**, 95-101 (2009).
7. K. A. Athanasiou, E. M. Darling, J. C. Hu, G. D. DuRaine, and A. H. Reddi, *Articular cartilage* (CRC Press, 2013).
8. C. R. Chu, A. A. Williams, C. H. Coyle, and M. E. Bowers, "Early diagnosis to enable early treatment of pre-osteoarthritis," Arthritis Res Ther **14**, 212 (2012).
9. B. Johnstone, M. Alini, M. Cucchiarini, G. R. Dodge, D. Eglin, F. Guilak, H. Madry, A. Mata, R. L. Mauck, C. E. Semino, and M. J. Stoddart, "Tissue engineering for articular cartilage repair--the state of the art," Eur Cell Mater **25**, 248-267 (2013).
10. G. D. O'Connell, E. G. Lima, L. Bian, N. O. Chahine, M. B. Albro, J. L. Cook, G. A. Ateshian, and C. T. Hung, "Toward engineering a biological joint replacement," J Knee Surg **25**, 187-196 (2012).
11. L. Kock, C. C. van Donkelaar, and K. Ito, "Tissue engineering of functional articular cartilage: the current status," Cell Tissue Res **347**, 613-627 (2012).
12. J. C. Hu and K. A. Athanasiou, "A self-assembling process in articular cartilage tissue engineering," Tissue Eng **12**, 969-979 (2006).
13. M. B. Albro, M. S. Bergholt, J. P. St-Pierre, A. Vinals Guitart, H. M. Zlotnick, E. G. Evita, and M. M. Stevens, "Raman spectroscopic imaging for quantification of depth-dependent and local heterogeneities in native and engineered cartilage," NPJ Regen Med **3**, 3 (2018).
14. E. A. Makris, A. H. Gomoll, K. N. Malizos, J. C. Hu, and K. A. Athanasiou, "Repair and tissue engineering techniques for articular cartilage," Nat Rev Rheumatol **11**, 21-34 (2015).
15. S. Saarakkala, P. Waris, V. Waris, I. Tarkiainen, E. Karvanen, J. Aarnio, and J. M. Koski, "Diagnostic performance of knee ultrasonography for detecting degenerative changes of articular cartilage," Osteoarthritis Cartilage **20**, 376-381 (2012).
16. A. D. Rogers, J. E. Payne, and J. S. Yu, "Cartilage imaging: a review of current concepts and emerging technologies," Semin Roentgenol **48**, 148-157 (2013).
17. H. J. Braun and G. E. Gold, "Diagnosis of osteoarthritis: imaging," Bone **51**, 278-288 (2012).

18. W. P. Chan, P. Lang, M. P. Stevens, K. Sack, S. Majumdar, D. W. Stoller, C. Basch, and H. K. Genant, "Osteoarthritis of the knee: comparison of radiography, CT, and MR imaging to assess extent and severity," AJR Am J Roentgenol **157**, 799-806 (1991).
19. J. P. Wu, T. B. Kirk, and M. H. Zheng, "Study of the collagen structure in the superficial zone and physiological state of articular cartilage using a 3D confocal imaging technique," Journal of orthopaedic surgery and research **3**, 29 (2008).
20. K. G. Brockbank, W. R. MacLellan, J. Xie, S. F. Hamm-Alvarez, Z. Z. Chen, and K. Schenke-Layland, "Quantitative second harmonic generation imaging of cartilage damage," Cell Tissue Bank **9**, 299-307 (2008).
21. A. T. Yeh, M. J. Hammer-Wilson, D. C. Van Sickle, H. P. Benton, A. Zoumi, B. J. Tromberg, and G. M. Peavy, "Nonlinear optical microscopy of articular cartilage," Osteoarthr Cartilage **13**, 345-352 (2005).
22. J. Mansfield, J. Yu, D. Attenburrow, J. Moger, U. Tirlapur, J. Urban, Z. F. Cui, and P. Winlove, "The elastin network: its relationship with collagen and cells in articular cartilage as visualized by multiphoton microscopy," Journal of Anatomy **215**, 682-691 (2009).
23. A. Boskey and N. P. Camacho, "FT-IR imaging of native and tissue-engineered bone and cartilage," Biomaterials **28**, 2465-2478 (2007).
24. N. P. Camacho, P. West, P. A. Torzilli, and R. Mendelsohn, "FTIR microscopic imaging of collagen and proteoglycan in bovine cartilage," Biopolymers **62**, 1-8 (2001).
25. M. Kim, X. H. Bi, W. E. Horton, R. G. Spencer, and N. P. Camacho, "Fourier transform infrared imaging spectroscopic analysis of tissue engineered cartilage: histologic and biochemical correlations," Journal of Biomedical Optics **10**(2005).
26. N. T. Khanarian, M. K. Boushell, J. P. Spalazzi, N. Pleshko, A. L. Boskey, and H. H. Lu, "FTIR-I Compositional Mapping of the Cartilage-to-Bone Interface as a Function of Tissue Region and Age," J Bone Miner Res **29**, 2643-2652 (2014).
27. K. A. Esmonde-White, F. W. Esmonde-White, M. D. Morris, and B. J. Roessler, "Fiber-optic Raman spectroscopy of joint tissues," Analyst **136**, 1675-1685 (2011).
28. D. Gorpas, D. Ma, J. Bec, D. R. Yankelevich, and L. Marcu, "Real-Time Visualization of Tissue Surface Biochemical Features Derived From Fluorescence Lifetime Measurements," IEEE Trans Med Imaging **35**, 1802-1811 (2016).
29. M. Y. Berezin and S. Achilefu, "Fluorescence lifetime measurements and biological imaging," Chem Rev **110**, 2641-2684 (2010).
30. I. Georgakoudi, B. C. Jacobson, M. G. Muller, E. E. Sheets, K. Badizadegan, D. L. Carr-Locke, C. P. Crum, C. W. Boone, R. R. Dasari, J. Van Dam, and M. S. Feld, "NAD(P)H and collagen as in vivo quantitative fluorescent biomarkers of epithelial precancerous changes," Cancer Res **62**, 682-687 (2002).
31. C. R. Chu, A. Williams, D. Tolliver, C. K. Kwoh, S. Bruno, 3rd, and J. J. Irrgang, "Clinical optical coherence tomography of early articular cartilage degeneration in patients with degenerative meniscal tears," Arthritis Rheum **62**, 1412-1420 (2010).
32. M. J. O'Malley and C. R. Chu, "Arthroscopic optical coherence tomography in diagnosis of early arthritis," Minim Invasive Surg **2011**, 671308 (2011).
33. Y. Yang, A. Dubois, X. P. Qin, J. Li, A. El Haj, and R. K. Wang, "Investigation of optical coherence tomography as an imaging modality in tissue engineering," Physics in Medicine and Biology **51**, 1649-1659 (2006).

34. J. D. Pitts and M.-A. Mycek, "Design and development of a rapid acquisition laser-based fluorometer with simultaneous spectral and temporal resolution," Rev Sci Instrum **72**, 3061-3072 (2001).
35. Q. Y. Fang, T. Papaioannou, J. A. Jo, R. Vaitha, K. Shastry, and L. Marcu, "Time-domain laser-induced fluorescence spectroscopy apparatus for clinical diagnostics," Rev Sci Instrum **75**, 151-162 (2004).
36. J. R. Lakowicz, *Principles of fluorescence spectroscopy* (Springer Science & Business Media, 2013).
37. "Jablonski diagram" (2020/8/15/), https://chem.libretexts.org/@go/page/1769.
38. T. G. Scott, R. D. Spencer, N. J. Leonard, and G. Weber, "Emission Properties of Nadh . Studies of Fluorescence Lifetimes and Quantum Efficiencies of Nadh, Acpyadh, and Simplified Synthetic Models," Journal of the American Chemical Society **92**, 687-& (1970).
39. N. Ramanujam, "Fluorescence spectroscopy of neoplastic and non-neoplastic tissues," Neoplasia **2**, 89-117 (2000).
40. Q. R. Yu and A. A. Heikal, "Two-photon autofluorescence dynamics imaging reveals sensitivity of intracellular NADH concentration and conformation to cell physiology at the single-cell level," J Photoch Photobio B **95**, 46-57 (2009).
41. J. T. Sharick, P. F. Favreau, A. A. Gillette, S. M. Sdao, M. J. Merrins, and M. C. Skala, "Protein-bound NAD(P) H Lifetime is Sensitive to Multiple Fates of Glucose Carbon," Sci Rep-Uk **8**(2018).
42. N. Nakashima, K. Yoshihara, F. Tanaka, and K. Yagi, "Picosecond fluorescence lifetime of the coenzyme of D-amino acid oxidase," J Biol Chem **255**, 5261-5263 (1980).
43. B. Koziol, M. Markowicz, J. Kruk, and B. Plytycz, "Riboflavin as a source of autofluorescence in Eisenia fetida coelomocytes," Photochemistry and Photobiology **82**, 570-573 (2006).
44. Y. Sun, D. Responte, H. Xie, J. Liu, H. Fatakdawala, J. Hu, K. A. Athanasiou, and L. Marcu, "Nondestructive evaluation of tissue engineered articular cartilage using time-resolved fluorescence spectroscopy and ultrasound backscatter microscopy," Tissue Eng Part C Methods **18**, 215-226 (2012).
45. G. A. Wagnieres, W. M. Star, and B. C. Wilson, "In vivo fluorescence spectroscopy and imaging for oncological applications," Photochem Photobiol **68**, 603-632 (1998).
46. P. Galera, D. Vivien, S. Pronost, J. Bonaventure, F. Redini, G. Loyau, and J. P. Pujol, "Transforming Growth Factor-Beta-1 (Tgf-Beta-1) up-Regulation of Collagen Type-Ii in Primary Cultures of Rabbit Articular Chondrocytes (Rac) Involves Increased Messenger-Rna Levels without Affecting Messenger-Rna Stability and Procollagen Processing," J Cell Physiol **153**, 596-606 (1992).
47. K. Deshmukh and M. E. Nimni, "Isolation and Characterization of Cyanogen Bromide Peptides from Collagen of Bovine Articular Cartillage," Biochem J **133**, 615-622 (1973).
48. D. R. Eyre and J. J. Wu, "Collagen structure and cartilage matrix integrity," J Rheumatol Suppl **43**, 82-85 (1995).
49. G. Veit, B. Kobbe, D. R. Keene, M. Paulsson, M. Koch, and R. Wagener, "Collagen XXVIII, a novel von Willebrand factor A domain-containing protein with many imperfections in the collagenous domain," J Biol Chem **281**, 3494-3504 (2006).
50. K. Konig, H. Schneckenburger, J. Hemmer, B. Tromberg, and R. Steiner, "In-Vivo Fluorescence Detection and Imaging of Porphyrin-Producing Bacteria in the Human Skin

and in the Oral Cavity for Diagnosis of Acne-Vulgaris, Caries, and Squamous-Cell Carcinoma," Advances in Laser and Light Spectroscopy to Diagnose Cancer and Other Diseases **2135**, 129-138 (1994).
51. N. D. Kirkpatrick, J. B. Hoying, S. K. Botting, J. A. Weiss, and U. Utzinger, "In vitro model for endogenous optical signatures of collagen," Journal of Biomedical Optics **11**(2006).
52. R. R. Kortum, R. Drezek, K. Sokolov, I. Pavlova, and M. Follen, "Survey of endogenous biological fluorophores," in *Handbook of biomedical fluorescence* (CRC Press, 2003), pp. 237-264.
53. S. Cortassa, M. A. Aon, E. Marban, R. L. Winslow, and B. O'Rourke, "An integrated model of cardiac mitochondrial energy metabolism and calcium dynamics," Biophys J **84**, 2734-2755 (2003).
54. W. C. Stanley, G. D. Lopaschuk, J. L. Hall, and J. G. McCormack, "Regulation of myocardial carbohydrate metabolism under normal and ischaemic conditions - Potential for pharmacological interventions," Cardiovasc Res **33**, 243-257 (1997).
55. R. D. Spencer and G. Weber, "Measurements of Subnanosecond Fluorescence Lifetimes with a Cross-Correlation Phase Fluorometer," Ann Ny Acad Sci **158**, 361-& (1969).
56. S. D. M. Islam, T. Susdorf, A. Penzkofer, and P. Hegemann, "Fluorescence quenching of flavin adenine dinucleotide in aqueous solution by pH dependent isomerisation and photo-induced electron transfer," Chem Phys **295**, 137-149 (2003).
57. S. C. A. Yeh, M. S. Patterson, J. E. Hayward, and Q. Y. Fang, "Time-Resolved Fluorescence in Photodynamic Therapy," Photonics-Basel **1**, 530-564 (2014).
58. E. Gratton, S. Breusegem, J. Sutin, and Q. Q. Ruan, "Fluorescence lifetime imaging for the two-photon microscope: time-domain and frequency-domain methods," Journal of Biomedical Optics **8**, 381-390 (2003).
59. R. M. Clegg, O. Holub, and C. Gohlke, "Fluorescence lifetime-resolved imaging: Measuring lifetimes in an image," Biophotonics, Pt A **360**, 509-542 (2003).
60. L. Marcu, "Fluorescence lifetime techniques in medical applications," Ann Biomed Eng **40**, 304-331 (2012).
61. D. R. Yankelevich, D. Ma, J. Liu, Y. Sun, Y. Sun, J. Bec, D. S. Elson, and L. Marcu, "Design and evaluation of a device for fast multispectral time-resolved fluorescence spectroscopy and imaging," Rev Sci Instrum **85**, 034303 (2014).
62. X. B. Liu, D. Y. Lin, W. Becker, J. J. Niu, B. Yu, L. W. Liu, and J. L. Qu, "Fast fluorescence lifetime imaging techniques: A review on challenge and development," J Innov Opt Heal Sci **12**(2019).
63. H. C. Gerritsen, A. V. Agronskaia, A. N. Bader, and A. Esposito, "Time domain FLIM: Theory, instrumentation, and data analysis," Lab Tech Biochem Mol **33**, 95-132 (2009).
64. P. A. De Beule, C. Dunsby, N. P. Galletly, G. W. Stamp, A. C. Chu, U. Anand, P. Anand, C. D. Benham, A. Naylor, and P. M. French, "A hyperspectral fluorescence lifetime probe for skin cancer diagnosis," Rev Sci Instrum **78**, 123101 (2007).
65. W. Becker, A. Bergmann, and C. Biskup, "Multispectral fluorescence lifetime imaging by TCSPC," Microsc Res Tech **70**, 403-409 (2007).
66. J. L. Lagarto, F. Villa, S. Tisa, F. Zappa, V. Shcheslavskiy, F. S. Pavone, and R. Cicchi, "Real-time multispectral fluorescence lifetime imaging using Single Photon Avalanche Diode arrays," Sci Rep **10**, 8116 (2020).

67. J. L. Lagarto, V. Shcheslavskiy, F. S. Pavone, and R. Cicchi, "Real-time fiber-based fluorescence lifetime imaging with synchronous external illumination: A new path for clinical translation," J Biophotonics **13**, e201960119 (2020).
68. M. L. Bhaumik, G. L. Clark, J. Snell, and L. Ferder, "Stroboscopic Time-Resolved Spectroscopy," Rev Sci Instrum **36**, 37-& (1965).
69. B. G. Barisas and M. D. Leuther, "Grid-Gated Photomultiplier Photometer with Sub-Nanosecond Time Response," Rev Sci Instrum **51**, 74-78 (1980).
70. R. G. Bennett, "Instrument to Measure Fluorescence Lifetimes in the Millimicrosecond Region," Rev Sci Instrum **31**, 1275-1279 (1960).
71. Y. Sun, R. Liu, D. S. Elson, C. W. Hollars, J. A. Jo, J. Park, Y. Sun, and L. Marcu, "Simultaneous time- and wavelength-resolved fluorescence spectroscopy for near real-time tissue diagnosis," Opt Lett **33**, 630-632 (2008).
72. W. Becker, *Advanced time-correlated single photon counting techniques* (Springer Science & Business Media, 2005), Vol. 81.
73. A. Ruck, C. Hulshoff, I. Kinzler, W. Becker, and R. Steiner, "SLIM: a new method for molecular imaging," Microsc Res Tech **70**, 485-492 (2007).
74. R. Erdmann, J. Enderlein, and M. Wahl, *Time correlated single-photon counting and fluorescence spectroscopy* (2005).
75. M. Monici, "Cell and tissue autofluorescence research and diagnostic applications," Biotechnol Annu Rev **11**, 227-256 (2005).
76. S. Coda, A. J. Thompson, G. T. Kennedy, K. L. Roche, L. Ayaru, D. S. Bansi, G. W. Stamp, A. V. Thillainayagam, P. M. French, and C. Dunsby, "Fluorescence lifetime spectroscopy of tissue autofluorescence in normal and diseased colon measured ex vivo using a fiber-optic probe," Biomed Opt Express **5**, 515-538 (2014).
77. B. H. Malik, J. Lee, S. Cheng, R. Cuenca, J. M. Jabbour, Y. S. Cheng, J. M. Wright, B. Ahmed, K. C. Maitland, and J. A. Jo, "Objective Detection of Oral Carcinoma with Multispectral Fluorescence Lifetime Imaging In Vivo," Photochem Photobiol **92**, 694-701 (2016).
78. L. Marcu, W. S. Grundfest, and J. M. Maarek, "Photobleaching of arterial fluorescent compounds: characterization of elastin, collagen and cholesterol time-resolved spectra during prolonged ultraviolet irradiation," Photochem Photobiol **69**, 713-721 (1999).
79. D. Ma, J. Bec, D. Gorpas, D. Yankelevich, and L. Marcu, "Technique for real-time tissue characterization based on scanning multispectral fluorescence lifetime spectroscopy (ms-TRFS)," Biomed Opt Express **6**, 987-1002 (2015).
80. D. Gorpas, J. Phipps, J. Bec, D. Ma, S. Dochow, D. Yankelevich, J. Sorger, J. Popp, A. Bewley, R. Gandour-Edwards, L. Marcu, and D. G. Farwell, "Autofluorescence lifetime augmented reality as a means for real-time robotic surgery guidance in human patients," Sci Rep **9**, 1187 (2019).
81. B. W. Weyers, M. Marsden, T. Sun, J. Bec, A. F. Bewley, R. F. Gandour-Edwards, M. G. Moore, D. G. Farwell, and L. Marcu, "Fluorescence lifetime imaging for intraoperative cancer delineation in transoral robotic surgery," Transl Biophotonics **1**, e201900017 (2019).
82. A. Alfonso-Garcia, J. Bec, S. Sridharan Weaver, B. Hartl, J. Unger, M. Bobinski, M. Lechpammer, F. Girgis, J. Boggan, and L. Marcu, "Real-time augmented reality for delineation of surgical margins during neurosurgery using autofluorescence lifetime contrast," J Biophotonics **13**, e201900108 (2020).

83. J. Bec, J. E. Phipps, D. Gorpas, D. Ma, H. Fatakdawala, K. B. Margulies, J. A. Southard, and L. Marcu, "In vivo label-free structural and biochemical imaging of coronary arteries using an integrated ultrasound and multispectral fluorescence lifetime catheter system," Sci Rep **7**, 8960 (2017).
84. J. E. Phipps, D. Gorpas, J. Unger, M. Darrow, R. J. Bold, and L. Marcu, "Automated detection of breast cancer in resected specimens with fluorescence lifetime imaging," Phys Med Biol **63**, 015003 (2017).
85. A. Alfonso-Garcia, J. Shklover, B. E. Sherlock, A. Panitch, L. G. Griffiths, and L. Marcu, "Fiber-based fluorescence lifetime imaging of recellularization processes on vascular tissue constructs," J Biophotonics **11**, e201700391 (2018).
86. A. K. Haudenschild, B. E. Sherlock, X. Zhou, J. C. Hu, J. K. Leach, L. Marcu, and K. A. Athanasiou, "Non-destructive detection of matrix stabilization correlates with enhanced mechanical properties of self-assembled articular cartilage," J Tissue Eng Regen Med **13**, 637-648 (2019).
87. S. Shrestha, B. E. Applegate, J. Park, X. Xiao, P. Pande, and J. A. Jo, "High-speed multispectral fluorescence lifetime imaging implementation for in vivo applications," Opt Lett **35**, 2558-2560 (2010).
88. D. S. Kittle, F. Vasefi, C. G. Patil, A. Mamelak, K. L. Black, and P. V. Butte, "Real time optical Biopsy: Time-resolved Fluorescence Spectroscopy instrumentation and validation," Sci Rep **6**, 38190 (2016).
89. H. S. Nam, W. J. Kang, M. W. Lee, J. W. Song, J. W. Kim, W. Y. Oh, and H. Yoo, "Multispectral analog-mean-delay fluorescence lifetime imaging combined with optical coherence tomography," Biomed Opt Express **9**, 1930-1947 (2018).
90. S. Cheng, R. M. Cuenca, B. Liu, B. H. Malik, J. M. Jabbour, K. C. Maitland, J. Wright, Y. S. Cheng, and J. A. Jo, "Handheld multispectral fluorescence lifetime imaging system for in vivo applications," Biomed Opt Express **5**, 921-931 (2014).
91. R. A. Romano, R. G. Teixeira Rosa, A. G. Salvio, J. A. Jo, and C. Kurachi, "Multispectral autofluorescence dermoscope for skin lesion assessment," Photodiagnosis Photodyn Ther **30**, 101704 (2020).
92. L. Marcu, P. M. French, and D. S. Elson, *Fluorescence lifetime spectroscopy and imaging: principles and applications in biomedical diagnostics* (CRC Press, 2014).
93. K. C. Lee, J. Siegel, S. E. Webb, S. Leveque-Fort, M. J. Cole, R. Jones, K. Dowling, M. J. Lever, and P. M. French, "Application of the stretched exponential function to fluorescence lifetime imaging," Biophys J **81**, 1265-1274 (2001).
94. J. C. Andre, L. M. Vincent, D. Oconnor, and W. R. Ware, "Applications of Fast Fourier-Transform to Deconvolution in Single Photon-Counting," J Phys Chem-Us **83**, 2285-2294 (1979).
95. A. Gafni, R. L. Modlin, and L. Brand, "Analysis of Fluorescence Decay Curves by Means of Laplace Transformation," Biophys J **15**, 263-280 (1975).
96. W. R. Ware, L. J. Doemeny, and T. L. Nemzek, "Deconvolution of Fluorescence and Phosphorescence Decay Curves - Least-Squares Method," J Phys Chem-Us **77**, 2038-2048 (1973).
97. J. M. Maarek, L. Marcu, W. J. Snyder, and W. S. Grundfest, "Time-resolved fluorescence spectra of arterial fluorescent compounds: reconstruction with the Laguerre expansion technique," Photochem Photobiol **71**, 178-187 (2000).

98. I. Isenberg, J. P. Mullooly, R. D. Dyson, and R. Hanson, "Studies on Analysis of Fluorescence Decay Data by Method of Moments," Biophys J **13**, 1090-1115 (1973).
99. J. Liu, Y. Sun, J. Qi, and L. Marcu, "A novel method for fast and robust estimation of fluorescence decay dynamics using constrained least-squares deconvolution with Laguerre expansion," Phys Med Biol **57**, 843-865 (2012).
100. Z. G. Wang, D. B. Durand, M. Schoenberg, and Y. T. Pan, "Fluorescence guided optical coherence tomography for the diagnosis of early bladder cancer in a rat model," J Urology **174**, 2376-2381 (2005).
101. T. A. Shaik, A. Alfonso-Garcia, X. Zhou, K. M. Arnold, A. K. Haudenschild, C. Krafft, L. G. Griffiths, J. Popp, and L. Marcu, "FLIm-Guided Raman Imaging to Study Cross-Linking and Calcification of Bovine Pericardium," Anal Chem **92**, 10659-10667 (2020).
102. S. Dochow, H. Fatakdawala, J. E. Phipps, D. Ma, T. Bocklitz, M. Schmitt, J. W. Bishop, K. B. Margulies, L. Marcu, and J. Popp, "Comparing Raman and fluorescence lifetime spectroscopy from human atherosclerotic lesions using a bimodal probe," J Biophotonics **9**, 958-966 (2016).
103. D. Gorpas, H. Fatakdawala, J. Bec, D. Ma, D. R. Yankelevich, J. Qi, and L. Marcu, "Fluorescence lifetime imaging and intravascular ultrasound: co-registration study using ex vivo human coronaries," IEEE Trans Med Imaging **34**, 156-166 (2015).
104. H. Fatakdawala, D. Gorpas, J. W. Bishop, J. Bec, D. Ma, J. A. Southard, K. B. Margulies, and L. Marcu, "Fluorescence Lifetime Imaging Combined with Conventional Intravascular Ultrasound for Enhanced Assessment of Atherosclerotic Plaques: an Ex Vivo Study in Human Coronary Arteries," J Cardiovasc Transl Res **8**, 253-263 (2015).
105. Y. Sun, H. Xie, J. Liu, M. Lam, A. J. Chaudhari, F. Zhou, J. Bec, D. R. Yankelevich, A. Dobbie, S. L. Tinling, R. F. Gandour-Edwards, W. L. Monsky, D. G. Farwell, and L. Marcu, "In vivo validation of a bimodal technique combining time-resolved fluorescence spectroscopy and ultrasonic backscatter microscopy for diagnosis of oral carcinoma," J Biomed Opt **17**, 116003 (2012).
106. B. Z. Fite, M. Decaris, Y. Sun, Y. Sun, A. Lam, C. K. Ho, J. K. Leach, and L. Marcu, "Noninvasive multimodal evaluation of bioengineered cartilage constructs combining time-resolved fluorescence and ultrasound imaging," Tissue Eng Part C Methods **17**, 495-504 (2011).
107. S. S. Liang, A. Saidi, J. Jing, G. J. Liu, J. W. Li, J. Zhang, C. S. Sun, J. Narula, and Z. P. Chen, "Intravascular atherosclerotic imaging with combined fluorescence and optical coherence tomography probe based on a double-clad fiber combiner," Journal of Biomedical Optics **17**(2012).
108. J. K. Barton, F. Guzman, and A. Tumlinson, "Dual modality instrument for simultaneous optical coherence tomography imaging and fluorescence spectroscopy," Journal of Biomedical Optics **9**, 618-623 (2004).
109. L. P. Hariri, A. R. Tumlinson, D. G. Besselsen, U. Utzinger, E. W. Gerner, and J. K. Barton, "Endoscopic optical coherence tomography and laser-induced fluorescence spectroscopy in a murine colon cancer model," Laser Surg Med **38**, 305-313 (2006).
110. C. A. Patil, N. Bosschaart, M. D. Keller, T. G. van Leeuwen, and A. Mahadevan-Jansen, "Combined Raman spectroscopy and optical coherence tomography device for tissue characterization," Opt Lett **33**, 1135-1137 (2008).

111. M. Mazurenka, L. Behrendt, M. Meinhardt-Wollweber, U. Morgner, and B. Roth, "Development of a combined OCT-Raman probe for the prospective in vivo clinical melanoma skin cancer screening," Rev Sci Instrum **88**(2017).
112. D. Vasquez, F. Knorr, F. Hoffmann, G. Ernst, L. Marcu, M. Schmitt, O. Guntinas-Lichius, J. Popp, and I. W. Schie, "Multimodal Scanning Microscope Combining Optical Coherence Tomography, Raman Spectroscopy and Fluorescence Lifetime Microscopy for Mesoscale Label-Free Imaging of Tissue," Anal Chem **93**, 11479-11487 (2021).
113. B. E. Sherlock, J. E. Phipps, J. Bec, and L. Marcu, "Simultaneous, label-free, multispectral fluorescence lifetime imaging and optical coherence tomography using a double-clad fiber," Opt Lett **42**, 3753-3756 (2017).
114. M. R. Hee, J. A. Izatt, E. A. Swanson, D. Huang, J. S. Schuman, C. P. Lin, C. A. Puliafito, and J. G. Fujimoto, "Optical Coherence Tomography of the Human Retina," Arch Ophthalmol-Chic **113**, 325-332 (1995).
115. B. E. Sherlock, X. Zhou, J. Bec, and L. Marcu, "Synchronous fluorescence lifetime imaging and optical coherence tomography using a double clad fiber," Ieee Photon Conf (2016).
116. X. Zhou, A. K. Haudenschild, B. E. Sherlock, J. C. Hu, J. K. Leach, K. A. Athanasiou, and L. Marcu, "Detection of glycosaminoglycan loss in articular cartilage by fluorescence lifetime imaging," J Biomed Opt **23**, 1-8 (2018).
117. T. Vos, A. D. Flaxman, M. Naghavi, R. Lozano, and C. Michaud, "Years lived with disability (YLDs) for 1160 sequelae of 289 diseases and injuries 1990-2010: a systematic analysis for the Global Burden of Disease Study 2010," Lancet **380**, 2163-2196 (2012).
118. F. Guilak, L. Setton, and V. Kraus, "Structure and function of articular cartilage," Principles And Practice Of Orthopaedic Sports Medicine. In Principles and Practice of Orthopaedic Sports Medicine. Edited by Garrett WE, et al. Philadelphia, PA: Lippincott Williams & Wilkins (2000).
119. L. A. Setton, V. C. Mow, F. J. Muller, J. C. Pita, and D. S. Howell, "Altered structure-function relationships for articular cartilage in human osteoarthritis and an experimental canine model," Agents Actions Suppl **39**, 27-48 (1993).
120. B. Z. Fite, M. Decaris, Y. H. Sun, Y. Sun, A. Lam, C. K. L. Ho, J. K. Leach, and L. Marcu, "Noninvasive Multimodal Evaluation of Bioengineered Cartilage Constructs Combining Time-Resolved Fluorescence and Ultrasound Imaging," Tissue Eng Part C-Me **17**, 495-504 (2011).
121. Y. Sun, D. Responte, H. T. Xie, J. Liu, H. Fatakdawala, J. Hu, K. A. Athanasiou, and L. Marcu, "Nondestructive Evaluation of Tissue Engineered Articular Cartilage Using Time-Resolved Fluorescence Spectroscopy and Ultrasound Backscatter Microscopy," Tissue Eng Part C-Me **18**, 215-226 (2012).
122. D. L. Ma, J. Bec, D. Gorpas, D. Yankelevich, and L. Marcu, "Technique for real-time tissue characterization based on scanning multispectral fluorescence lifetime spectroscopy (ms-TRFS)," Biomedical Optics Express **6**, 987-1002 (2015).
123. D. H. Agemura, W. D. O'Brien, Jr., J. E. Olerud, L. E. Chun, and D. E. Eyre, "Ultrasonic propagation properties of articular cartilage at 100 MHz," J Acoust Soc Am **87**, 1786-1791 (1990).
124. G. O. Angheloiu, A. S. Haka, I. Georgakoudi, J. Arendt, M. G. Muller, O. R. Scepanovic, S. P. Evanko, T. N. Wight, P. Mukherjee, D. H. Waldeck, R. R. Dasari, M. Fitzmaurice, J. R. Kramer, and M. S. Feld, "Detection of coronary atherosclerotic plaques with superficial

proteoglycans and foam cells using real-time intrinsic fluorescence spectroscopy," Atherosclerosis **215**, 96-102 (2011).
125. D. R. Yankelevich, D. L. Ma, J. Liu, Y. Sun, Y. Sun, J. Bec, D. S. Elson, and L. Marcu, "Design and evaluation of a device for fast multispectral time-resolved fluorescence spectroscopy and imaging," Review of Scientific Instruments **85**(2014).
126. Y. Sun, R. Liu, D. S. Elson, C. W. Hollars, J. A. Jo, J. Park, Y. Sun, and L. Marcu, "Simultaneous time- and wavelength-resolved fluorescence spectroscopy for near real-time tissue diagnosis," Optics Letters **33**, 630-632 (2008).
127. J. Liu, Y. Sun, J. Y. Qi, and L. Marcu, "A novel method for fast and robust estimation of fluorescence decay dynamics using constrained least-squares deconvolution with Laguerre expansion," Physics in Medicine and Biology **57**, 843-865 (2012).
128. D. S. Elson, N. Galletly, C. Talbot, J. Requejo-Isidro, J. McGinty, C. Dunsby, P. M. P. Lanigan, I. Munro, R. K. P. Benninger, P. de Beule, E. Auksorius, L. Hegyi, A. Sandison, A. Wallace, P. Soutter, M. A. A. Neil, J. Lever, G. W. Stamp, and P. M. W. French, "Multidimensional Fluorescence Imaging Applied to Biological Tissue," in *Reviews in Fluorescence 2006*, C. D. Geddes and J. R. Lakowicz, eds. (Springer US, Boston, MA, 2006), pp. 477-524.
129. A. K. Haudenschild, B. E. Sherlock, X. Zhou, J. C. Hu, J. K. Leach, L. Marcu, and K. A. Athanasiou, "Nondestructive fluorescence lifetime imaging and time-resolved fluorescence spectroscopy detect cartilage matrix depletion and correlate with mechanical properties," Eur Cell Mater **36**, 30-43 (2018).
130. M. J. Nissi, F. Toth, L. N. Wang, C. S. Carlson, and J. M. Ellermann, "Improved Visualization of Cartilage Canals Using Quantitative Susceptibility Mapping," Plos One **10**(2015).
131. J. E. Phipps, D. Gorpas, J. Unger, M. Darrow, R. J. Bold, and L. Marcu, "Automated detection of breast cancer in resected specimens with fluorescence lifetime imaging," Phys Med Biol (2017).
132. Y. Sun, J. E. Phipps, J. Meier, N. Hatami, B. Poirier, D. S. Elson, D. G. Farwell, and L. Marcu, "Endoscopic fluorescence lifetime imaging for in vivo intraoperative diagnosis of oral carcinoma," Microsc Microanal **19**, 791-798 (2013).
133. D. S. Elson, J. A. Jo, and L. Marcu, "Miniaturized side-viewing imaging probe for fluorescence lifetime imaging (FLIM): validation with fluorescence dyes, tissue structural proteins and tissue specimens," New J Phys **9**(2007).
134. B. E. Sherlock, J. E. Phipps, J. Bec, and L. Marcu, "Simultaneous, label-free, multispectral fluorescence lifetime imaging and optical coherence tomography using a double-clad fiber," Optics Letters **42**, 3753-3756 (2017).
135. E. B. Hunziker, "Articular cartilage repair: are the intrinsic biological constraints undermining this process insuperable?," Osteoarthr Cartilage **7**, 15-28 (1999).
136. J. R. Steadman, W. G. Rodkey, and J. J. Rodrigo, "Microfracture: Surgical technique and rehabilitation to treat chondral defects," Clin Orthop Relat R, S362-S369 (2001).
137. N. J. Castro, G. Babakhanova, J. Hu, and K. A. Athanasiou, "Nondestructive testing of native and tissue-engineered medical products: adding numbers to pictures," Trends Biotechnol (2021).
138. R. P. Harrison, N. Medcalf, and Q. A. Rafiq, "Cell therapy-processing economics: small-scale microfactories as a stepping stone toward large-scale macrofactories," Regen Med **13**, 160-174 (2018).

139. K. Moisio, F. Eckstein, J. S. Chmiel, A. Guermazi, P. Prasad, O. Almagor, J. Song, D. Dunlop, M. Hudelmaier, A. Kothari, and L. Sharma, "Denuded Subchondral Bone and Knee Pain in Persons With Knee Osteoarthritis," Arthritis Rheum-Us **60**, 3703-3710 (2009).
140. L. Bian, S. L. Angione, K. W. Ng, E. G. Lima, D. Y. Williams, D. Q. Mao, G. A. Ateshian, and C. T. Hung, "Influence of decreasing nutrient path length on the development of engineered cartilage," Osteoarthr Cartilage **17**, 677-685 (2009).
141. C. T. Hung, E. G. Lima, R. L. Mauck, E. Taki, M. A. LeRoux, H. H. Lu, R. G. Stark, X. E. Guo, and G. A. Ateshian, "Anatomically shaped osteochondral constructs for articular cartilage repair," Journal of Biomechanics **36**, 1853-1864 (2003).
142. C. I. Hung, R. L. Mauck, C. C. B. Wang, E. G. Lima, and G. A. Ateshian, "A paradigm for functional tissue engineering of articular cartilage via applied physiologic deformational loading (vol 32, pg 35, 2004)," Annals of Biomedical Engineering **32**, 510-510 (2004).
143. J. N. Harvestine, C. S. Sheaff, C. Li, A. K. Haudenschild, M. A. Gionet-Gonzales, J. C. Hu, K. A. Athanasiou, L. Marcu, and J. K. Leach, "Multimodal Label-Free Imaging for Detecting Maturation of Engineered Osteogenic Grafts," Acs Biomater Sci Eng **5**, 1956-1966 (2019).
144. D. Mitra, H. Fatakdawala, M. Nguyen-Truong, A. Creecy, J. Nyman, L. Marcu, and J. K. Leach, "Detection of Pentosidine Cross-Links in Cell-Secreted Decellularized Matrices Using Time Resolved Fluorescence Spectroscopy," Acs Biomater Sci Eng **3**, 1944-1954 (2017).
145. D. Huang, E. A. Swanson, C. P. Lin, J. S. Schuman, W. G. Stinson, W. Chang, M. R. Hee, T. Flotte, K. Gregory, C. A. Puliafito, and J. G. Fujimoto, "Optical Coherence Tomography," Science **254**, 1178-1181 (1991).
146. M. E. Brezinski and J. G. Fujimoto, "Optical coherence tomography: High-resolution imaging in nontransparent tissue," Ieee J Sel Top Quant **5**, 1185-1192 (1999).
147. H. Yabushita, B. E. Bourna, S. L. Houser, T. Aretz, I. K. Jang, K. H. Schlendorf, C. R. Kauffman, M. Shishkov, D. H. Kang, E. F. Halpern, and G. J. Tearney, "Characterization of human atherosclerosis by optical coherence tomography," Circulation **106**, 1640-1645 (2002).
148. R. Wessels, D. M. De Bruin, D. J. Faber, T. G. Van Leeuwen, M. Van Beurden, and T. J. M. Ruers, "Optical biopsy of epithelial cancers by optical coherence tomography (OCT)," Laser Med Sci **29**, 1297-1305 (2014).
149. H. Jahr, N. Brill, and S. Nebelung, "Detecting early stage osteoarthritis by optical coherence tomography?," Biomarkers **20**, 590-596 (2015).
150. M. T. El-Haddad and Y. K. Tao, "Advances in intraoperative optical coherence tomography for surgical guidance," Curr Opin Biomed Eng **3**, 37-48 (2017).
151. K. Kim and W. R. Wagner, "Non-invasive and Non-destructive Characterization of Tissue Engineered Constructs Using Ultrasound Imaging Technologies: A Review," Annals of Biomedical Engineering **44**, 621-635 (2016).
152. M. B. Albro, R. J. Nims, K. M. Durney, A. D. Cigan, J. J. Shim, G. Vunjak-Noyakovic, C. T. Hung, and G. A. Ateshian, "Heterogeneous engineered cartilage growth results from gradients of media-supplemented active TGF-beta and is ameliorated by the alternative supplementation of latent TGF-beta," Biomaterials **77**, 173-185 (2016).
153. Z. P. Luo, "Statistical quantification of the microstructural homogeneity of size and orientation distributions," J Mater Sci **45**, 3228-3241 (2010).

154. B. A. Byers, R. L. Mauck, I. E. Chiang, and R. S. Tuan, "Transient exposure to transforming growth factor beta 3 under serum-free conditions enhances the biomechanical and biochemical maturation of tissue-engineered cartilage," Tissue Eng Part A **14**, 1821-1834 (2008).
155. A. H. Huang, A. Stein, R. S. Tuan, and R. L. Mauck, "Transient exposure to transforming growth factor beta 3 improves the mechanical properties of mesenchymal stem cell-laden cartilage constructs in a density-dependent manner," Tissue Eng Part A **15**, 3461-3472 (2009).
156. C. M. Revell, C. E. Reynolds, and K. A. Athanasiou, "Effects of initial cell seeding in self assembly of articular cartilage," Ann Biomed Eng **36**, 1441-1448 (2008).
157. Y. Hiraki, H. Inoue, R. Hirai, Y. Kato, and F. Suzuki, "Effect of transforming growth factor beta on cell proliferation and glycosaminoglycan synthesis by rabbit growth-plate chondrocytes in culture," Biochim Biophys Acta **969**, 91-99 (1988).
158. T. I. Morales and A. B. Roberts, "Transforming growth factor beta regulates the metabolism of proteoglycans in bovine cartilage organ cultures," J Biol Chem **263**, 12828-12831 (1988).
159. F. Redini, P. Galera, A. Mauviel, G. Loyau, and J. P. Pujol, "Transforming growth factor beta stimulates collagen and glycosaminoglycan biosynthesis in cultured rabbit articular chondrocytes," FEBS Lett **234**, 172-176 (1988).
160. X. Zhou, J. Bec, D. Yankelevich, and L. Marcu, "Multispectral fluorescence lifetime imaging device with a silicon avalanche photodetector," Opt Express **29**, 20105-20120 (2021).
161. A. C. Croce and G. Bottiroli, "Autofluorescence spectroscopy and imaging: a tool for biomedical research and diagnosis," Eur J Histochem **58**, 2461 (2014).
162. M.-A. Mycek, K. T. Schomacker, and N. S. Nishioka, "Colonic polyp differentiation using time-resolved autofluorescence spectroscopy," Gastrointest Endosc **48**, 390-394 (1998).
163. M. Marsden, T. Fukazawa, Y. C. Deng, B. W. Weyers, J. Bec, D. Gregory Farwell, and L. Marcu, "FLImBrush: dynamic visualization of intraoperative free-hand fiber-based fluorescence lifetime imaging," Biomed Opt Express **11**, 5166-5180 (2020).
164. J. Kim, M. Lee, J. H. Yang, and J. H. Choy, "Photophysical properties of hemicyanine dyes intercalated in Na-fluorine mica," J Phys Chem A **104**, 1388-1392 (2000).
165. L. Rabiner, R. Schafer, and D. Dlugos, *Programs for Digital Signal Processing, edited by Digital Signal Processing Committee of the IEEE Acoustics, Speech and Signal Processing Society* (IEEE, 1979).
166. T. J. Paulus, "Timing Electronics and Fast Timing Methods with Scintillation Detectors," Ieee T Nucl Sci **32**, 1242-1249 (1985).
167. D. A. Gedcke and W. J. McDonald, "A constant fraction of pulse height trigger for optimum time resolution," Nuclear Instruments and Methods **55**, 377-380 (1967).
168. International Electrotechnical Commission, "Safety of Laser Products - Part 1: Equipment Classification, and Requirements," IEC 60825–1 (2014).
169. H. Pal, S. Nad, and M. Kumbhakar, "Photophysical properties of coumarin-120: Unusual behavior in nonpolar solvents," The Journal of Chemical Physics **119**, 443-452 (2003).
170. D. Magde, G. E. Rojas, and P. G. Seybold, "Solvent Dependence of the Fluorescence Lifetimes of Xanthene Dyes," Photochemistry and Photobiology **70**, 737-744 (1999).

171. A. S. Dabir, C. A. Trivedi, Y. Ryu, P. Pande, and J. A. Jo, "Fully automated deconvolution method for on-line analysis of time-resolved fluorescence spectroscopy data based on an iterative Laguerre expansion technique," J Biomed Opt **14**, 024030 (2009).
172. A. Žukauskas, P. Vitta, N. Kurilčik, S. Juršėnas, and E. Bakienė, "Characterization of biological materials by frequency-domain fluorescence lifetime measurements using ultraviolet light-emitting diodes," Opt Mater **30**, 800-805 (2008).
173. B. Steindl, R. Enne, S. Schidl, and H. Zimmermann, "Linear Mode Avalanche Photodiode With High Responsivity Integrated in High-Voltage CMOS," Ieee Electr Device L **35**, 897-899 (2014).